# Structural and Dynamic Properties of Disordered Solids

Thesis presented for the degree of
Doctor of Philosophy

Matthew Jonathan Jones

University College London

1997

ProQuest Number: 10106940

# ProQuest.

ProQuest 10106940

# Acknowledgements

# Abstract

The structural and dynamic properties of several disordered solids were investigated using a range of experimental techniques. Ni K–edge EXAFS spectroscopy was used to study the local environment of the nickel atoms in several *catena*-[(1,2–diaminopropane)–cadmium(II)–tetra–$\mu$–cyanonickelate(II)] inclusion compounds containing halogenated alkane guest molecules. The main contribution to the spectra arises from the CN–units and the Cd atoms surrounding the Ni atoms. For all guest molecules studied (with one exception) a significant contribution from the halogen atoms of the guest is observed, suggesting some degree of ordering of the guest molecules with respect to the host substructure. Incoherent quasielastic neutron scattering (IQNS) was employed to study the dynamics of *tetrakis*(trimethylsilyl)silane (TTMSS). The dynamics at low temperature are consistent with 3–fold rotational jumps with a gyration radius of *ca.* 1 Å, ascribed to rotation of the methyl groups about the C–Si bond. At *ca.* 240 K a phase transition occurs, associated with a change of dynamics. At ambient temperature the motion is consistent with isotropic rotation on a sphere. The structure of the thiourea/chlorocyclohexane inclusion compound was investigated *via* X–ray powder diffraction. The structure of the high temperature phase is consistent with previous studies. The low temperature structure is a distorted form of the high temperature structure, and in contrast to the latter the guest molecules have well defined positions. The guest molecule dynamics in the thiourea/chlorocyclohexane and thiourea/cyclohexane inclusion compounds were studied using IQNS. For cyclohexane the motion is described by a combination of 3–fold rotational jumps about the molecular axis and 3–fold rotational jumps about the tunnel axis. The guest molecules are tilted with respect to the tunnel axis. The results for chlorocyclohexane are qualitatively similar to those for cyclohexane. For both compounds there is a change in the guest dynamics at the respective phase transition temperatures, the nature of which could not be determined.

3

# Contents

# List of Figures

# List of Tables

# Chapter 1

# Introduction

Disorder in crystalline solids has been of great interest ever since it has been possible to verify it experimentally and to treat its existence theoretically. From simple point defects in atomic crystals to orientational disorder in molecular crystals there are numerous manifestations of this phenomenon (for a detailed review see [1]). Often a classification in terms of both positional and orientational and static and dynamic disorder is encountered. Positional disorder can be encountered if, within a particular structure, there is an excess of sites capable of accommodating a given particle, or if, for example, different types of particles are randomly distributed on equivalent sites. Orientational disorder, in contrast, generally refers to a situation where well defined positional ordering of a particle occurs, but where this particle can assume several distinguishable orientations. Whereas positional and orientational disorder are easily defined, static and dynamic disorder require care in their definition: a given spectroscopic technique will have a characteristic timescale and for any dynamic process slower than this, the system will appear to be static. Therefore one must always be mindful of the fact that static generally means static within the timescale of the experimental probe. Diffraction experiments do not yield time resolved information, but rather a time–averaged distribution of the scattering matter, which may lead to any observed disorder being interpreted

as static. This is not necessarily correct, however, since well defined locations of scattering matter do not preclude the occurrence of exchange between these sites.

Structural and dynamic properties of crystalline solids are intimately related. The degree of motional freedom an individual molecule has will depend to a large extent on the nature (and symmetry) of the potential it experiences, which is necessarily governed by the surrounding molecules. The arrangement of neighbouring molecules will also play a role in simple steric considerations regarding the motion of molecules. In this respect, application of a range of experimental techniques is essential for understanding in detail the properties of a given material, as each individual experiment will only provide a fragment of information, a view limited by the technique itself. Understanding disorder, its origins and effects then becomes a complex task of piecing together the information gained from numerous sources.

Two classes of compounds are particularly interesting, plastic crystals and inclusion compounds, and in the work presented here representatives of both classes were studied. Plastic crystals display a high degree of orientational disorder of the constituent molecules while retaining crystallinity through well defined positional ordering of the individual molecules. The degree of orientational disorder found is also commonly observed for guest molecules in certain solid inclusion compounds, which are also prime examples of the interrelation of structural and dynamic properties, as discussed in Chapters 4 and 6. The remainder of this chapter serves as a general introduction to plastic crystals and inclusion compounds and their general characteristics.

## 1.1 Plastic Crystals

Plastic crystals derive their name from one of their most striking macroscopic properties, their high plasticity. Plastic crystals are crystalline molecular solids

and exist in at least two distinguishable solid phases. At low temperature, these compounds are unremarkable, with both positional and orientational ordering of the constituent molecules. Heating the crystals results in a solid–solid phase transition to the plastic crystal phase, which is accompanied by an unusually high entropy change. This phase is generally of high symmetry. On further heating these crystals melt, with a low entropy of fusion.

Timmermans [2] first reviewed work on organic compounds displaying these characteristics. In his review article, Timmermans pointed out that all materials known to possess a plastically crystalline phase are either of high molecular symmetry (generally tetrahedral) or very nearly spherical. It was assumed, that the low entropy of fusion and the high entropy at the solid–solid phase transition indicated a high degree of orientational freedom of the constituent molecules, facilitated by their high symmetry.

Since then a great deal of work has been undertaken on this class of solids (for a review see [1, 3]) using a variety of experimental techniques, and it was seen that dynamic processes play an important role in determining the physical properties of the plastically crystalline state. However, a direct correlation of structural and dynamic properties proves difficult in most cases due to the lack of structural knowledge available as diffraction experiments generally yield only limited information. Due to the high degree of disorder in the plastically crystalline state, only a few reflections are generally observed in diffraction experiments, and those of weak intensity are often masked by diffuse scattering. In principle, this diffuse scattering contains much information about the disorder.

## 1.2 Inclusion Compounds

The term inclusion compound covers a vast range of different types of system. Molecular inclusion compounds consist of a molecular host containing cavities

within which a guest atom or molecule can be enclosed. Of these the crown ethers are one of the best known examples. The majority of the work presented in this thesis is concerned with crystalline inclusion compounds, in particular those in which the host structure comprises one–dimensional tunnels.

A crystalline inclusion compound is formed by a minimum of two distinct chemical species, of which one forms a crystalline substructure (denoted the host) containing "empty" space large enough to enclose the other (denoted the guest). There are no chemical bonds between the host and the guest molecules. Possibly the oldest known inclusion compounds are the ice clathrates discovered by Davy [4] and many other examples are known [5, 6, 7], formed both by inorganic host substructures (e.g. zeolites, Hofmann–type inclusion compounds) and organic host substructures (e.g. urea and thiourea inclusion compounds, cyclodextrins). Host materials with very different chemical nature are capable of forming inclusion compounds with similar topology of the spaces containing the guest molecules and similar selectivity towards the types of guest included. Therefore it appears prudent to distinguish not between inorganic and organic host materials but rather between different topologies of the space containing the guest molecules, i.e to distinguish between those inclusion compounds containing tunnels, cavities and combinations of these. Indeed, as discussed in more detail in Chapter 3, there are examples of inclusion compounds formed by a given host material with differing topology of the cavity, depending very much upon the type of guest molecule included.

Inclusion compounds are of interest for many reasons, not least for their (potential) applications. Zeolitic materials, for example, are of major industrial importance, used as catalysts and molecular sieves, cyclodextrins can be used to enclose pharmaceuticals in order to control the way in which a body absorbs them [8, 9, 10]. Thiourea inclusion compounds have potential applications due to the non–linear optical properties found in the presence of certain guest molecules [11, 12].

However, only a detailed understanding of the fundamental physical properties of inclusion compounds will allow their function to be controlled and any insight into their physical properties can only be gained through knowledge of the relationship between the constituent host and guest molecules and how the properties of one component interact with and influence the other.

# Chapter 2

# Theoretical Background

## 2.1 Fundamental Theory of EXAFS

X–ray Absorption Fine Structure is the sinusoidal modulation of the X–ray absorption coefficient for a given atom, observable as the incident X–ray energy increases beyond an absorption edge. Although there is no precise boundary, the X–ray absorption fine structure is usually interpreted in terms of two distinct regions. The first region, within a few tens of electron volts of the absorption edge, is called the X–ray Absorption Near Edge Structure (XANES) and contains information about the electronic structure and the local environment of the absorbing species [13]. The modulations beyond a few tens of electron volts and up to a few hundred electron volts beyond the absorption edge are called Extended X–ray Absorption Fine Structure (EXAFS) and can be interpreted mainly in terms of the immediate environment of the absorbing atom. The modulations of the absorption coefficient are caused by backscattering of an outgoing photoelectron wave, originating at the X–ray absorbing (central) atom, by neighbouring atoms and the subsequent interference of the backscattered wave with the outgoing wave. The EXAFS interference function, describing the modulation of the absorption coefficient, can be written

as [13]:

$$\chi(E) = \frac{\mu(E) - \mu_0(E)}{\mu_e(E)} \tag{2.1}$$

where $\mu(E)$ is the observed absorption coefficient and $\mu_0(E)$ is the smoothly varying absorption coefficient of an isolated atom. The latter is generally unknown, but with suitable procedures for background subtraction (see Section 2.1.1) it is not essential that $\mu_0(E)$ is known. The interference function is normalized to the absorption, $\mu_e$, due to the absorption edge.

Although the fine structure beyond absorption edges was first noticed as early as 1920 [14, 15], it was not until the early 1970's that a comprehensive and generally accepted theory describing the structural information contained in the spectra was available [16, 17]. The magnitude of the photoelectron wave vector, $k$, is related to the X–ray frequency, $\nu$, via

$$k = \sqrt{\frac{2m}{\hbar^2}(h\nu - E_0)} \tag{2.2}$$

where $E_0$ is the threshold energy for the removal of the core electron. The modulations of the absorption coefficient are due to scattering of the photoelectron by neighbouring atoms, and will therefore contain valuable information about the local environment around the the X–ray absorbing atom. The structural contents of the EXAFS spectrum becomes apparent, when written as a function of the magnitude of the photoelectron wave vector [18]:

$$\begin{aligned} \chi(k) = \sum_i N_i\, S_i(k)\, F_i(k)\, \exp\left(-2\sigma_i^2 k^2\right) \\ \times\, \exp\left(-2r_i/\lambda(k)\right) \frac{\sin\left(2kr_i + \phi_i(k)\right)}{kr_i^2} \end{aligned} \tag{2.3}$$

where $F_i(k)$ is the backscattering amplitude of the $N_i$ neighbouring atoms of type i located at a distance $r_i$ from the central atom, $2\sigma_i^2$ is the Debye–

Waller factor (disorder parameter) for these atoms, $\phi_i$ is the total phase shift due to atoms of type i. $\lambda(k)$ is the mean free path of the photoelectron and $S(k)$ is an amplitude reduction factor. This so called "shake up / shake off" parameter accounts for amplitude reductions arising from inelastic processes in the central atom (excitations of outer electrons (shake up) or ionisation (shake off)). The factor $\exp\left(-2r_i/\lambda(k)\right)$ accounts for inelastic losses due to scattering of the photoelectron wave by excitations in the surroundings of the central atom (such as phonons).

$2\sigma_i^2$ accounts for static disorder as well as for dynamic disorder due to harmonic motion of the atoms. Unlike the Debye–Waller factor encountered in X–ray diffraction, which describes disorder due to harmonic motion and is generally an anisotropic quantity, the disorder parameter $2\sigma_i^2$ only describes the mean square deviation of the distance of the $i^{th}$ neighbour from the central atom. As mentioned above, this expression assumes harmonic motion in the case of dynamic disorder and a gaussian distribution of distances in the case of static disorder and fails to describe strongly disordered systems.

The additional phase shift $\phi_i(k)$ contains contributions from both the X–ray absorbing atom and the scattering atom. The photoelectron twice experiences a phase shift at the central atom due to the potential caused by the remaining electrons, once on leaving and once on returning to the central atom after the scattering process, and the scattering process at the neighbouring atom itself causes a further phase shift.

The backscattering amplitude is solely a property of the scattering atom. It can either be derived from theoretical calculations or by fitting to EXAFS spectra of standard materials of known structure (see Section 2.1.1 below).

Expression 2.3 is derived for single electron, single scattering processes and proves to be valid in most cases since multiple scattering generally leads to long pathlengths (assuming the effective phase factor for these processes behaves as $\sin\left(2kr_{\text{eff}}\right)$, where the effective scattering path length $2r_{\text{eff}}$ is the

sum of all scattering paths beginning and ending at the central atom). This corresponds to rapidly oscillating waves in k–space which, in addition, will have small amplitudes due to the attenuation proportional to the square of the distance traversed by the photoelectron wave (Equation 2.3), and the inelastic loss factor $\exp\left(-2r_i/\lambda(k)\right)$.

In some cases, however, especially in systems containing collinear or nearly collinear arrays of atoms, multiple scattering due to direct forward scattering can lead to a noticeable enhancement of the observed amplitude. In these cases, Equation 2.3 must be modified [18] to account for all possible multiple scattering paths.

The realisation in the early 1970's, that the EXAFS function could be related to a radial distribution function proved to be a great advance in the understanding of EXAFS spectra [17, 19]. The Fourier transformation

$$\rho(r') = \frac{1}{(2\pi)^{\frac{1}{2}}} \int_{k_{min}}^{k_{max}} k^n \, \chi(k) \, \exp\left(i2kr'\right) dk \qquad (2.4)$$

relates the EXAFS function $\chi(k)$ in $k$ space to the radial distribution function $\rho(r')$ in $r$ space. The factor $k^n$ is a weighting factor applied to emphasize the higher regions in $k$ space, which are usually of low intensity. The limits of integration reflect the finite range in $k$ space within which experimental data are available.

Each peak in $\rho(r')$ represents a number of neighbouring atoms at a distance $r$ from the central atom. The peaks are shifted from the true distances $r$ by a quantity $\Delta = r - r'$, the exact magnitude of which depends not only upon the elements involved but also upon the choice of threshold energy, upon the weighting of the data and upon the disorder parameter for the particular neighbours [18]. Providing the shift $\Delta$ is known, or similar, standard compounds of known structure are available for which the shift $\Delta$ is transferable, the radial distribution function allows the distances of neighbouring atoms to

be easily determined. In addition, it is invaluable in assessing the validity of the single electron, single scattering approach for the particular problem, since multiple scattering effects are readily visible in the Fourier transformations of the EXAFS function (*vide infra*)[1] whereas they are difficult to assess from the EXAFS function alone.

## 2.1.1 Data Analysis

The initial step in the analysis of experimental data is to reduce the measured absorption coefficient to the required EXAFS spectrum according to Equation 2.1. Since the absorption coefficient of the isolated atom is generally not known, it is approximated by fitting two smooth background functions to the data. The first function accounts for the pre–edge absorption, the second accounts for absorption beyond the edge other than the sinusoidal modulations of interest. This part of the procedure was performed using the SPLINE program [20] which fits a spline function to the background. During the background subtraction, care must be taken not to introduce high frequency oscillations with the spline function. Least squares fitting of theoretical spectra was performed using the program XFIT [21, 20], incorporating the FEFF code [22] for *ab initio* calculations of theoretical EXAFS standards (phase shifts and amplitude factors). The EXAFS data were weighted with $k^3$. To minimize truncation effects when Fourier transforming the data, a window function was applied. The window consists of a region of constant value 1, the extent of which can be varied. At the boundaries of this region the window function decreases to 0. The functional form and the gradient of the edges are also variable. The following parameters were treated as refinable: the threshold

---

[1]In cases where single scattering of the photoelectron applies, a decay of the amplitude of the peaks in the Fourier transformation is evident with increasing distance. The presence of multiple scattering may increase the amplitude of the peak due to the second coordination shell to an extent, where it is equal to or even higher than the peak due to the first coordination shell

energy reference parameter, $E_o$; the distance, $r_i$, between the atoms in shell $i$ and the X-ray absorbing atom; the number of atoms, $N_i$, in shell $i$ (although in some cases (see Section 3.3) the value of $N_i$ was fixed); and the Debye–Waller factor, $2\sigma_i^2$, for shell $i$. In addition, for refinements taking multiple scattering into account, the C–N–Cd angle (for carbon and nitrogen atoms of the $Ni(CN)_4$ units) was refined. The values of $N_i$ were constrained to be equal for the carbon, nitrogen and cadmium shells of the C–N–Cd units. The inelastic energy loss parameter, $S_o^2$, was determined by fitting a simple model consisting only of the carbon and nitrogen shells (at known, fixed distances) of the $Ni(CN)_4$ unit to the low–temperature EXAFS data for 2–chlorobutane/$Cd(pn)Ni(CN)_4$. The value ($S_o^2 = 0.8494$) obtained was used as a fixed parameter in all subsequent refinements. In all refinements, the parameter $E_{oi}$ was fixed equal to zero. The goodness–of–fit factors R and $\chi^2$ used in the XFIT program are defined as follows:

$$R = \left[\frac{\sum_i \{w_i\left[\chi_i^{expt} - \chi_i^{calc}\right]\}^2}{\sum_i \left[w_i\chi_i^{expt}\right]^2}\right]^{\frac{1}{2}} \qquad (2.5)$$

$$\chi^2 = \sum_i \{w_i\left[\chi_i^{expt} - \chi_i^{calc}\right]\}^2 \qquad (2.6)$$

where $\chi_i^{expt}$ and $\chi_i^{calc}$ denote the $i^{th}$ data point in the experimental and calculated normalized EXAFS spectra, respectively, and $w_i$ is the weighting for the $i^{th}$ data point. The EXAFS data were processed without Fourier filtering to allow statistical significance testing [23] to be applied. In this approach, the addition of a new shell to the structural model is considered statistically significant if it corresponds to a sufficiently large improvement in the fit between the experimental and calculated data. The required improvement in fit

is quantified using the parameter $\xi$, which is defined as:

$$\xi = \frac{[d - 1 - p][\chi^2(a) - \chi^2(b)]}{3\chi^2(b)} \tag{2.7}$$

where d is the number of data points and p is the number of refined parameters in Model b which contains one shell more than Model a. $\chi^2$ is the goodness–of–fit factor defined in Equation 2.6. Specifically, if d is approximately 200, the additional shell in Model b is significant at the 5% confidence level if $\xi \geq$ 2.7.

It is important to note that the nickel K–edge EXAFS spectrum represents the summation of the separate spectra for the Ni[1] and Ni[2] sites; this issue has been given careful consideration in the data analysis and will be discussed in Section 3.3.

## 2.2 Theory of X–ray Powder Diffraction

X–ray diffraction is a well established technique, utilising the coherent, elastic scattering of X–rays by atoms to establish the structures of materials. Diffraction experiments can be performed either on single crystals or on powder samples, where a powder is defined as a polycrystalline entity, where the orientation of the individual crystallites is entirely random so that all possible orientations of the crystallites are present in equal proportions. Much of the following discussion is general. As, however, the relevant experiment reported in Chapter 4 is powder diffraction experiment, attention will be focussed on particular aspects of this technique.

X–rays are scattered as a result of the interaction of the electric field of the X–rays with the electric field due to the electrons surrounding the atomic nuclei. For crystalline solids, i.e. those exhibiting long range, three dimensional ordering of the constituent atoms or molecules, the result of the scattering is

a well defined interference pattern in which the positions of the maxima are described by Braggs' law, which is derived from a simple geometric argument: Constructive interference from X–rays diffracted in different locations will only occur if the diffracted X–rays are in phase. Considering diffraction as specular reflection from a set of parallel planes, it is easily seen in Figure 2.1 that the path difference $\overline{ABC}$ is equal to $2d \sin \theta$, resulting in

$$n\lambda = 2d \sin \theta \qquad (2.8)$$

where $\lambda$ is the wavelength of the X–rays, d is the spacing between lattice planes and $\theta$ is the incident angle of the X–ray with respect to the lattice plane (see Figure 2.1).

A lattice plane is a plane defined by three non–collinear points within the crystallographic coordinate system, namely those points where the plane intercepts the three crystallographic axes. However, rather than using these three points directly, it is more convenient to use the lowest set of integers with the same ratio as the reciprocal values of the intercepts. These numbers, denoted Miller indecees, are written as (hkl). A set of equidistant planes will have common Miller indices.

A further useful concept is that of the reciprocal lattice. A lattice in direct space, described by three vectors $\underline{a}_1$, $\underline{a}_2$, and $\underline{a}_3$, can be related to the reciprocal lattice defined by the three vectors

$$\underline{b}_1 = \frac{\underline{a}_2 \times \underline{a}_3}{\underline{a}_1 \cdot \underline{a}_2 \times \underline{a}_3}$$

$$\underline{b}_2 = \frac{\underline{a}_3 \times \underline{a}_1}{\underline{a}_1 \cdot \underline{a}_2 \times \underline{a}_3} \qquad (2.9)$$

and

$$\underline{b}_3 = \frac{\underline{a}_1 \times \underline{a}_2}{\underline{a}_1 \cdot \underline{a}_2 \times \underline{a}_3}$$

From this definition, it is clear that each of the reciprocal lattice vectors is orthogonal to two of the direct lattice vectors.

A vector in the reciprocal lattice is given by

$$\underline{S} = h\underline{b}_1 + k\underline{b}_2 + l\underline{b}_3 \tag{2.10}$$

where the components of the vector $\underline{S}$ are related to the Miller indices mentioned above inasmuch as the reciprocal lattice vector is perpendicular to the lattice plane described by the same indices.
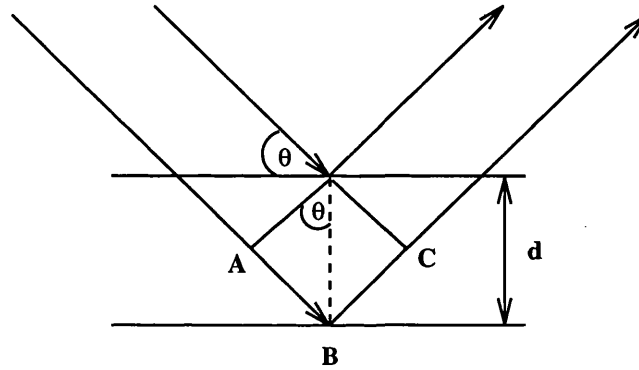
**Figure 2.1:** Reflection of X–rays from two lattice planes

For a powder sample, the Bragg condition will be fulfilled for many of the crystallites at any given time. The diffraction maxima lie on cones with the incident beam as their axis and a vertical angle of $2\theta$. The number of symmetry related planes which contribute to the intensity of a given diffraction maximum is called the multiplicity of the reflection. It must be noted that, in some cases, maxima may contain intensity from planes with identical d spacing that are not related by symmetry.

Bragg's law only contains information regarding the symmetry of the crystal lattice. With the appropriate expression for the lattice spacing d, the crystal class and lattice parameters of the crystal can be determined from the positions of the diffraction maxima.

The position and arrangement of the constituent atoms can be deduced

from the intensity $\mathcal{I}$ of the diffraction maxima, which, for an ideally imperfect crystal, is given by [24]:

$$\mathcal{I} = C \, \exp\left(-W\right) \mathcal{F}^2 \tag{2.11}$$

where C contains a number of geometric correction factors, discussed in more detail below, $\exp\left(-W\right)$ is the temperature factor and $\mathcal{F}$ is the structure factor. Thermal energy, on an atomic scale, is energy of motion and hence a crystal will not represent a collection of rigid atoms. Thermal motion of atoms will lead to an attenuation of the observed intensity, which is accounted for by the temperature factor. For isotropic, harmonic motion about an equilibrium position, the Debye–Waller factor W can be expressed as

$$W = \frac{8}{3}\pi < u_{iso} >^2 \frac{\sin^2 \theta}{\lambda} \tag{2.12}$$

where $< u_{iso} >^2$ is the mean square displacement of the relevant atom and the other factors take their usual meaning.

The structure factor $\mathcal{F}$ is given by:

$$\mathcal{F}^{hkl} = \sum_i f_i^{hkl} \exp\left(2i\pi(hx_i + ky_i + lz_i)\right) \tag{2.13}$$

where $x_i$, $y_i$, and $z_i$ are the coordinates of the $i^{th}$ atom in the unit cell and $f_i$ is the atomic scattering factor for atoms of type $i$. $hkl$ are the Miller indices denoting a given lattice plane. The sum runs over all atoms $i$ in the unit cell. The scattering factor itself depends upon the scattering angle $\theta$ and is defined such that, at $\theta = 0$, $f_i$ is equal to the number of electrons contained in the atom or ion.

The structure factor is related to the electron density of the crystal. As the structure factor only exists at discrete points (i.e. at reciprocal lattice points), the integral form of the Fourier transformation can be substituted by

the summation

$$\rho(xyz) = \frac{1}{V} \sum_{h=-\infty}^{\infty} \sum_{k=-\infty}^{\infty} \sum_{l=-\infty}^{\infty} \mathcal{F}^{hkl} \exp\left(-2\pi i(hx + ky + lz)\right)$$

$$(2.14)$$

A graphical representation of the electron density $\rho(xyz)$ will give a direct indication of the positions of atoms in the unit cell. However, it cannot be calculated directly from the measured intensities of the diffraction maxima. This can be seen by rewriting the structure factor using simple properties of complex numbers

$$\mathcal{F}^{hkl} = \mathcal{A}^{hkl} + i\mathcal{B}^{hkl} \qquad (2.15)$$

where

$$\mathcal{A}^{hkl} = \sum_{j} f_j \cos\left(2\pi(hx_j + ky_j + lz_j)\right) \qquad (2.16)$$

and

$$\mathcal{B}^{hkl} = \sum_{j} f_j \sin\left(2\pi(hx_j + ky_j + lz_j)\right) \qquad (2.17)$$

the phase angle $\phi$ is defined by

$$\tan\phi = \frac{\mathcal{B}^{hkl}}{\mathcal{A}^{hkl}} \qquad (2.18)$$

and the structure factor can be written as

$$\mathcal{F}^{hkl} = |\mathcal{F}^{hkl}| \exp\left(i\phi\right) \qquad (2.19)$$

Inserting Equation 2.19 into the equation for the electron density (Equation 2.14), it can be seen that the Fourier transformation cannot be fully

determined from the experimental data alone, since the phase angle $\phi$ is unknown.

It is therefore necessary to compare a diffraction pattern calculated from a structural model with the experimental data. Once a sufficiently good, partial model has been determined, the information contained in this model can be used to calculate difference Fourier maps to locate further atoms in the crystal structure. The initial structural model can be obtained either by using a sufficiently similar known structure and refining this model (this procedure was applied in Chapter 4, where the Rietveld method [25] of whole profile refinement was used to refine the low temperature structure from an initial model derived from the high temperature structure). or by solving the structure using conventional methods.

Since structure solution was not applied, methods of solving unknown structures will not be discussed.

The exact nature of $C$ (Equation 2.11) is determined by the experimental geometry. Several components depend on the scattering geometry, whereas others are independent of the scattering geometry. Those factors independent of the experimental geometry are:

**Multiplicity** Any reflection in an X-ray powder diffractogram will contain intensity contributions from lattice planes with nominally different $hkl$, which are related by symmetry. These symmetry equivalent planes will have an identical $d$ spacing, thus fulfilling the Bragg condition at the same diffraction angle. The number of symmetry equivalent planes is termed the multiplicity.

**Polarisation Factor** The polarisation factor accounts for the polarisation dependence of the scattering. The polarisation of the X-rays incident on the sample will depend upon the both the nature of the source of the photons as well as instrumental factors such as the presence of optical components.

Those correction factors which depend upon the scattering geometry are:

**Lorentz Factor**   The Lorentz factor expresses the relative amount of time a reciprocal lattice point spends in a reflecting position. As such it depends upon the experimental geometry. This factor derives from the fact that for an imperfect crystal, reflection will occur over a small angular range, rather than exactly and only at the Bragg angle.

**Absorption Correction**   This factor accounts for absorption of X–rays by crystals and depends upon the sample shape and size.

**Preferred Orientation**   In the case of a powder sample of small volume or relatively large crystallite size, preferred orientation of the crystallites will lead to a non–random distribution of crystal orientations. As a result, some peaks have enhanced intensities. For crystals with needle or plate morphology this behaviour is frequently encountered. The approach for calculating the effect of preferred orientation described by March and Dollase [26, 27] is implemented in the software used here.

**Line Shape**   The line shape of the experimentally observed diffraction maxima depends upon the experimental geometry as well as on properties of the sample. Several different line shape functions suitable for various experimental conditions have been developed. A detailed discussion of such functions can be found in references [28, 29]. Those implemented in the software used for analysing the present data are also discussed in reference [30] and will be mentioned in Section 2.2.2.

The measured diffraction intensities, following application of these correction factors, are proportional to $\mathcal{F}^2$, as required for determining the crystal structure.

## 2.2.1 Rationalisation of Structural Changes at the Phase Transition

The initial task in the analysis of any diffraction pattern is to determine the lattice parameters and the metric symmetry of the lattice from the positions of the diffraction maxima. Once these parameters have been determined, the space group describing the crystal symmetry can be determined, or (as is more often the case) can be narrowed down to a small number of possible space groups on the basis of the Laue symmetry and the conditions for systematic absences.

Several programs exist for the purpose of indexing powder patterns, allowing the lattice parameters to be determined automatically on the basis of the observed positions of the diffraction maxima [31, 32, 33]. The lattice parameters these programs produce depend upon the peak positions being determined precisely and accurately. A number of experimental factors, such as diffractometer zero point shift or peak asymmetry, will result in an effective shift of the observed peak maximum from the true Bragg angle. Indexing programs, therefore, compare the peak positions calculated for a given lattice with the experimental positions and assign a figure of merit based on the deviation of the two. Only those sets of parameters with a figure of merit greater than a given value will be reported. For low symmetry phases this can often result in a substantial number of sets of lattice parameters with similar figures of merit. It is then up to the experimentalist to determine which is the correct set of lattice parameters.

For the experiment described in Chapter 4, the problems associated with automated indexing programs were avoided by using further information contained in the diffractograms (as described below) and indexing the pattern manually. A similar approach has been reported recently [34] in the investigation of a low temperature phase transition in the urea/n–hexadecane inclusion

compound.

As mentioned in the previous section, a single peak may contain intensity contributions from several lattice planes. For reasons of symmetry, there will exist a set of lattice planes for which the Bragg condition is fulfilled at the same scattering angle. This set of lattice planes constitutes a form in the holosymmetric point group of the crystal system. It is possible for several forms to correspond to the same scattering angle, although such accidental equivalence is ignored in the following discussion. If the point group of the crystal is the same as the holosymmetric point group of the crystal system, each individual reflection contributing to a given peak will have the same intensity.

If the symmetry of the crystal is reduced to a lower symmetry crystal system, the set of lattice planes constituting a form in the higher symmetry will now, in general, constitute several forms in the holosymmetric point group of the lower symmetry crystal system. Providing the change in symmetry is associated with a change in lattice parameters, the Bragg angle for reflections corresponding to each of these forms will be different, and hence a splitting of peaks will be observed upon lowering the symmetry. If the geometric transformation relating the high and low symmetry lattices is known, the splitting can be predicted readily. Clearly, the manner in which the diffraction maxima in the high symmetry phase separate in the low symmetry phase conveys valuable information regarding the nature of the transition.

It is reasonable to assume that the distribution of scattering matter will not be substantially different in the high and low symmetry phases. Under this assumption, the sum of the intensities of the peaks in the low symmetry phase emanating from a given peak in the high symmetry phase will be approximately the same as the intensity of the original peak. Additionally, if the point group symmetry of both phases is that of the holosymmetric point group of the respective crystal class, the ratio of the intensities of a set of previously

equivalent reflections will be determined by the ratio of the multiplicities of these reflections.

## 2.2.2 Data Analysis

All diffractograms were indexed manually using the appropriate quadratic expansions of Bragg's law (Equation 2.8).

The Rietveld refinement calculations on the diffraction data obtained from the Synchrotron Radiation Source, Daresbury were performed using the GSAS suite of programs [30, 35].

In the first instance, a whole profile fit was performed using the LeBail method [36]. This method does not require a structural model and was used to extract the peak shape parameters for the experimental diffraction maxima. The peak shape function chosen was the modified Thompson–Cox–Hastings pseudo–Voigt function [29, 30, 37], representing a linear combination of a Gaussian ($\mathcal{G}$) function and a Lorentzian ($\mathcal{L}$) function [28]:

$$\mathcal{S}_p = \eta \mathcal{G} + (1 - \eta)\mathcal{L} \qquad (2.20)$$

The mixing parameter $\eta$ is a function of both the Gaussian width parameter and Lorentzian width parameter (which in turn are functions of the scattering angle).

Refinements using structural models were carried out after determining the line shape parameters using the Rietveld method [29, 25, 38]. Rather than attempting to assign well defined intensities to individual peaks in the diffraction pattern, in this method the whole diffraction profile is calculated according to Equation 2.11 for a given structural model for every experimental data point. The structural model is refined by minimising the difference between the calculated and observed diffraction profiles for all points simultaneously. The quality of the refinement depends very much upon the correct

choice of line shape function, as well as upon the quality of the experimental data.

The refinable parameters can be divided into two groups. The first constitutes those parameters that do not depend upon the structure. These are the line shape parameters, the experimental background scattering, the $2\theta$ zero–point shift as well as sample absorption, preferred orientation parameters and scale factors.

The second group comprises the lattice parameters, the fractional coordinates, as well as atomic displacement factors and site occupancies of the individual atoms.

For the experimental data presented here, the background was not modelled by a function with refinable parameters due to the obvious scattering from the amorphous film used to cover the sample (see Figure 4.2). Instead, individual points on the diffractogram were selected manually, and the background scattering was approximated by linear interpolation between these points.

## 2.3 Neutron Scattering

Neutrons are a versatile tool in the study of condensed matter. Neutrons obtained from typical, dedicated sources have energies of the order of several meV and the associated de Broglie wavelengths are of the order of a few Ångstrom. The energies of these neutrons are comparable to those of excitations in the solid state (i.e. molecular reorientations, vibrations or collective excitations), whereas their wavelengths are comparable to interatomic spacings. Both spectroscopic studies and diffraction experiments are thus feasible. In contrast, photons of comparable wavelengths (i.e the X–ray region of the electromagnetic spectrum) have energies of several thousand eV and scattering processes are elastic. Electromagnetic radiation with energies comparable to those of molecular excitations (in the infrared region), on the other hand, have

wavelengths of several thousand Ångstrom and are unsuitable for conventional diffraction experiments.

Neutron scattering can be broadly subdivided into three areas, namely diffraction, inelastic scattering and quasielastic scattering. It is the latter on which this section will focus. The discussion herein is only intended as a brief introduction to some basic concepts required to understand the technique and the information to be gained from its use. For a more detailed discussion of neutron scattering, the reader is referred to Squires [39] and Lovesey [40].

### 2.3.1   Basic Concepts

The neutron is a spin $\frac{1}{2}$ particle with a mass of $m_n = 1.675 \times 10^{-27}$ kg and zero charge. The velocities of neutrons from a typical source are much less than the velocity of light, they can be treated as non–relativistic particles. The energy of a free neutron is then given by its kinetic energy

$$E = \frac{1}{2} m_n v^2 \qquad (2.21)$$

where $v$ is the velocity of the neutron. From this it follows that the momentum of the neutron is

$$p = \sqrt{2m_n E} \qquad (2.22)$$

The de Broglie wavelength $\lambda$ of the neutron is then given by

$$\lambda = \frac{h}{p} = \frac{h}{\sqrt{2m_n E}} \qquad (2.23)$$

with which one can define the neutron wavevector $\underline{k}$, the magnitude of which is given by

$$k = \frac{2\pi}{\lambda} \qquad (2.24)$$

The direction of the wavevector is given by the direction of propagation of the neutron. The wavevector is related to the momentum of the neutron *via* the equation

$$p = \hbar k \qquad (2.25)$$

h denotes Planck's constant, $\hbar$ is $h/2\pi$. The neutron also possesses a magnetic moment, the interaction of which with magnetic atoms leads to magnetic scattering. As magnetic scattering is not relevant here, it is not discussed any further.

The other relevant interaction between neutrons and matter, resulting in scattering, is that between the neutron and nuclei. Since the neutron has zero charge, it does not experience any coulombic interaction and can therefore penetrate the electron shell and come close to the nucleus.

The interaction between the neutron and the nucleus is strong, but of short range compared to the wavelength of the neutron. It can therefore be described by a single parameter, the scattering length $b$. The scattering length varies from isotope to isotope and is not a monotonic function of any known nuclear property. Scattering lengths of isotopes of the same element can vary substantially [41], which allows specific sites of a given molecule to be differentiated by means of selective isotopic substitution. In addition, the scattering length of light elements may be quite large, thus making them relatively easier to distinguish in neutron diffraction experiments, for example, than by X–ray diffraction, for which the scattering power increases monotonically with the atomic number.

The scattering length is a property of the compound neutron–nucleus and depends upon the total spin state of the system. For a nucleus with non–zero spin $I$, there are two possible compound systems with spin states $I + \frac{1}{2}$ and $I - \frac{1}{2}$, with different scattering lengths $b^{+}$ and $b^{-}$, respectively. When

considering a macroscopic system, the average over all distributions of nuclei $i$ with scattering length $b_i$ must be taken. This naturally leads to the separation of two contributions to the total scattering. One contribution, the coherent scattering, is associated with the average of the scattering length, where

$$b^2_{\text{coh}} = <b^2_i>$$ (2.26)

The other contribution, incoherent scattering, is associated with the mean deviation of the scattering length $b_i$ from the coherent scattering length

$$b^2_{\text{inc}} = <b^2_i> - <b_i>^2$$ (2.27)

With these definitions the scattering cross section $\sigma$ is defined as

$$\sigma_{\text{coh}} = 4\pi\, b^2_{\text{coh}}$$ (2.28)

$$\sigma_{\text{inc}} = 4\pi\, b^2_{\text{inc}}$$ (2.29)

Coherent scattering gives interference effects and as such contains information about the correlation between different nuclei. Incoherent scattering, on the other hand, does not give interference effects and yields only the self correlation of a single nucleus.

The experiments described in Chapters 5 and 6 were carried out using samples containing a substantial amount of the $^1$H isotope. This isotope has a very large incoherent scattering cross section [41] and incoherent scattering by the $^1$H–nuclei therefore dominates the experimental spectra. As a result, the incoherent scattering arising from other nuclei in the system can be neglected and will not be discussed in any detail in the remainder of this section.

## 2.3.2 Incoherent Quasielastic Neutron Scattering (IQNS)

In the spectrum of neutrons scattered from a material, the quasielastic scattering is the region within a few meV of, and centred upon, the elastic scattering line. Figure 2.2 shows a schematic representation of a scattering experiment.

The incident neutron with wavevector $k_i$ is scattered by the sample and detected by a detector covering a small solid angle $d\Omega$. The final wavevector is $k_f$. In an experiment with energy discrimination, the measured quantity is the (incoherent) partial differential cross section

$$\left[\frac{d^2\sigma}{d\Omega\,dE}\right]_{\text{inc}} = \frac{1}{4\pi}\frac{k_f}{k_i}\,\sigma_{\text{inc}}\,S_{\text{inc}}(\underline{Q},\omega) \tag{2.30}$$

which describes the effective scattering cross section for neutrons scattered into a small solid angle $d\Omega$ and with an energy in the range $E$ to $E + dE$. $S_{\text{inc}}(\underline{Q},\omega)$ is the scattering function for incoherent scattering, which is discussed in detail in the following section. Clearly, by integrating over $d\Omega$ and $dE$, the scattering cross section as defined above (Equation 2.29) is retrieved.
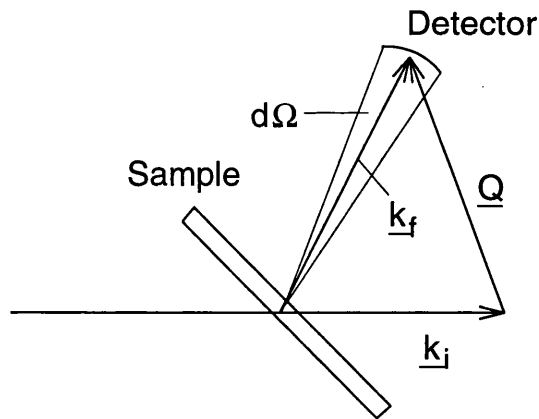


**Figure 2.2:** Schematic diagram of a scattering experiment. The incident neutron with wavevector $k_i$ is scattered at the sample and detected at a detector covering a small solid angle $d\Omega$. The final wavevector of the neutron is $k_f$ and the scattering vector is Q (see text)

The scattering function is the main quantity of interest. It depends upon: (1) the scattering vector $\underline{Q}$, which is defined as the vectorial difference between the final and the incident neutron wave vectors

$$\underline{Q} = \underline{k}_f - \underline{k}_i \qquad (2.31)$$

thus representing the momentum transfer during the scattering process ($\Delta\underline{p} = \hbar\underline{Q}$), and (2) the energy transfer $\hbar\omega$ during the scattering process, which is given by the difference between the final and the incident neutron energies

$$\hbar\omega = E_f - E_i = \frac{\hbar^2}{2m_n}\left(k_f^2 - k_i^2\right) \qquad (2.32)$$

The dependence of the scattering function upon both of these quantities means that it contains not only information about the correlation times of molecular motions, but also about the spatial extent of such motion. Clearly, for elastic scattering ($\hbar\omega = 0$), the magnitude of the incident neutron wavevector is identical to the magnitude of the final neutron wavevector. The momentum transfer is not independent of the energy transfer. However, as the energy transfers observed in an IQNS experiment are generally small compared to the neutron energies, the approximation $k_f = k_i$ is usually applied and hence the momentum transfer/wavevector is determined solely by the scattering angle.

### 2.3.3 Scattering and Correlation Functions

The experimentally determined scattering function is given explicitly by

$$S^{\mathrm{expt}}(\underline{Q},\omega) = \exp\left(-\hbar\omega/k_bT\right)S_{\mathrm{inc}}(\underline{Q},\omega)\otimes\mathcal{R}(\omega) + B \qquad (2.33)$$

where $k_b$ is the Boltzmann constant, $B$ is the background scattering, and $\exp\left(-\hbar\omega/k_bT\right)$ is the detailed balance factor. $S_{\mathrm{inc}}(\underline{Q},\omega)$ is the scattering func-

tion, which depends upon details of the system under investigation. The scattering function is convoluted with the instrumental resolution function $\mathcal{R}(\omega)$ (the convolution is denoted by $\otimes$). The detailed balance factor accounts for the asymmetry in the distribution of (energy) states in the system: the scattering function is a symmetric function,

$$S(\underline{Q}, \omega) = S(-\underline{Q}, -\omega) \tag{2.34}$$

i.e. the *a priori* probability that a neutron with an energy of $\hbar\omega$ will effect a transition between two states of the system separated by the same energy is independent of the direction of the transition. However, the probability that the system will initially be in the higher energy state will be lower by a factor $\exp(-\hbar\omega/k_b T)$ than the probability that it will be in the lower energy state.

Van Hove [42] first suggested describing the scattering function $S(\underline{Q}, \omega)$ in terms of the correlation function $G(\underline{r}, t)$. The correlation function is related to the scattering function by a double Fourier transformation involving $\underline{r}$ and $t$. In this respect it is useful to define a third function, the intermediate scattering function $I(\underline{Q}, t)$, which represents the Fourier transformation of $G(\underline{r}, t)$ with respect to $\underline{r}$. The full set of functions is then

$$I(\underline{Q}, t) = \int G(\underline{r}, t) \exp(i\underline{Q}.\underline{r}) \, dr \tag{2.35}$$

$$S(\underline{Q}, \omega) = \frac{1}{2\pi\hbar} \int I(\underline{Q}, t) \exp(-i\omega t) dt \tag{2.36}$$

The correlation function relevant to incoherent quasielastic neutron scattering is the self pair–correlation function

$$G_s(\underline{r}, t) = <\delta(\underline{r} - \underline{R}_0(t) + \underline{R}_0(0))> \tag{2.37}$$

which describes the conditional probability of a particle being found at $\underline{r}$ at time $t$ if the same particle was at the origin $\underline{R}_0$ at time $t = 0$. $G_s(\underline{r}, t)$ must

therefore satisfy the normalization condition

$$\int G_s(\underline{r}, t)\, d\underline{r} = 1 \tag{2.38}$$

The brackets $<>$ in Equation 2.37 denote the thermal average, i.e. the average over all initial states of the system at a given temperature.

In the case of incoherent scattering, the intermediate scattering function can be generalized as

$$I_{\text{inc}}(\underline{Q}, t) = \frac{1}{N} \sum_i b_{\text{inc}} < \exp\left(i\underline{Q}.\underline{r_i}(t)\right) \exp\left(-i\underline{Q}.\underline{r_i}(0)\right) > \tag{2.39}$$

where the sum runs over all particles $i$ and N is the total number of particles. $I_{\text{inc}}(\underline{Q}, t)$ therefore represents the average over all scatterers $i$, and decomposes into two parts

$$I_{\text{inc}}(\underline{Q}, t) = I_{\text{inc}}(\underline{Q}, \infty) + I'_{\text{inc}}(\underline{Q}, t) \tag{2.40}$$

which, upon Fourier transformation, become

$$S_{\text{inc}}(\underline{Q}, \omega) = I_{\text{inc}}(\underline{Q}, \infty)\delta(\omega) + S'_{\text{inc}}(\underline{Q}, \omega) \tag{2.41}$$

The intermediate scattering function evaluated at infinite time clearly represents the elastic part of the total scattering upon which the time dependent, inelastic scattering is superimposed.

The vector $\underline{r}(t)$ can be written as

$$\underline{r}(t) = \underline{r}^{\text{vib}}(t) + \underline{r}^{\text{rot}}(t) + \underline{r}^{\text{trans}}(t) \tag{2.42}$$

where the superscripts vib, rot and trans represent those parts of $\underline{r}$ due to vibrational, rotational and translational motion, respectively. The separation

of the individual contributions assumes that the different types of motion are independent of each other.

The intermediate scattering function then becomes

$$I_{\text{inc}}(\underline{Q},t) = I_{\text{inc}}^{\text{vib}}(\underline{Q},t) \times I_{\text{inc}}^{\text{rot}}(\underline{Q},t) \times I_{\text{inc}}^{\text{trans}}(\underline{Q},t) \qquad (2.43)$$

and Fourier tranformation of Equation 2.43 results in

$$S_{\text{inc}}(\underline{Q},\omega) = S_{\text{inc}}^{\text{vib}}(\underline{Q},\omega) \otimes S_{\text{inc}}^{\text{rot}}(\underline{Q},\omega) \otimes S_{\text{inc}}^{\text{trans}}(\underline{Q},\omega) \qquad (2.44)$$

The total scattering function is the convolution of the vibrational, rotational and translational scattering functions.

In the quasielastic region ($|\hbar\omega| \lesssim 2$ meV), the vibrational part can be treated as small amplitude, harmonic motion and is then given by the Debye–Waller factor

$$S_{\text{inc}}^{\text{vib}} = \exp\left(-Q^2 <u^2>\right) \qquad (2.45)$$

where $<u^2>$ is the mean square displacement of the oscillating particle. As it is independent of the energy transfer, the Debye-Waller factor reduces to a factor in Equation 2.44.

The exact expressions of the rotational and translational scattering factors depends upon the nature of the motion. To describe these parts of the scattering function requires a dynamic model, from which the functions are derived (see also Appendix A). In general, if there is no correlation between the motions of distinct particles, the scattering functions take the form

$$S_{\text{inc}}^{\text{rot/trans}}(\underline{Q},\omega) = A_0^{\text{rot/trans}}(\underline{Q})\,\delta(\omega) + \sum_i A_i^{\text{rot/trans}}(\underline{Q})\mathcal{L}_i(\omega)$$

$$(2.46)$$

where $A_0(\underline{Q})$ is the elastic incoherent structure factor (EISF) and the $A_i(\underline{Q})$ are the amplitudes of the Lorentzian functions $\mathcal{L}_i(\omega)$. $\delta(\omega)$ is Dirac's delta function in $\omega$. The number of terms $i$ in the summation depends upon the dynamic model. The EISF and the amplitudes of the Lorentzian function convey information on the geometry of the motion whereas the Lorentzian functions describe the temporal aspects of the dynamics. They represent the Fourier transformation of exponential functions describing the motion in the time–domain (see Appendix A). The half width at half maximum (HWHM) of the Lorentian functions are related to the correlation times $\tau$ of the motion. Exponential decay of the dynamics arises when the motion of a single ^{1}H nucleus is not correlated with the motion of other, structurally independent ^{1}H nuclei in the system.

Comparison with Equation 2.40 reveals that the EISF is equivalent to the intermediate scattering function evaluated at infinite time. It can be written as

$$A_0(\underline{Q}) \; = \; \frac{I^{\mathrm{el}}_{\mathrm{inc}}(\underline{Q})}{I^{\mathrm{el}}_{\mathrm{inc}}(\underline{Q}) \, + \, I^{\mathrm{qe}}_{\mathrm{inc}}(\underline{Q})} \qquad (2.47)$$

where $I$ denotes intensity and the superscripts el and qe denote the elastic and quasielastic parts thereof. From this description it follows that the EISF represents the fraction of elastic scattering with respect to the total intensity (within the experimental energy window). The importance of the EISF is that it gives direct information on the nature of the observed motion, both in terms of geometrical features of the motion (*via* its $Q$–dependence) and in terms of its temperature dependence. The correlation times of the relevant dynamic processes can be deduced from the widths of the Lorentzian functions $\mathcal{L}_i(\omega)$.

Scattering functions are evaluated from the intermediate scattering func-

tion written as

$$I(\underline{Q},t) = \iint \exp\left(-i\underline{Q}.[\underline{r_t} - \underline{r_0}]\right) P(\Omega, t : \Omega_0, 0) \, P(\Omega_0) \, d\Omega \, d\Omega_0$$

(2.48)

where $P(\Omega, t : \Omega_0, 0)$ is the conditional probability of finding a particle at a position given by $\Omega$ at a time $t$ if the same particle was at the position $\Omega_0$ at time $t = 0$. $P(\Omega_0)$ is the distribution of all initial positions. The functions $P(\Omega, t : \Omega_0, 0)$ and $P(\Omega_0)$ are determined from a dynamic model and some examples of derivations are given in Appendix A. The models used in this work are discussed in the appropriate chapters in greater detail.

The Fourier transformation of $I(\underline{Q}, t)$ with respect to $t$, after any additional averaging required by experimental considerations, gives the required scattering function $S(\underline{Q}, \omega)$.

The intermediate scattering function (Equation 2.48) contains the scalar product of the scattering vector $\underline{Q}$ and the position vector $\underline{r}$. To properly account for the relative orientations of these vectors, the intermediate scattering function must be averaged over all possible orientations of the position vector $\underline{r}$. The resulting scattering function therefore differs, depending upon whether the sample is polycrystalline, semi–oriented or oriented. Averaging procedures are discussed in Appendix A.

## 2.3.4 Multiple Scattering

If the experimental transmission is low (e.g. less than *ca.* 0.9), it may be necessary to consider the effects of multiple scattering in analysis of IQNS data, as multiple scattering affects both the intensity and lineshape of the experimental IQNS spectrum. To take multiple scattering into account, the effective

scattering law $S_{\text{eff}}(\underline{Q},\omega)$ can be expanded to a sum of contributions [43]:

$$S_{\text{eff}}(\underline{Q},\omega) = \sum_{i=1}^{\infty} S_i(\underline{Q},\omega) \tag{2.49}$$

where $S_i(\underline{Q},\omega)$ describes the contribution from neutrons scattered $i$ times. The higher order contributions can be generalized as:

$$S_i(\underline{Q},\omega) = \left[\frac{n\sigma_{\text{inc}}}{4\pi}\right]^{i-1} \int \cdots \int d\Omega_1 d\omega_1 \ldots d\Omega_{i-1} d\omega_{i-1}$$

$$S_{\text{rot}}\underline{Q}_1,\omega_1 \ldots S_{\text{rot}}\underline{Q}_i,\omega_i \times H_i(\underline{Q}_1,\ldots,\underline{Q}_i,\omega_1,\ldots,\omega_i) \tag{2.50}$$

where the subscripts $1,\ldots,i-1,i$ denote respectively variables after the $1^{st},\ldots,(i-1)^{th},i^{th}$ scattering, $\sigma_{\text{inc}}$ is the incoherent neutron scattering cross-section, n represents the number of atoms per unit volume, $\Omega_i$ defines the orientation of the momentum transfer vector $\underline{Q}_i$, and $H_i$ is the transmission factor for the $i^{th}$ scattering. Writing the individual scattering functions in terms of the specific dynamic model being considered, the integral in Equation 2.50 separates into sums of contributions (as illustrated in Equations 2.52 and 2.54) representing different combinations of elastic and inelastic scattering. The expressions for the multiple scattering functions can be simplified greatly [44] if, in the quasielastic region, the momentum transfer vector is considered to be approximately constant. In the following, multiple scattering higher than third order is neglected. The first order scattering is given by:

$$S_1(\underline{Q},\omega) = S_{\text{rot}}(\underline{Q},\omega)H_1(\phi_0,\phi), \tag{2.51}$$

where $\phi_0$ represents the angle between the incident neutron wavevector and the normal to the plane of the sample holder and $\phi$ is the angle between the scattered neutron wavevector and the normal to the plane of the sample holder (Figure 2.3).
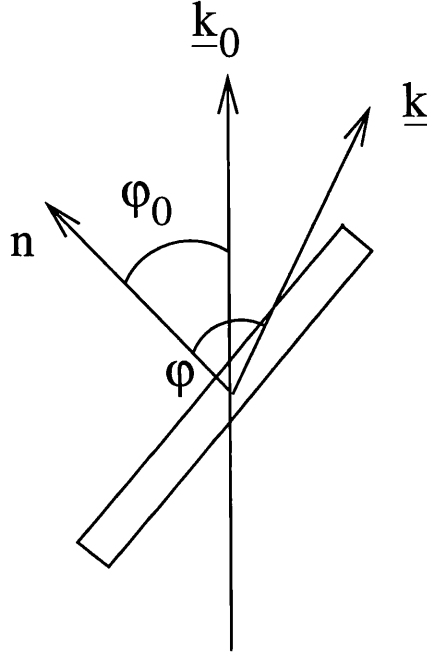
**Figure 2.3:** Schematic diagram of the general scattering geometry in a neutron scattering experiment. $\phi_0$ is the angle between the incident neutron wavevector and the normal to the plane of the sample holder, $\phi$ is the angle between the scattered neutron wavevector and the normal to the plane of the sample holder.

The second order scattering is given by

$$
\begin{aligned}
S_2(\underline{Q}, \omega) = \; & B_{00}(\underline{Q})\delta(\omega) \\
& + \sum_{i=1}^{N} (B_{0i}(\underline{Q}) + B_{i0}(\underline{Q}))\mathcal{L}_i(\omega) \\
& + \sum_{i=1}^{N} \sum_{j=1}^{N} B_{ij}(\underline{Q})\mathcal{L}_{ij}(\omega)
\end{aligned}
\tag{2.52}
$$

with

$$
B_{ij}(\underline{Q}) = \frac{n\sigma_{inc}}{4\pi} \int d\Omega_1 A_i(\underline{Q}_1) A_j(\underline{Q}_2) H_2(\phi_0\phi_1\phi)
\tag{2.53}
$$

where $\phi_1$ is the angle between the wavevector of the first order scattered neutron and the normal to the plane of the sample container and $\mathcal{L}_{ij}(\omega)$ denote

Lorentzian functions with HWHM $= \Delta_i + \Delta_j$. The structure factors $A_i(\underline{Q})$ are those defined in Equation 2.46.

The third order scattering is given by

$$
\begin{aligned}
S_3(\underline{Q}, \omega) \; = \; & C_{000}(\underline{Q})\delta(\omega) \\
& + \sum_{i=1}^{N}(C_{00i}(\underline{Q}) + C_{0i0}(\underline{Q}) + C_{i00}(\underline{Q}))\mathcal{L}_i(\omega) \\
& + \sum_{i=1}^{N}\sum_{j=1}^{N}(C_{0ij}(\underline{Q}) + C_{i0j}(\underline{Q}) + C_{ij0}(\underline{Q})\mathcal{L}_{ij}(\omega) \\
& + \sum_{i=1}^{N}\sum_{j=1}^{N}\sum_{k=1}^{N} C_{ijk}(\underline{Q})\mathcal{L}_{ijk}(\omega)
\end{aligned}
\tag{2.54}
$$

with

$$
C_{ijk}(\underline{Q}) \; = \; \left[\frac{n\sigma_{inc}}{4\pi}\right]^2 \iint d\Omega_1 d\Omega_2 A_i(\underline{Q}_1)A_j(\underline{Q}_2)A_k(\underline{Q}_3)H_3(\phi_0\phi_1\phi_2\phi)
\tag{2.55}
$$

where $\phi_2$ is the angle between the wavevector of the second order scattered neutron and the normal to the plane of the sample holder and $\mathcal{L}_{ijk}(\omega)$ are Lorentzian functions with HWHM $= \Delta_i + \Delta_j + \Delta_k$.

The EISF corrected for multiple scattering for a polycrystalline sample is:

$$
A_0(\underline{Q}) \; = \; \frac{H_1(\phi_0\phi)A_0(\underline{Q}) + B_{00}(\underline{Q}) + C_{000}(\underline{Q})}{H_1(\phi_0\phi) + \sum_{i=1}^{N}\sum_{j=1}^{N} B_{ij}(\underline{Q}) + \sum_{i=1}^{N}\sum_{j=1}^{N}\sum_{k=1}^{N} C_{ijk}(\underline{Q})}
\tag{2.56}
$$

As required, Equation 2.56 reduces to $A_0(\underline{Q})$ when multiple scattering becomes negligible.

## 2.3.5 Experimental Considerations and Data Analysis

During a scattering experiment it is common to collect data for an empty sample can as well as for a vanadium sample of the same dimensions as the sample under investigation. The material generally used for sample cans is aluminium, since its scattering cross section and its absorption cross section are small [41]. In addition, it is possible to manufacture windows with a thickness of the order of a few hundred $\mu m$, thus minimizing the effects of scattering from the experimental environment.

Vanadium (in particular the isotope $^{51}V$, which has a natural abundance of $> 99\%$ ), like hydrogen, is a predominantly incoherent scatterer, and is used to normalize the detectors. Due to the normalization condition (Equation 2.38) the integrated intensity from an incoherent scatterer is constant. As vanadium comprises an atomic crystal, reorientational motion resulting in a broadening of the elastic line is not observed in a neutron scattering experiment and the scattering within the experimental energy range is entirely elastic. Thus by integrating the observed intensities of a vanadium standard, any discrepancies due to detector inefficiency can be accounted for.

The raw scattering data represent the partial differential scattering cross section of the sample under investigation (*vide infra*). After subtracting the scattering due to the aluminium sample can and normalising the data to a vanadium standard, the data are reduced to the required scattering function *via* Equation 2.30. The scattering function is then analysed in terms of a dynamic model (see Chapters 5 and 6 as well as Appendix A) by fitting the theoretical scattering function predicted for a given model to the experimental spectra using standard least squares fitting routines.

# Chapter 3

# EXAFS Studies of *Catena*-[(1,2-diaminopropane)-cadmium(II)-tetra-$\mu$-cyano-nickelate(II)] Inclusion Compounds

## Abstract

Nickel K–edge EXAFS spectroscopy has been employed to study inclusion compounds of *catena*-[(1,2-diaminopropane)-cadmium(II)-tetra-$\mu$-cyanonickelate(II)] containing halogenoalkane guest molecules. Inclusion compounds containing 2-chlorobutane, 2-bromobutane, 2,3-dichlorobutane, 2,3-dibromobutane, 1,2-dichloroethane, and 1,2-dibromoethane were studied at 295 K and *ca.* 120 K. For these inclusion compounds there are ambiguities in the interpretation of the atomic positions attributed to the guest molecules by diffraction based studies, and the work presented here has allowed an assessment of the scope of EXAFS spectroscopy for probing the host–guest in-

teraction in such situations. The optimum approach for handling the host substructure within the EXAFS data analysis has also been assessed.

The only atoms of the host substructure that make a significant contribution to the nickel K–edge EXAFS spectrum are the carbon and the nitrogen of the Ni(CN)$_4$ units and the cadmium atoms. The C–N–Cd angle was refined in multiple scattering calculations. Carbon and nitrogen atoms in the host substructure corresponding to Ni...C and Ni...C distances in the range 3.5 Å to 5.0 Å do not contribute significantly to the nickel K–edge EXAFS spectrum. With the exception of 1,2–dibromoethane the halogen atoms contribute significantly to the EXAFS spectrum for all guest molecules studied. The refined Ni...Cl and Ni...Br distances are within physically sensible values, supporting the suggestion that there exists some degree of ordering of the guest molecules relative to the host substructure in these inclusion compounds.

## 3.1 Introduction

Park *et al.* [45] first reported *catena*–[(1,2–diaminopropane)–cadmium(II)–tetra–$\mu$–cyanonickelate(II)] inclusion compounds in 1990 (in the remainder of this chapter the abbreviation Cd(pn)Ni(CN)$_4$ inclusion compounds is used (pn = 1,2–diaminopropane)).

The Cd(pn)Ni(CN)$_4$ inclusion compounds form in the presence of aliphatic guest molecules such as alkanes, halogenoalkanes and alcohols. The starting material for preparation of the host structure is Cd(pn)$_3$Ni(CN)$_4$. Chemically, the Cd(pn)Ni(CN)$_4$ inclusion compounds are related to the Hofmann–pn type inclusion compounds [46, 47] which form, in the presence of aromatic guest molecules, from the same starting material. The structural properties of the two families of inclusion compounds are, however, quite distinct. Whereas the host structure in the Hofmann–pn type inclusion compounds contains cages within which the aromatic guests are enclosed, the Cd(pn)Ni(CN)$_4$ inclusion

compounds contain linear, parallel, infinite tunnels akin, in some respects, to the well known urea and thiourea inclusion compounds [47, 48, 49].

Two types of host structure are known for Cd(pn)Ni(CN)$_4$ inclusion compounds: the first type is monoclinic (space group P2$_1$/a); the second is orthorhombic (space group Pnma). The two structures are very similar (lattice parameters are found within the ranges 13.8 Å $<$ a $<$ 14.2 Å, 26.7 Å $<$ b $<$ 27.2 Å, 7.5 Å $<$ c $<$ 7.7 Å; for the monoclinic structures, $\beta$ is found to be $90 \pm 2°$ [50, 51]), with the tunnels parallel to the crystallographic $c$ axis in both cases. Each structure contains two crystallographically independent Ni(CN)$_4$ units, denoted Ni[1](CN)$_4$ and Ni[2](CN)$_4$, the geometries of which are close to square planar. The Ni[1](CN)$_4$ unit forms part of a doubly–bridged one–dimensional chain, [Ni(CN-Cd-NC)$_2$]$_\infty$, in which the cadmium atoms lie along the $c$ axis and the plane defined by the Ni[1](CN)$_4$ units is almost parallel to the $bc$ plane. These one–dimensional chains are stacked along the $a$ axis to define two of the four "walls" of the tunnel. The Ni[2](CN)$_4$ units are coordinated to cadmium atoms to form extended two–dimensional networks parallel to the $ac$ plane. The one–dimensional chains and two–dimensional networks intersect at each cadmium atom, thereby constructing the three-dimensional host structure. Each cadmium atom is coordinated by six nitrogen atoms (two from Ni[1](CN)$_4$ units, two from Ni[2](CN)$_4$ units, and two from 1,2–diamino-propane ligands).

The main difference between the monoclinic and orthorhombic structures concerns the relative orientations of the 1,2–diaminopropane ligands. In both structures, these ligands protrude into the tunnel; in the monoclinic structure, pairs of 1,2–diaminopropane ligands are related by a centre of symmetry lying on the tunnel axis, whereas in the orthorhombic structure, pairs of 1,2–diaminopropane ligands are related by a mirror plane containing the tunnel axis (see Figure 3.1). It has been reported, that the Cd(pn)Ni(CN)$_4$ inclusion compounds are generally stoichiometric, with a host to guest ratio of 2:1 [51].
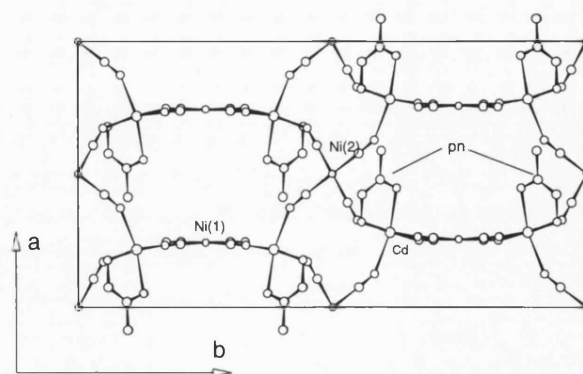
(a) The orthorhombic host substructure
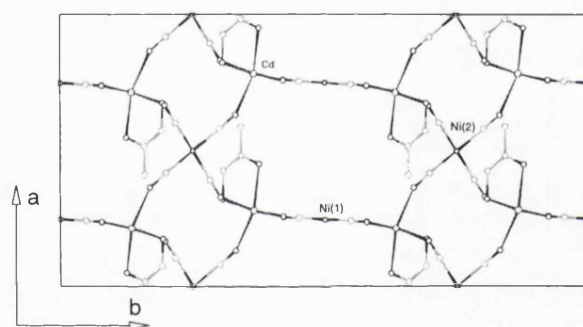


(b) The monoclinic host substructure

Figure 3.1: Comparison of the orthorhombic and monoclinic host structures of the Cd(pn)Ni(CN)$_4$ inclusion compounds, both viewed along the crystallographic c–axis (tunnel axis). Note the different orientations of the 1,2–di-aminopropane ligands (pn) in the two structures.

This suggests that they may be commensurate systems, and therefore that the X–ray diffraction data used to determine the host structure may also contain information on the periodic structural properties of the guest molecules. It was also shown that atoms of the guest molecules can be located from X–ray diffraction data recorded at ambient temperature [51]. On closer inspection however, the reported coordinates for these atoms actually represent guest molecules that are considerably distorted from plausible geometries,

and the reliability and physical interpretation of these atomic positions must therefore be uncertain. It is possible, for example, that these atomic positions merely represent local maxima in the averaged electron density distribution for a significantly disordered guest molecule. This problem is often encountered in attempts to determine the structural properties of guest molecules in commensurate inclusion compounds from X-ray diffraction data [52]. Since the dynamic properties of the guest molecules in Cd(pn)Ni(CN)$_4$ inclusion compounds have not yet been investigated, it is not clear if the source of this disorder is static or dynamic in nature.

In light of the above, Extended X-Ray Absorption Fine Structure spectroscopy (EXAFS), which probes local structural properties about selected atoms, is ideally suited for investigating the nature of host–guest interactions in these materials. In recent years, EXAFS spectroscopy has been employed successfully, to further our knowledge of inclusion compounds in general. The technique has, for example, been employed to investigate the local structural properties of guest molecules in urea inclusion compounds [53] and thiourea inclusion compounds [54]. It has also been used to elucidate the structural properties of guest molecules in layered compounds [55] and zeolites [56], as well as those of layered host structures [57] and zeolites themselves. EXAFS is a particularly useful tool in the study of zeolites, especially for probing the influence of structural properties on their catalytic properties [58, 59, 60, 61].

In this experiment, Cd(pn)Ni(CN)$_4$ inclusion compounds containing a series of halogenated alkanes were investigated. The guest materials employed were 2–chlorobutane, 2–bromobutane, 2,3–dichlorobutane, 2,3–dibromobutane, 1,2–dichloroethane and 1,2–dibromoethane. The pairs of similar materials were chosen in order to contrast possible differences between the chlorinated and brominated guest molecules in the inclusion compound, an addition to any local structural effects the different substituents might have on the host substructure. The Cd(pn)Ni(CN)$_4$ inclusion contain two easily accessible absorp-

tion edges in the host substructure (cadmium and nickel). By choosing bromi-
nated guest molecules, a further absorption edge (namely that of bromine) is
made available which, in addition, allows the local structural properties of the
guest molecules to be probed directly.

Here, the results of variable temperature Ni K–edge EXAFS spectro-
scopic experiments on the above mentioned compounds are reported. Spectra
were recorded at ambient temperature and at temperatures close to 80 K. In
contrast, the X–ray diffraction experiments reported by Iwamoto *et al.* were
performed exclusively at ambient temperature. In the remainder of this chap-
ter Ni K–edge EXAFS experiments performed on Cd(pn)Ni(CN)$_4$ inclusion
compounds will be discussed.

# 3.2 Experimental

## 3.2.1 Preparation of Cd(pn)Ni(CN)$_4$ Inclusion Compounds

The raw host material *tris*-(1,2–diaminopropane)–cadmium–tetracyanonickel-
ate (Cd(pn)$_3$Ni(CN)$_4$, pn = 1,2–diaminopropane) was prepared by crystalli-
sation from a concentrated, aqueous solution of cadmium chloride, potassium
tetracyanonickelate monohydrate and d,l–1,2–diaminopropane in a 1:1:3 mo-
lar ratio. The solids were first dissolved by heating the solution to 100°C.
The appropriate amount of 1,2–diaminopropane was added once the solids
had completely dissolved, the flask was sealed to prevent evaporation of the
1,2–diaminopropane, and the solution was slowly cooled to room temperature.
The raw precipitate was collected by filtration from the mother liquor. The
crystals had a needle morphology and were of a deep brown color.

The raw product was then recrystallised from water, whereupon the color
changed to a pale brown. The morphology was unchanged.

The inclusion compounds were prepared is follows: A saturated solution of Cd(pn)$_3$Ni(CN)$_4$ was prepared under sonification at 50°. The sonification is essential to prevent crystallisation of the starting material remaining in the solution. Once the raw host material was completely dissolved, the pH of the solution was adjusted to between 8 and 9 by dropwise addition of citric acid. Then a molar excess of the guest material was added. The guest molecules considered were 2–chlorobutane, 2–bromobutane, 2,3–dichlorobutane, 2,3–dibromobutane, 1,2–dichloroethane, and 1,2–dibromoethane. Of these, the crystal structure is known for the inclusion compounds containing 2–chlorobutane, 1,2–dichloroethane, and 1,2–dibromoethane [51]. All of the guest materials are liquids that are not completely miscible with the aqueous solution.

The flask was then sealed and left in an incubator at 50°C for several days, until crystals of the inclusion compound had started to grow at the phase boundary between the aqueous and non–aqueous phases. At this point the temperature of the mixture was lowered to 4°C over a period of several days. The product was separated from the mother liquor by filtration, washed with small amounts of cold (*ca.* 4°C) water and stored in a sealed sample container. The shape and size of the crystallites varies from guest material to guest material, but all have a bright yellow colour and a plate morphology. In general the yield is poor ($<$ 10%).

The samples containing 2–chlorobutane, 2,3–dichlorobutane, 1,2–dichloroethane, and 2–bromobutane were characterised by powder X–ray diffraction. In all cases, the powder pattern was characteristic of Cd(pn)Ni(CN)$_4$ inclusion compounds with the orthorhombic host structure. The materials prepared with 2,3–dibromobutane and 1,2–dibromoethane were not characterised by powder X–ray diffraction, as only small amounts of these samples were obtained. However, the external appearance of the crystals (bright yellow colour and flat plate morphology) strongly suggests that these are indeed Cd(pn)Ni(CN)$_4$ inclusion compounds rather than the starting material

$Cd(pn)_3Ni(CN)_4$.

## 3.2.2 EXAFS Spectroscopy

Nickel K–edge X–ray absorption spectra were recorded at station 7.1 at the Synchrotron Radiation Source, Daresbury (2 GeV electron energy, typical electron current in the range 150–210 mA). The Si(111) double–crystal monochromator was detuned to 50% intensity to avoid the effect of higher harmonics in the photon beam.

Most of the samples were ground to fine powders and pressed into thin pellets of approximately 20 mm diameter. These were then loaded into a standard sample holder. Samples for which only small amounts were available were spread thinly onto adhesive tape and several layers of tape were combined for a single sample. The samples were placed in a liquid nitrogen cryostat in order to perform low temperature measurements.

For each sample two spectra were recorded, one at ambient temperature (*ca.* 295 K) and one at low temperature (*ca.* 120 K). At each temperature, two spectra were recorded and subsequently added to improve the signal to noise ratio.

## 3.3 Results and Discussion

Initially, this section focusses on the 2–chlorobutane/Cd(pn)Ni(CN)₄ inclusion compound and the stategy of analysis developed is discussed in detail. A similar strategy is employed for all inclusion compounds studied and the results obtained for the different inclusion compounds are then compared in Section 3.3.2.

## 3.3.1 2–Chlorobutane/Cd(pn)Ni(CN)$_4$

Experimental nickel K–edge EXAFS spectra from the 2–chlorobutane/ Cd(pn)Ni(CN)$_4$ inclusion compound at 116 K and 295 K and the respective Fourier transformations are shown in Figure 3.2. The backscattering is clearly dominated by the first two shells, which represent the carbon and nitrogen atoms of the Ni(CN)$_4$ unit. These give rise to the peaks at approximately 1.4 Å and 2.5 Å in the Fourier transformations. The fact that the heights of these peaks are approximately equal suggests that the effects of multiple scattering are significant (resulting from the linearity of the Ni–C–N unit). The third most significant peak (at ca. 4.8 Å) in the Fourier transformation arises from the cadmium atoms of the host structure.

The initial structural model used (Model 1) considered only the carbon and nitrogen atoms from the Ni(CN)$_4$ units, as well as the cadmium atoms from the host structure and took multiple scattering into account. Further models were developed, extending the initial structural model to include further atoms from the host substructure (Model 2) and atoms from the guest substructure (Model 3).

Prior to the following discussion, it should be noted, that of the materials studied the crystal structures are only known for the the three compounds containing the guest molecules 2–chlorobutane, 1,2–dichloroethane, and 1,2–dibromoethane, respectively.

**Model 1**: Initially only the carbon and the nitrogen atoms of the Ni(CN)$_4$ units were considered. Since there are two crystallographically independent nickel sites, each with two different Ni$\cdots$C distances and two different Ni$\cdots$N distances, it was important to establish the extent to which these differences, albeit subtle, could be be observed in the experimental data. For this purpose, two different models were compared:

**a)** a model based on the actual geometry of the Ni[1] site [1] in the published crystal structure [51] for which there are two different Ni$\cdots$C distances corresponding to $r_C = 1.86$ Å [occupancy $N_C = 2$] and $r_C = 1.88$ Å [$N_C = 2$] and two different Ni$\cdots$N distances corresponding to $r_N = 3.01$ Å [$N_N = 2$] and $r_N = 3.02$ Å [$N_N = 2$] and,

**b)** an idealised model representing single, averaged shells of carbon initially at $r_C = 1.86$ Å [$N_C = 4$] and nitrogen initially at $r_N = 3.00$ Å [$N_N = 4$].



(a) 116 K               (b) 295 K

(c) 116 K               (d) 295 K
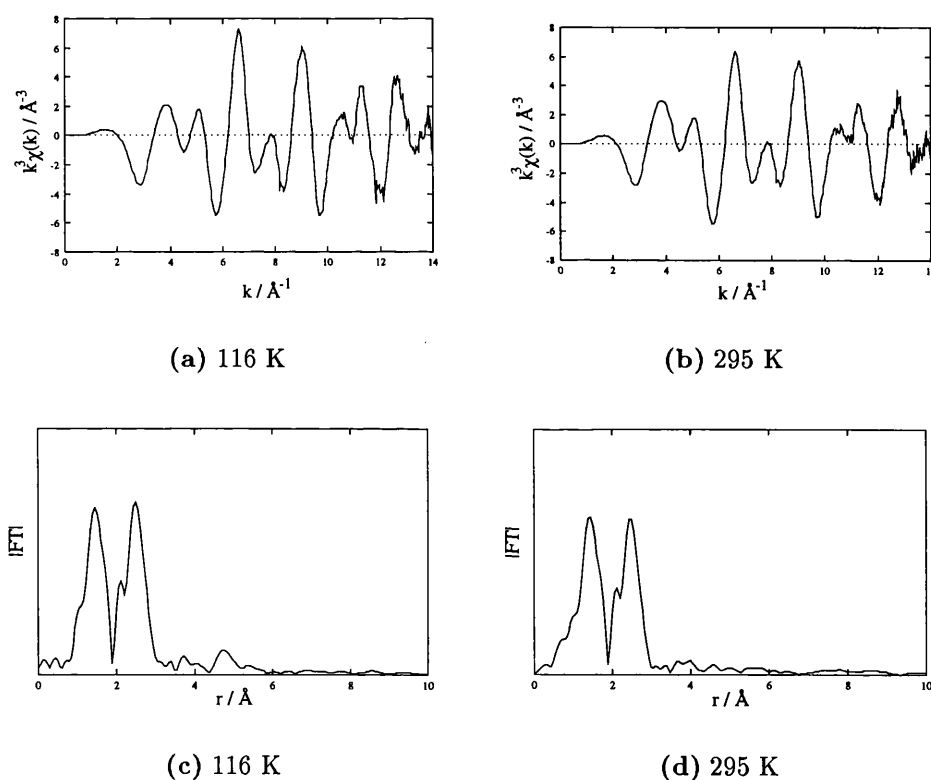
**Figure 3.2:** EXAFS spectra (above) and their Fourier transformations (below) for the 2–chlorobutane/Cd(pn)Ni(CN)$_4$ inclusion compound at 116 K (a and c) and 295 K (b and d). It should be noted, that these spectra are not phase shift corrected.

---

[1] Although the geometry around the Ni[2] site differs from that of the Ni[1] site, these differences are not relevant in the context of this experiment (see text).

**Table 3.1:** Comparison of the results from Model 1 a) and b). The initial distances in the case of a) were $r_1 = 1.86$ Å, $r_2 = 3.01$ Å, $r_3 = 1.88$ Å and $r_4 = 3.02$ Å. In Model 1 a), the first CN unit was placed along the x–axis of the coordinate system, the second was placed along the y–axis, in order to account for multiple scattering effects from the two units separately and the Debye–Waller factor was constrained to be the same for the carbon atoms and for the nitrogen atoms, respectively.

Refined positions from Model 1 a)

| | | | | | |
|---|---|---|---|---|---|
| $r_1$ | = | 1.866 Å | $2\sigma_1^2$ | = | 0.00217 Å$^2$ |
| $r_2$ | = | 3.033 Å | $2\sigma_2^2$ | = | 0.00416 Å$^2$ |
| $r_3$ | = | 1.865 Å | | | |
| $r_4$ | = | 3.034 Å | | | |
| | | | $\chi^2$ | = | 5.80 |
| | | | R | = | 26.29 |

Refined Debye–Waller factors from Model
1 a) with fixed starting positions

| | | | | | |
|---|---|---|---|---|---|
| $2\sigma_1^2$ | = | 0.00219 Å$^2$ | $\chi^2$ | = | 8.17 |
| $2\sigma_2^2$ | = | 0.00416 Å$^2$ | R | = | 31.20 |

Refined Debye–Waller factors from Model
1 b) with fixed starting positions

| | | | | | |
|---|---|---|---|---|---|
| $2\sigma_1^2$ | = | 0.00209 Å$^2$ | $\chi^2$ | = | 5.91 |
| $2\sigma_2^2$ | = | 0.00378 Å$^2$ | R | = | 26.53 |

There was no significant difference in the fit obtained for a) and b) (see Table 3.1), and the idealised representation (Model b) of the geometry of the Ni(CN)$_4$ units was used in all subsequent refinements as this reduced the number of refined parameters.

Next, cadmium was added to the structural model as a single, averaged shell initially at $r_{Cd} = 5.2$ Å $[N_{Cd} = 4]$. In the published crystal structure [51], each nickel site has two pairs of crystallographically equivalent cadmium neighbours at distances of 5.24 Å and 5.34 Å for Ni[1] and 5.16 Å and 5.23 Å for Ni[2]. To assess the effect of the initial position of the cadmium atoms on the result of the refinement, the first two shells were refined with cadmium held at various different positions corresponding to different angles $\theta$(C–N–Cd). The distance between cadmium and nitrogen was kept constant for these

calculations, and therefore the nickel–cadmium distances were different in the different initial structures. The C–N–Cd angle affects the effective scattering path and hence affects the observed amplitude. The initial conditions for the cadmium shell are given in Table 3.2 and the definition of the geometric parameters is shown in Figure 3.3.

In Table 3.3 the results of these refinement calculations are presented. A clear minimum in the value of $\chi^2$ is observed for a cadmium angle of 145°. Subsequent refinements of the cadmium position (and hence of the angle $\theta$(C–N–Cd)) from different initial positions revealed, that the refined position of cadmium atom was essentially independent of the initial position.
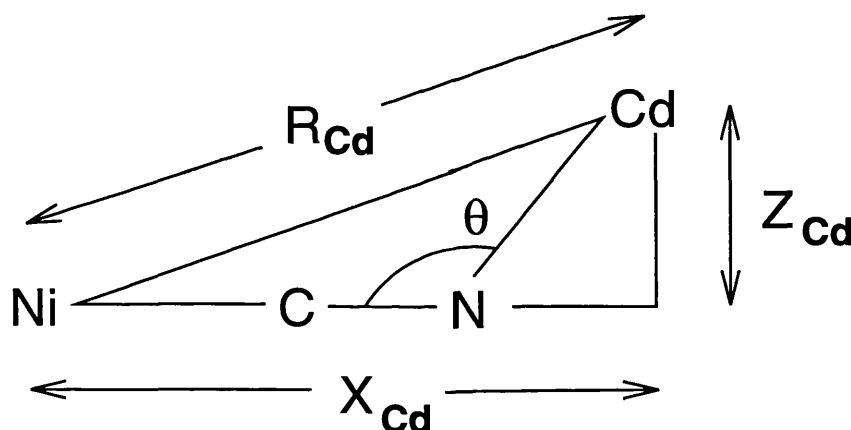


**Figure 3.3:** Definition of the parameters shown in Table 3.2.

The refined position of the cadmium atom corresponded to $r_{Cd} = 5.13$ Å, $\theta$(C–N–Cd) = 144° at 116 K, and $r_{Cd} = 5.07$ Å, $\theta$(C–N–Cd) = 141° at 295 K. The corresponding angles in the published crystal structure [51] are 171° and 172° for Ni[1] and 146° and 152° for Ni[2] (Table 3.7). As the published crystal structure contains a pair of $\theta$(C–N–Cd) angles close to 150° and a pair of $\theta$(C–N–Cd) angles close to 171°, a model representing two independent C–N–Cd units was also considered.

**Table 3.2:** Geometric parameters for the cadmium shell in the refinement calculations assessing the effect of the angle $\theta$(C–N–Cd).

| $\theta/^\circ$ | $R_{Cd}$ / Å | $Z_{Cd}$ / Å | $X_{Cd}$/Å | $\theta/^\circ$ | $R_{Cd}$/Å | $Z_{Cd}$/Å | $X_{Cd}$/Å |
|---|---|---|---|---|---|---|---|
| 135 | 4.968 | 1.661 | 4.682 | 160 | 5.290 | 0.802 | 5.229 |
| 140 | 5.051 | 1.511 | 4.820 | 165 | 5.325 | 0.607 | 5.290 |
| 145 | 5.125 | 1.349 | 4.944 | 170 | 5.350 | 0.405 | 5.335 |
| 150 | 5.190 | 1.175 | 5.055 | 175 | 5.365 | 0.204 | 5.361 |
| 155 | 5.245 | 0.992 | 5.150 | 180 | 5.370 | 0 | 5.37 |

The occupancies of the atoms in these C–N–Cd units were fixed at $N_C = N_N = N_{Cd} = 2$, the initial values of $r_C$, $r_N$ and $r_{Cd}$ were taken as the refined values for the above model representing a single, averaged C–N–Cd unit, and the initial values of $\theta$(C–N–Cd) for the two C–N–Cd units were 150° and 171° respectively. The number of refined parameters is approximately twice that for the model with only a single, averaged C–N–Cd unit. Although the refinements in this model generated physically sensible parameters, with the refined values of $\theta$(C–N–Cd) lying acceptably close to the initial values taken from the published crystal structure, this modified model gave a fit which was significantly worse than the model representing a single, averaged C–N–Cd unit. For this reason, the latter model containing two independent C–N–Cd units was not considered further, even though this model should provide a more complete representation of the actual structure.

**Table 3.3:** Results of the refinement calculations with various fixed cadmium positions. A clear minimum in terms of the goodness–of–fit parameter is observed for a $\theta$(C–N–Cd) angle of 145°. The variation of the parameters for the carbon and nitrogen shell is within standard error limits. Estimated errors in the refined parameters are $\pm 0.02$ Å for $r$, 10% for $2\sigma^2$. The shell occupancy N is treated as a fixed parameter in these refinement calculations and is set to a value of N = 4.

| $\theta$ | = | 135° | $r_1$ | = | 1.86 | $2\sigma_1^2$ | = | 0.0022 | $\chi^2$ | = | 4.67 |
| | | | $r_2$ | = | 3.02 | $2\sigma_2^2$ | = | 0.0042 | $R$ | = | 23.63 |
| $\theta$ | = | 140° | $r_1$ | = | 1.86 | $2\sigma_1^2$ | = | 0.0021 | $\chi^2$ | = | 3.82 |
| | | | $r_2$ | = | 3.02 | $2\sigma_2^2$ | = | 0.0042 | $R$ | = | 21.36 |
| $\theta$ | = | 145° | $r_1$ | = | 1.86 | $2\sigma_1^2$ | = | 0.0022 | $\chi^2$ | = | 2.99 |
| | | | $r_2$ | = | 3.02 | $2\sigma_2^2$ | = | 0.0042 | $R$ | = | 18.91 |
| $\theta$ | = | 150° | $r_1$ | = | 1.86 | $2\sigma_1^2$ | = | 0.0022 | $\chi^2$ | = | 3.27 |
| | | | $r_2$ | = | 3.02 | $2\sigma_2^2$ | = | 0.0042 | $R$ | = | 19.77 |
| $\theta$ | = | 155° | $r_1$ | = | 1.86 | $2\sigma_1^2$ | = | 0.0022 | $\chi^2$ | = | 3.48 |
| | | | $r_2$ | = | 3.02 | $2\sigma_2^2$ | = | 0.0042 | $R$ | = | 20.37 |
| $\theta$ | = | 160° | $r_1$ | = | 1.86 | $2\sigma_1^2$ | = | 0.0022 | $\chi^2$ | = | 5.46 |
| | | | $r_2$ | = | 3.02 | $2\sigma_2^2$ | = | 0.0042 | $R$ | = | 25.55 |
| $\theta$ | = | 165° | $r_1$ | = | 1.86 | $2\sigma_1^2$ | = | 0.0022 | $\chi^2$ | = | 11.84 |
| | | | $r_2$ | = | 3.02 | $2\sigma_2^2$ | = | 0.0042 | $R$ | = | 37.58 |
| $\theta$ | = | 170° | $r_1$ | = | 1.86 | $2\sigma_1^2$ | = | 0.0022 | $\chi^2$ | = | 21.83 |
| | | | $r_2$ | = | 3.03 | $2\sigma_2^2$ | = | 0.0042 | $R$ | = | 51.01 |
| $\theta$ | = | 175° | $r_1$ | = | 1.86 | $2\sigma_1^2$ | = | 0.0022 | $\chi^2$ | = | 30.76 |
| | | | $r_2$ | = | 3.03 | $2\sigma_2^2$ | = | 0.0042 | $R$ | = | 60.55 |
| $\theta$ | = | 180° | $r_1$ | = | 1.86 | $2\sigma_1^2$ | = | 0.0022 | $\chi^2$ | = | 34.41 |
| | | | $r_2$ | = | 3.03 | $2\sigma_2^2$ | = | 0.0042 | $R$ | = | 64.04 |

The Ni–C–N angle ($\phi$) varies within the range of 178° — 182° in the various reported crystal structures [50, 51]. In all the refinement calculations discussed above, as well as in those to be discussed in the remainder of this section, a value of $\phi = 180°$ was used. This approach was justified, since no significant difference was observed (see Table 3.4) between the refined parameter obtained using $\phi = 178°$, $\phi = 180°$, and $\phi = 182°$ [2].

The results from fitting Model 1 to the EXAFS data for all compounds studied are summarised in Table 3.5 and the fits to the data for 2–chloro-butane/Cd(pn)Ni(CN)$_4$ are shown in Figure 3.4.

**Table 3.4:** Comparison of the refined Debye–Waller factors $2\sigma^2$, occupancies N, and Goodness–of–fit parameters obtained for different angles $\phi$(Ni–C–N) at T = 116 K. Note that N was restrained to be the same for all three shells.

| $\phi$(Ni–C–N) | $2\sigma^2$(C) / Å$^2$ | $2\sigma^2$(N) / Å$^2$ | $2\sigma^2$(Cd) / Å$^2$ | N | $\chi^2$ |
|---|---|---|---|---|---|
| 178° | 0.00216 | 0.00393 | 0.00932 | 3.018 | 2.935 |
| 180° | 0.00214 | 0.00418 | 0.0091 | 3.021 | 2.887 |
| 182° | 0.00216 | 0.00329 | 0.0093 | 3.019 | 3.079 |

[2]It should be noted, that in the planar models considered, $\phi > 180°$ implies that the Ni–C–N–Cd dihedral angle is 180°, whereas $\phi < 180°$ implies that the Ni–C–N–Cd dihedral angle is 0°.

(a) 116 K          (b) 295 K

(c) 116 K          (d) 295 K
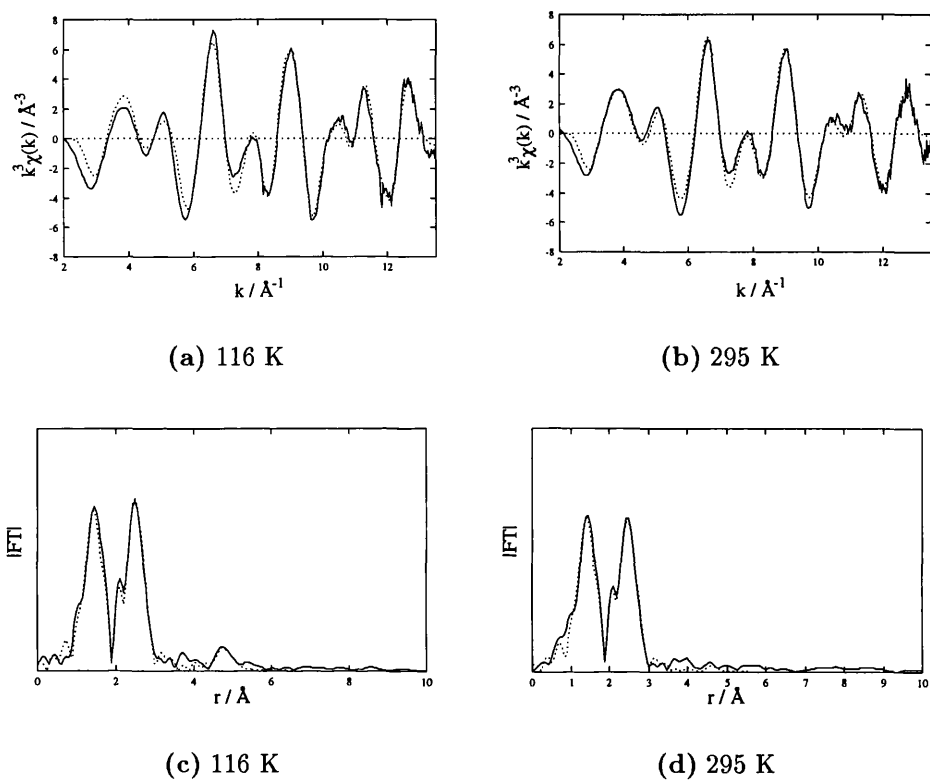
**Figure 3.4:** Comparison of the spectra calculated using Model I and their Fourier transformations to the experimental data for 2-chlorobutane. The full lines are the experimental data, the dotted lines are the calculated data.

**Table 3.5:** Results of the refinement calculations for Model 1 from the nickel K–edge EXAFS data from all the Cd(pn)Ni(CN)$_4$ inclusion compounds studied. Estimated errors in the refined parameters are $\pm 0.02$ Å for $r$, 10% for $2\sigma^2$, and 20% for N.

| Guest | T/K | $\chi^2$ | R | shell | r/Å | $2\sigma^2/\text{Å}^2$ | N | $\theta$/degrees |
|---|---|---|---|---|---|---|---|---|
| 2–chloro– | 116 | 2.80 | 18.30 | C | 1.86 | 0.0038 | 4.0 | — |
| butane | | | | N | 3.02 | 0.0083 | 4.0 | — |
| | | | | Cd | 5.14 | 0.014 | 4.0 | 145 |
| | 295 | 2.19 | 17.51 | C | 1.85 | 0.0052 | 4.3 | — |
| | | | | N | 3.01 | 0.011 | 4.3 | — |
| | | | | Cd | 5.11 | 0.031 | 4.3 | 143 |
| 2,3–dichloro– | 120 | 4.98 | 21.72 | C | 1.86 | 0.0031 | 4.1 | — |
| butane | | | | N | 3.02 | 0.0075 | 4.1 | — |
| | | | | Cd | 5.28 | 0.0077 | 4.1 | 155 |
| | 295 | 3.57 | 20.78 | C | 1.85 | 0.0050 | 4.5 | — |
| | | | | N | 3.02 | 0.010 | 4.5 | — |
| | | | | Cd | 5.12 | 0.020 | 4.5 | 154 |
| 1,2–dichloro– | 135 | 4.46 | 20.33 | C | 1.85 | 0.0046 | 4.4 | — |
| ethane | | | | N | 3.02 | 0.0083 | 4.4 | — |
| | | | | Cd | 5.12 | 0.0050 | 4.4 | 142 |
| | 295 | 3.33 | 20.63 | C | 1.85 | 0.0049 | 4.3 | — |
| | | | | N | 3.01 | 0.0099 | 4.3 | — |
| | | | | Cd | 5.22 | 0.019 | 4.3 | 152 |
| 2–bromo– | 125 | 7.19 | 26.63 | C | 1.86 | 0.0035 | 4.0 | — |
| butane | | | | N | 3.02 | 0.0074 | 4.0 | — |
| | | | | Cd | 5.27 | 0.0093 | 4.0 | 154 |
| | 295 | 3.58 | 22.37 | C | 1.86 | 0.0051 | 4.2 | — |
| | | | | N | 3.02 | 0.010 | 4.2 | — |
| | | | | Cd | 5.14 | 0.016 | 4.2 | 145 |
| 2,3–dibromo– | 125 | 5.35 | 21.96 | C | 1.85 | 0.0038 | 3.9 | — |
| butane | | | | N | 3.02 | 0.0072 | 3.9 | — |
| | | | | Cd | 5.26 | 0.0039 | 3.9 | 156 |
| | 295 | 3.32 | 20.70 | C | 1.85 | 0.0057 | 4.1 | — |
| | | | | N | 3.02 | 0.010 | 4.1 | — |
| | | | | Cd | 5.24 | 0.012 | 4.1 | 146 |
| 1,2–bromo– | 137 | 6.51 | 27.27 | C | 1.85 | 0.0069 | 4.1 | — |
| ethane | | | | N | 3.02 | 0.0078 | 4.1 | — |
| | | | | Cd | 5.26 | 0.0055 | 4.1 | 154 |
| | 295 | 2.95 | 20.48 | C | 1.86 | 0.0053 | 4.1 | — |
| | | | | N | 3.02 | 0.0099 | 4.1 | — |
| | | | | Cd | 5.24 | 0.024 | 4.1 | 154 |

**Model 2**: This model extends Model 1 by including further carbon and nitrogen atoms from the host structure. The reported host structure [51] contains several carbon and nitrogen atoms corresponding to $Ni \cdots C$ and $Ni \cdots N$ distances in the range 3.3 Å – 5.1 Å. In Model 2, these carbon and nitrogen atoms were divided into three groups, with the $Ni \cdots C$ or $Ni \cdots N$ distances within each group differing by less than ca. 0.3 Å. The distances within each group were then averaged to give shells at $r_{C2} = 3.5$ Å, $r_{C3} = 4.3$ Å, $r_{C4} = 4.9$ Å, with occupancies $N_{C2} = 1$, $N_{C3} = 3$, $N_{C4} = 4$. As carbon and nitrogen have similar backscattering behaviour, these averaged shells were treated as carbon atoms. Initially, the following models were considered:

**a)** the atoms of model 1 plus C2

**b)** the atoms of model 1 plus C3

**c)** the atoms of model 1 plus C4.

However, the fits obtained with these models did not represent statistically significant improvements in fit in comparison with Model 1.

Next, each shell was added successively (first considering the atoms of Model 1 plus C2 and C3, and second considering the atoms of Model 1 plus C2, C3 and C4). Again no statistically significant improvements in fit were obtained by inclusion of these shells within the model. The lack of a significant contribution of shells C2, C3 and C4 to the EXAFS spectrum reflects the comparatively large $Ni \cdots C$ and $Ni \cdots N$ distances, the low scattering factors of the carbon and nitrogen atoms, and the fact that there are many atoms distributed within this range of distances; as a consequence, the presence of these shells will result in only a weak contribution to the EXAFS spectrum. For this reason, the only atoms of the host structure considered in the subsequent data analysis were those used in Model 1.

**Model 3**    The aim of this model was to determine whether well-defined positions of guest atoms relative to the host structure can be identified. Although some use is made of information from the reported crystal structures [50, 51] concerning the distances of the carbon atoms in the first shell, the distances of the nitrogen atoms in the second shell and the number of atoms contributing to any given shell, the approach taken is essentially independent of any information regarding the positions of guest atoms available from the X–ray diffraction studies [51]. In the first instance, Model 3 considered the atoms of Model 1 plus a single, additional chlorine shell, represented by an average of the Ni[1]$\cdots$Cl and Ni[2]$\cdots$Cl distances. The occupancy of this chlorine shell was initially assumed to be 1.5, since plausible structures with one chlorine atom in the vicinity of one nickel site and two chlorine atoms in the vicinity of the other nickel site can be envisaged. $N_{Cl} = 1.5$ represents the average occupancy. Errors in this representation of the average chlorine occupancy may be accommodated in the refined Debye–Waller factor for the chlorine shell.

Several different initial Ni$\cdots$Cl distances from $r_{Cl} = 4.2$ Å to 5.4 Å in steps of 0.1 Å were considered. In the final stages of each refinement, both $N_{Cl}$ and $2\sigma^2(\mathrm{Cl})$ were allowed to refine, leading to a significant increase in $N_{Cl}$ compared to the initial value. For the data recorded at 116 K, the best fit was found for the refined value $r_{Cl} = 4.60$ Å. The second best fit corresponded to the refined value $r_{Cl} = 5.40$ Å, which also represents a statistically significant improvement of fit with respect to Model 1. Based on this finding, a model containing two chlorine shells, initially at $r_{Cl1} = 4.60$ Å and $r_{Cl2} = 5.40$ Å, was considered; the Debye–Waller factors for the chlorine shells were fixed (at the values obtained for the single chlorine shell), and the occupancies of the chlorine shells were refined. These chlorine shells refined to $r_{Cl1} = 4.62$ Å [$N_{Cl1} = 1.45$] and $r_{Cl2} = 5.46$ Å [$N_{Cl2} = 0.68$]; however, the improved fit obtained for this model was not statistically significant in comparison with the

models containing a single chlorine shell. Similar results were obtained for the data recorded at 295 K. For Model 3 with a single chlorine shell, the best fit corresponded to $r_{Cl} = 4.58$ Å, and the second best fit corresponded to $r_{Cl} = 5.07$ Å. Again, the improvement in fit upon consideration of two independent chlorine shells is not statistically significant. For comparison, the positions of chlorine atoms assigned from the X–ray diffraction data [51] for 2–chloro-butane/Cd(pn)Ni(CN)$_4$ correspond to Ni[1]$\cdots$Cl distances $r_{Cl} = 4.11$ Å [$N_{Cl}$ = 2] and $r_{Cl} = 4.92$ Å [$N_{Cl} = 2$], and Ni[2]$\cdots$Cl distance $r_{Cl} = 4.99$ Å [$N_{Cl} =$ 1]. The refined parameters for the carbon and nitrogen shells in Model 3 are virtually identical to those obtained for the same shells in Model 1 (see Tables 3.5 and 3.6). This also holds for most parameters relating to the cadmium shell. Comparing the parameters refined from the data recorded at 116 K and at 295 K, there are no significant differences in the refined distances ($\Delta r \leq$ 0.02 Å). As expected, the Debye-Waller factors are systematically higher at the higher temperature. No attempt was made to incorporate carbon atoms of the guest molecule into the models. The crystallographic data show that the Ni$\cdots$C distances for carbon atoms of the guest are in the ranges explored in Model 2, for which it was shown that these atoms do not represent statistically significant shells in the EXAFS data. Therefore, it was not considered justifiable to include carbon atoms of the guest molecule in the structural model.

Results from fitting Model 3 to the EXAFS data for all compounds studied are reported in Table 3.6. Fits of Model 3 to the EXAFS spectra recorded for 2–chlorobutane/Cd(pn)Ni(CN)$_4$ at 116 K and 295 K are shown in Figure 3.5

(a) 116 K             (b) 295 K

(c) 116 K             (d) 295 K
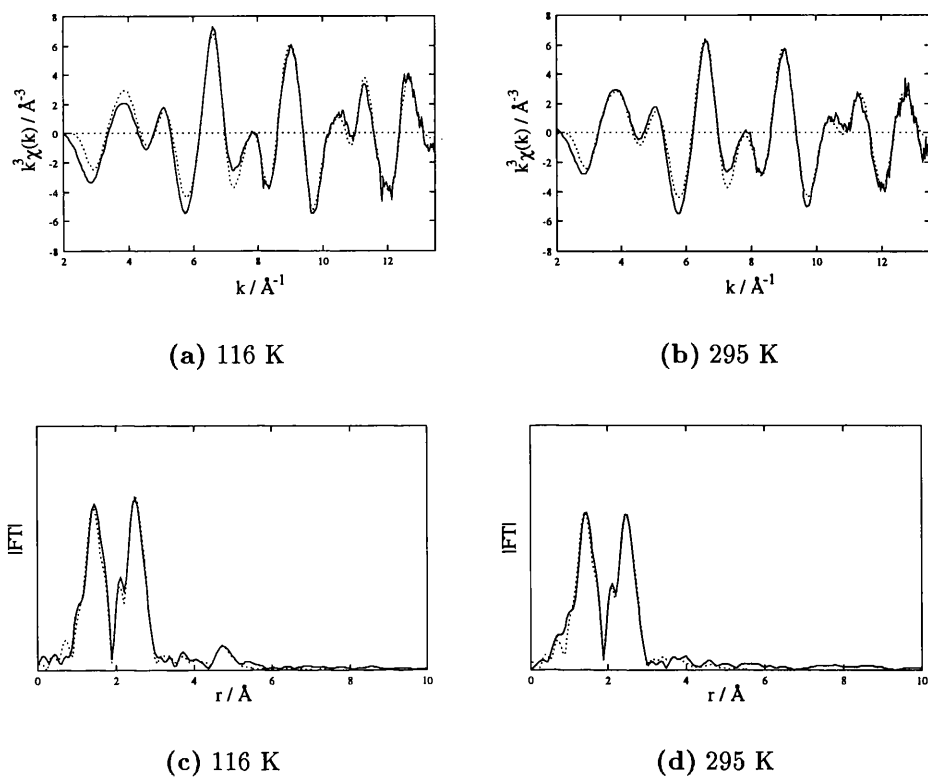
**Figure 3.5:** Comparison of the experimental data for 2–chlorobutane with the calculated spectra and Fourier transformations for Model 3. The full lines are the experimental data, the dotted lines are the calculated data.

**Table 3.6:** Results of the refinement calculations assuming Model 3 for the nickel K–edge EXAFS data for all compounds studied. (F) denotes parameters that were not refined. Estimated errors in the refined parameters are $\pm 0.02$ Å for $r$, 10% for $2\sigma^2$, and 20% for N. $\xi$ is defined as $[d - 1 - p][\chi^2(M1) - \chi^2(M3)]/[3\chi^2(M3)]$, where $\chi^2(M1)$ denotes the value of $\chi^2$ obtained for Model 1, $\chi^2(M3)$ denotes the value of $\chi^2$ obtained for Model 3, d is the number of data points and p is the number of refined parameters in Model 3. $\xi$ is used in assessing the statistical significance of the halogen shell in Model 3. Specifically, when d $\approx$ 200, the halogen shell is significant at the 5% confidence level if $\xi \gtrsim 2.7$.

2–chlorobutane

| T/K | $\chi^2$ | R | $\xi$ | shell | r / Å | $2\sigma^2$ / Å$^2$ | N | $\theta$ / degrees |
|---|---|---|---|---|---|---|---|---|
| 116 | 2.64 | 17.76 | 3.82 | C | 1.86 | 0.0039 | 4.0 | |
| | | | | N | 3.02 | 0.0083 | 4.0 | |
| | | | | Cd | 5.12 | 0.015 | 4.0 | 139 |
| | | | | Cl | 4.60 | 0.021 | 2.7 | |
| 295 | 1.93 | 16.45 | 8.49 | C | 1.85 | 0.0052 | 4.3 | |
| | | | | N | 3.01 | 0.011 | 4.3 | |
| | | | | Cd | 5.10 | 0.028 | 4.3 | 137 |
| | | | | Cl | 4.58 | 0.028 | 3.3 | |

2,3–dichlorobutane

| T / K | $\chi^2$ | R | $\xi$ | shell | r / Å | $2\sigma^2$ / Å$^2$ | N | $\theta$ / degrees |
|---|---|---|---|---|---|---|---|---|
| 120 | 4.41 | 20.44 | 8.14 | C | 1.86 | 0.0031 | 4.0 | |
| | | | | N | 3.02 | 0.0074 | 4.0 | |
| | | | | Cd | 5.28 | 0.0072 | 4.0 | 154 |
| | | | | Cl | 4.57 | 0.019 | 3.2 | |
| 295 | 3.24 | 19.97 | 6.41 | C | 1.85 | 0.0050 | 4.6 | |
| | | | | N | 3.00 | 0.010 | 4.6 | |
| | | | | Cd | 5.23 | 0.018 | 4.6 | 153 |
| | | | | Cl | 4.54 | 0.028 | 3.9 | |

| continued from previous page |
|---|

**1,2–dichloroethane**

| T / K | $\chi^2$ | R | $\xi$ | shell | r / Å | $2\sigma^2$ / Å$^2$ | N | $\theta$ / degrees |
|---|---|---|---|---|---|---|---|---|
| 135 | 4.22 | 19.78 | 3.58 | C | 1.86 | 0.0046 | 4.4 | |
| | | | | N | 3.02 | 0.0083 | 4.4 | |
| | | | | Cd | 5.12 | 0.0052 | 4.4 | 142 |
| | | | | Cl | 4.59 | 0.030 | 3.7 | |
| 295 | 3.07 | 19.81 | 5.34 | C | 1.85 | 0.0049 | 4.3 | |
| | | | | N | 3.01 | 0.0099 | 4.3 | |
| | | | | Cd | 5.23 | 0.017 | 4.3 | 153 |
| | | | | Cl | 4.56 | 0.023 | 3.0(F) | |

**2–bromobutane**

| T / K | $\chi^2$ | R | $\xi$ | shell | r / Å | $2\sigma^2$ / Å$^2$ | N | $\theta$ / degrees |
|---|---|---|---|---|---|---|---|---|
| 125 | 5.99 | 24.30 | 12.62 | C | 1.86 | 0.0038 | 4.1 | |
| | | | | N | 3.02 | 0.0076 | 4.1 | |
| | | | | Cd | 5.27 | 0.057 | 4.1 | 154 |
| | | | | Br | 4.78 | 0.0075 | 1.5(F) | |
| 295 | 3.42 | 22.37 | 2.95 | C | 1.86 | 0.0051 | 4.2 | |
| | | | | N | 3.02 | 0.010 | 4.2 | |
| | | | | Cd | 5.13 | 0.015 | 4.2 | 143 |
| | | | | Br | 4.78 | 0.024 | 1.5(F) | |

**2,3–dibromobutane**

| T / K | $\chi^2$ | R | $\xi$ | shell | r / Å | $2\sigma^2$ / Å$^2$ | N | $\theta$ / degrees |
|---|---|---|---|---|---|---|---|---|
| 125 | 4.94 | 21.10 | 5.23 | C | 1.85 | 0.0038 | 3.9 | |
| | | | | N | 3.01 | 0.0072 | 3.9 | |
| | | | | Cd | 5.28 | 0.0030 | 3.9 | 156 |
| | | | | Br | 4.77 | 0.020 | 3.0(F) | |
| 295 | 3.17 | 19.99 | 2.98 | C | 1.85 | 0.0057 | 4.2 | |
| | | | | N | 3.01 | 0.010 | 4.2 | |
| | | | | Cd | 5.12 | 0.013 | 4.2 | 143 |
| | | | | Br | 4.78 | 0.042 | 3.4 | |

1,2–dibromoethane

| T / K | $\chi^2$ | R | $\xi$ | shell | r / Å | $2\sigma^2$ / Å$^2$ | N | $\theta$ / degrees |
|---|---|---|---|---|---|---|---|---|
| 137 | 6.30 | 26.89 | 2.10 | C | 1.85 | 0.0070 | 4.1 | |
| | | | | N | 3.02 | 0.0079 | 4.1 | |
| | | | | Cd | 5.26 | 0.0080 | 4.1 | 155 |
| | | | | Br | 4.73 | 0.014 | 3.0(F) | |
| 295 | 2.89 | 20.26 | 1.31 | C | 1.86 | 0.0053 | 4.1 | |
| | | | top | N | 3.02 | 0.0099 | 4.1 | |
| | | | | Cd | 5.24 | 0.021 | 4.1 | 154 |
| | | | | Br | 4.77 | 0.038 | 3.0(F) | |

## 3.3.2 Comparison of the Different Inclusion Compounds

The refined parameters for the different inclusion compounds are fairly similar
in all cases. Significant differences are, however, observed for the parameters
relating to the cadmium atoms, both for different guest molecules and (in some
cases) for the same material at different temperatures. At a given temperature
and for a given compound, the refined angle $\theta$(C–N–Cd) is similar (within 6°)
for both Model 1 and Model 3. Comparing different Cd(pn)Ni(CN)₄ inclusion
compounds, however, there appears to be a well defined correlation between the
refined $\theta$(C–N–Cd) angle and the Ni⋯Cd distance, a larger angle correspond-
ing to a larger distance. It is difficult to assess whether the observed variations
of the parameters for the cadmium shell reflect genuine structural differences
between the different inclusion compounds or whether they are merely due
to the simplicity of the models considered or even a consequence of the high
degree of correlation between various refined parameters. However, for the 2–
chlorobutane/Cd(pn)Ni(CN)₄ inclusion compound, it was shown, that a model
comprising two independent C–N–Cd units gave a significantly worse fit than

the single, averaged unit.

If the observed differences in $r_{Cd}$ and $\theta$(C–N–Cd) do reflect genuine structural variations between the different inclusion compounds, they may be due to distortions of the host structure caused by the presence of the guest molecules. However, for the three inclusion compounds studied for which the structures have been reported in [51], no significant structural differences concerning the cadmium shell are discernible (see Table 3.7).

Table 3.7: The values of $\theta$(C–N–Cd) determined using X–ray diffraction data.

| Guest | Ni[1] | | Ni[2] | |
|---|---|---|---|---|
| 2–chlorobutane | 171° | 172° | 146° | 152° |
| 1,2–dichloroethane | 169° | 175° | 144° | 146° |
| 1,2–dibromoethane | 169° | 176° | 144° | 145° |

From the EXAFS results, the refined angle $\theta$(C–N–Cd) is significantly different at different temperatures only for the compounds containing 2–bromobutane, 2,3–dibromobutane, and 1,2-dichloroethane. In all three cases there is also a significant difference of 0.10 Å — 0.14 Å between the refined distance $r_{Cd}$ at low temperature and at ambient temperature. It is conceivable that some of these compounds may undergo structural phase transitions involving a distortion of the host structure when cooled below ambient temperature, yet the variation of refined parameters observed between the low temperature and ambient temperature spectra do not represent conclusive evidence of the occurrence of such transitions. Further independent evidence from low temperature, diffraction based techniques or from measurements of thermodynamic properties may shed some light on this issue.

Major differences in $2\sigma^2$ are observed for the low temperature data for the compounds containing the guest molecules 2–bromobutane and 1,2–dibromoethane, when comparing Models 1 and 3. This indicates that the refined value

for $2\sigma^2$ is compensating for inadequacies in the model and/or for a large degree of correlation between refined parameters, rather than conveying physically meaningful information.

Next the halogen atoms of the guest molecules are discussed. The refined Ni$\cdots$Br distances tend to be longer than the refined Ni$\cdots$Cl distances, as might be expected. There is no evidence of a systematic change (either increase or decrease) of these distances when comparing the results at ambient temperature with those at low temperature. A high degree of correlation between the Debye–Waller factor of the guest atoms and their occupancies must be expected. These parameters were handled in the following way during the refinements. In the first instance, the occupancy of the halogen shell was fixed at $N_X = 1.5$ for the monohalogeno guest molecules (*vide supra*) and at $N_X = 3$ for the dihalogeno guest molecules and the Debye–Waller factor was refined. In the final stage of the refinement, both occupancy, $N_X$, and Debye–Waller factor, $2\sigma_X^2$, were allowed to refine. For some inclusion compounds this strategy led to well behaved refinements resulting in physically reasonable refined values of $2\sigma^2$. For the inclusion compounds containing 1,2–dichloroethane (at ambient temperature), 2–bromobutane (at low temperature), 2,3–dibromobutane (at low temperature), and 1,2–dibromoethane (both at ambient and at low temperature) however, this approach was not well behaved, with both $N_X$ and $2\sigma^2$ refining towards zero. For these cases the results given in Table 3.6 refer to the calculations with $N_X$ fixed.

For those cases in which $N_X$ could be refined, the final value of $N_X$ was significantly larger than the initial value of $N_X = 1.5$ or 3. Since the occupancy, $N_X$, and the Debye–Waller factor, $2\sigma_X^2$, are strongly correlated, the amount of physical significance that can be attached to either of these parameters for the halogen shell is doubtful. In any case, these parameters might partially compensate for inadequacies in the approximations made in the structural models. For the inclusion compound containing 1,2–dibromo-

ethane, Model 3 does not represent a statistically significant improvement with respect to Model 1 (either at ambient or low temperature). This suggests that there is no significant ordering of the bromine atoms of the guest molecules relative to the nickel atoms of the host structure. It is not certain why this behaviour is observed only for the latter compound.

## 3.4  Conclusion

For all compounds investigated here, the environment of the absorbing nickel atoms of the host structure can be described with a single, averaged C–N–Cd unit. The subtle differences observed by single crystal X–ray diffraction [50, 51] are not detectable in the nickel K–edge EXAFS spectra. For all compounds (with the exception of the 1,2–dibromoethane/Cd(pn)Ni(CN)$_4$ inclusion compound), the addition of a single, averaged halogen shell results in a statistically significant improvement in the fit to the EXAFS data, with physically sensible values of the refined Ni$\cdots$Cl and Ni$\cdots$Br distances. The fact that well defined shells can be observed for the halogen atoms of the guest molecules suggests that, both at ambient and at low temperature, there is a substantial amount of ordering of the guest molecules within the tunnels of the host structure. However, as all compounds yield similar results in terms of the distance of the halogen shell with respect to the central nickel atom, more detailed investigations of the structural properties of these inclusion compounds are called for. EXAFS spectroscopy at the cadmium absorption edge (for the host substructure) and at the bromine absorption edge (for the guest substructure, *vide supra*), could provide a more detailed insight of the local structure with respect to the specific absorbers. As combined refinements of EXAFS spectra from several different absorbers are feasible, obtaining a more complete picture of the structural relationship between host and guest materials is conceivable, providing the availability of experimental data.

Certain issues will, however, remain elusive if only further EXAFS exper-
iments are considered. The stark changes of the local environment observed
in the 1,2–dichloroethane, 2–bromobutane and 2,3–dibromobutane inclusion
compounds (compared to the remaining materials investigated) on lowering
the temperature could, as mentioned above, be due to structural phase transi-
tions. To resolve the issue of phase transitions would require the use of other
techniques such as calorimetric measurements over a range of temperatures or
variable temperature X–ray diffraction, to probe structural changes directly.

To further investigate the dynamic properties of the guest materials in
the tunnels of the host substructure, NMR measurements could supply valu-
able insights. Another set of techniques used to explore dynamic properties of
materials, inelastic and quasielastic neutron scattering (see Section 2.3) would
necessarily fail in the case of these particular materials due to the cadmium
content of the inclusion compounds, since cadmium efficiently absorbs neu-
trons.

# Chapter 4

# Temperature Dependent Structural Properties of the Thiourea/Chlorocyclohexane Inclusion Compound

## Abstract

The structural properties of the thiourea/chlorocyclohexane inclusion compound have been determined, using Rietveld refinement techniques, from synchrotron X–ray powder diffraction data. Diffraction patterns were recorded at temperatures above and below the phase transition temperature of *ca.* 192 K. The structure determined for the high temperature phase at both 289 K and 199 K is in agreement with that previously reported from single crystal X–ray diffraction data. The thiourea molecules form a rhombohedral host structure containing parallel, linear, infinite tunnels, with the chlorocyclohexane guest molecules substantially disordered within these tunnels. The host substructure in the low temperature phase is sufficiently similar to the high temperature phase, so that the latter can be used as the initial structural

model for the Rietveld refinement in the low temperature phase. The low temperature phase, studied at 185 K and 85 K, is monoclinic (space group $P2_1/a$: a $\approx$ 9.9 Å, b $\approx$ 16.0 Å, c $\approx$ 12.5 Å, $\beta$ $\approx$ 113.9°), with both the host and the guest substructure characterised by well defined atomic positions. The host substructure is a distorted form of the rhombohedral structure of the high temperature phase. The guest molecules form an ordered head–head/tail–tail arrangement with an intermolecular chlorine–chlorine distance of 4.6 Å at 85 K. The chlorine atom is in an axial position with respect to the cyclohexane ring, giving direct confirmation of previous spectroscopic investigations. In the refined structure, the cyclohexane ring has a conformation resembling an envelope, although it is not clear if this deviation from the standard chair conformation is a genuine structural feature or an artefact of the refinement calculations.

# 4.1 Introduction

It has been known for some time [62, 63, 64, 65], that thiourea forms inclusion compounds with suitable guest molecules. These inclusion compounds consist of an extensively hydrogen bonded structure of thiourea molecules containing linear, non–intersecting tunnels. The projection of the tunnels perpendicular to the tunnel axis is of hexagonal appearance [48, 49, 52]. The crystal symmetry is generally rhombohedral and, at ambient temperature, the lattice parameters (in the hexagonal description) are *ca.* a = 15 Å and c = 12 Å, regardless of the guest molecule[1]. In contrast, the structure of pure thiourea is orthorhombic and does not contain any empty tunnels [67].

In the thiourea inclusion compounds, the guest molecules are contained within the tunnels of the host structure. The size and type of guest molecule

---

[1]Some exceptions are known, notably for large guest molecules such as 2,6–diethylnaphthalene [66].

is limited by the diameter of the tunnel. Examples of guest molecules which are known to form inclusion compounds with thiourea are branched hydrocarbons [48, 49], cyclic hydrocarbons (e.g. cyclohexane and substituted cyclohexanes [49, 52]), polycyclic hydrocarbons (e.g. adamantane [68]), metallocenes (e.g. ferrocene [69]), and certain organometallics [11, 12]. In general the stoichiometry of the inclusion compounds containing cyclic guest molecules is such that the molecular host to guest ratio is 3:1.

Of the guest molecules mentioned above, some inclusion compounds containing organometallic guest molecules show interesting optical properties. For certain guest molecules (details can be found in reference [11]), the arrangement of the guest molecules is acentric. These materials show Second Harmonic Generation from 1060 nm Nd:YAG laser light and are of potential interest in data storage technology.

Thiourea inclusion compounds of monosubstituted cyclohexanes are notable for the unusual conformational properties of the guest molecules. In the pure liquid and vapour phases of monohalogenocyclohexanes, conformational equilibrium favours the equatorial conformer [70, 71, 72]. In the pure solid, at low temperature or sufficiently high pressure, the molecules exist solely in the equatorial conformation [71, 73].

In the thiourea inclusion compounds, the predominant conformation of the monohalogenocyclohexane guest molecules, however, is the axial conformation [74, 75]. The amount of the equatorial conformer is dependent on the halogen, but is generally less than 10% [74]. This interesting conformational behaviour is undoubtedly due to the restrictions imposed on the guest molecules by the host structure.

The diameter of the thiourea tunnel is not uniform along the length of the tunnel. It has been shown [76], that the diameter varies substantially, with a minimum value of ca. 5.8 Å and a maximum value of ca. 7.1 Å. In this respect, the tunnels resemble cage–type structures, which is reflected in the

dynamic properties of the guest molecules. Since there is no chemical bonding between the host and the guest, the guest molecules can be expected to possess considerable motional freedom. However, due to the constriction in the tunnel, the amount of translational freedom of the guest molecules, in the direction of the tunnels, will be restricted. The dynamic properties of a number of guest molecules included in a thiourea host matrix have been investigated by NMR spectroscopy [77, 78, 79, 80, 81, 82, 83] and it is clear from these experiments that the guest molecules exhibit substantial dynamic disorder at sufficiently high temperature. A more detailed discussion of the dynamic properties of guest molecules in thiourea inclusion compounds can be found in Chapter 6.

Dynamic disorder of the guest molecules is also apparent in the results of some X–ray diffraction studies of these inclusion compounds [52]. Although the guest molecules clearly contribute to the observed intensities in the diffraction pattern and the molecules are seen to be confined within certain regions of the tunnel, generally a discernible molecular structure cannot be observed. For the inclusion compounds containing ferrocene and cyclohexane, respectively, low temperature phase transitions have been reported [84, 85]. The phase transition is associated with a freezing of the motion of the guest molecules. For both compounds, the phase transitions have been investigated by single crystal X–ray diffraction. For the the thiourea/cyclohexane inclusion compound a lowering of the crystal symmetry was ascribed [77] to a transition to a monoclinic phase. Although a possible crystal symmetry was proposed (*vide infra*) for the low temperature phase [77], a detailed account of the structure of the new phase was not given.

In the case of ferrocene, twinning of the crystal upon crossing the phase transition temperature precluded the possibility to determine the structural changes in this compound [86]. Due to the rhombohedral symmetry of the ambient temperature phase of the thiourea inclusion compounds, lowering of symmetry can be accomplished by equivalent distortions of the high symmetry

unit cell in different directions, naturally leading to twinning of the crystals.

The aim of the experiments discussed in this chapter was to determine the existence of similar transitions for the thiourea/chlorocyclohexane inclusion compound and to assess the structural properties of any low temperature phase. For this purpose, variable temperature powder X–ray diffraction experiments were carried out. The technique is ideally suited for investigations of this type, since any twinning of crystals would not affect the already random orientational distribution of the crystallites in the polycrystalline sample. Common problems associated with twinning in single crystal diffraction experiments are thus avoided.

## 4.2 Experimental

### 4.2.1 Preparation of the Thiourea/Chlorocyclohexane Inclusion Compound

A solution of thiourea in methanol was prepared at *ca.* 50°C. Chlorocyclohexane was added to the solution in excess of the expected molar ratio of 3:1 (thiourea to chlorocyclohexane in the product). Any immediate precipitate was dissolved by adding methanol. Over a period of several days, the solution was cooled to 4°C in an incubator.

The precipitate was collected by filtration and washed with a small amount of methanol in order to remove any excess chlorocyclohexane adhering to the surfaces of the crystals. The crystals were briefly dried on filter paper and stored in a sealed container at 4°C to prevent decomposition of the inclusion compound.

The structure of the crystals at ambient temperature was confirmed by X–ray powder diffraction to be that of the thiourea/chlorocyclohexane inclusion compound.

### 4.2.2 X–Ray Powder Diffraction

X–ray powder diffractograms were recorded at station 2.3 at the Synchrotron Radiation Source, Daresbury. A finely ground sample of thiourea/chlorocyclohexane was placed in a circular, flat sample holder and covered with Kapton film. Diffractograms were recorded in reflection geometry in the range $10° \leq 2\theta \leq 80°$ with a step size of $0.01°$ and a counting time of 4 s per step. The X–ray wavelength was 1.50 Å.

The X–ray powder diffractogram of thiourea/chlorocyclohexane was recorded at two temperatures above the phase transition (289 K and 199 K) and at two temperatures below the phase transition (185 K and 85 K). The temperature was stable to within $\pm 2$ K for the experiments at 289 K, 185 K and 85 K. For the experiment at 199 K, however, a sharp increase in temperature of *ca.* 10 K was observed between $2\theta = 35°$ and $2\theta = 40°$ and the overall variation in temperature (disregarding the sharp rise) was $\pm 5$ K.

Prior to the data analysis, the raw data were normalized to the incident X–ray intensity in order to account for the natural decay of the incident photon beam during the experiment.

## 4.3 Models for the Transition of the Rhombohedral High–Temperature Phase of the Thiourea/Chlorocyclohexane Inclusion Compound to Lower Symmetry

The crystal structure of the high temperature phase of thiourea/chlorocyclohexane has been determined previously [52]. The structure is characterized by a rhombohedral lattice. From this lattice, several simple transformations to lower symmetry lattices can be envisaged and these will now be discussed

together with the characteristic splitting patterns in powder diffraction peaks accompanying the associated transitions. The discussion will be restricted to describing the predicted effect upon the reflections at low scattering angles ($\leq 30°$) in the high temperature phase. Due to the low scattering angles and the lack of peak overlap, these reflections are likely to be the most instructive.

**A**: Within a rhombohedral lattice, it is possible to construct a hexagonal unit cell. The volume of the hexagonal cell is three times that of the rhombohedral cell. One transformation (six exist, corresponding to different orientations of the hexagonal unit vectors) describing the relationship between the rhombohedral and hexagonal lattice vectors is

$$(\underline{a}_H\,\underline{b}_H\,\underline{c}_H) = (\underline{a}_R\,\underline{b}_R\,\underline{c}_R) \begin{pmatrix} 1 & 0 & 1 \\ \bar{1} & 1 & 1 \\ 0 & \bar{1} & 1 \end{pmatrix} \tag{4.1}$$

where the subscript $R$ denotes the rhombohedral lattice vectors and the subscript $H$ denotes the the hexagonal lattice vectors. The following conditions hold for the hexagonal unit cell in the rhombohedral lattice:

$$a = b \quad \alpha = \beta = 90° \quad \gamma = 120° \tag{4.2}$$

Relaxing the condition $a = b$ and/or the condition $\gamma = 120°$ results in a reduction of the metric lattice symmetry to monoclinic. Applying the same transformation to all reflections contributing to a given peak, the corresponding reflections in the lower symmetry structure can be determined. To assess which of these correspond to a form in the lower symmetry structure, appropriate tables are used (see Reference [87]). The reflections of the rhombohedral phase in the aforementioned range of scattering angles are compared to the new peaks generated by the various models described here in Table 4.1.
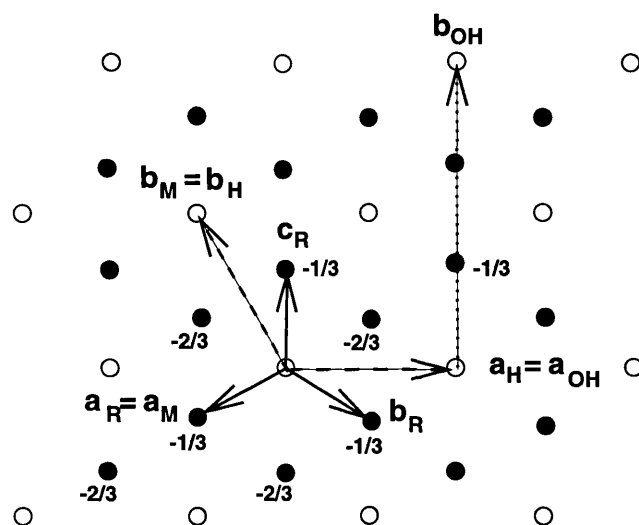
**Figure 4.1:** Comparison of the unit vectors for the various unit cells derived
from the rhombohedral lattice. The models are distinguished by the subscripts
of the axes, which are the same as used in the text. The c-axis of all three
models is perpendicular to the plane of the representation. For reasons of
clarity, the lattice points corresponding to a primitive hexagonal lattice are
shown as open circles, the filled circles indicate the positions of the additional
rhombohedral lattice points.

**B:** In a lattice of hexagonal symmetry, it is possible to define an or-
thorhombic unit cell. Clearly, this is also true for a lattice of rhombohedral
symmetry. This orthohexagonal cell has twice the volume of the hexagonal
cell and, therefore, six times the volume of the rhombohedral cell. One trans-
formation relating the hexagonal with the orthorhombic unit vectors is:

$$(\underline{a}_{OH}\, \underline{b}_{OH}\, \underline{c}_{OH}) = (\underline{a}_H\, \underline{b}_H\, \underline{c}_H) \begin{pmatrix} 1 & 1 & 0 \\ 0 & 2 & 0 \\ 0 & 0 & 1 \end{pmatrix} \tag{4.3}$$

Here the subscript $OH$ denotes the orthorhombic unit cell and $H$ again
denotes the hexagonal unit cell. As seen in Figure 4.1, this orthorhombic
cell is C-centred. Further conditions relating the hexagonal unit cell to the

orthorhombic unit cell are

$$a_{OH} = a_H, \quad b_{OH} = 2a_O H \cos 30° \quad \text{and} \quad c_{OH} = c_H \qquad (4.4)$$

and the rhombohedral metric lattice symmetry can be lowered to orthorhombic metric lattice symmetry by relaxing the condition $b_{OH} = 2a_{OH}cos(30°)$, either with or without loss of C–centering.

C: A less obvious transformation was used by Clement *et al.* [77] to describe the phase transition in the thiourea/cyclohexane inclusion compound. The transformation relates the rhombohedral lattice vectors to a monoclinic unit cell and is:

$$(\underline{a}_M\,\underline{b}_M\,\underline{c}_M) = (\underline{a}_R\,\underline{b}_R\,\underline{c}_R) \begin{pmatrix} 1 & 0 & \bar{1} \\ 0 & \bar{1} & \bar{1} \\ 0 & 1 & \bar{1} \end{pmatrix} \qquad (4.5)$$

The subscript $M$ denotes the monoclinic lattice vectors, whereas $R$ denotes the rhombohedral lattice vectors as above. This cell has twice the volume of the rhombohedral cell and is also C–centred. The $a_M$–axis is identical to the $a_R$–axis, the $b_M$– and $c_M$–axes are of the same magnitude as the $b_H$– and $c_H$–axes. Therefore, the following relationships hold for the magnitudes of the monoclinic and the rhombohedral basis vectors in the rhombohedral lattice

$$a_M = a_R, \quad b_M = 2a_R \sin\frac{\alpha}{2} \quad \text{and} \quad c_M = a_R\sqrt{3}\sqrt{1 + 2\cos\alpha}$$

$$(4.6)$$

Relaxing any of these conditions, either with or without the loss of C–centering, results in a monoclinic lattice.

**Table 4.1:** Peak splitting for the peaks observed in the high temperature phase of thiourea/chlorocyclohexane at low scattering angle as predicted by the various models described in the text. Only one set of (hkl) is given per form along with the multiplicity of the form (in brackets). The scattering angle $2\theta$ refers to the observed peak positions in the high temperature phase only. For some reflections a given transformation may only generate half of the reflections constituting a form in the lower symmetry. These are marked with an asterisk

| $2\theta$ / Å | High Temperature Phase | Model A | Model B | Model C |
|---|---|---|---|---|
| 10.77 | {10$\bar{1}$} (6) | {$\bar{2}$10} (2)<br>{$\bar{1}$20} (2)<br>{110} (2) | {130} (4)<br>{200} (2) | {110} (4)<br>{020} (2) |
| 15.13 | {110} (6) | {$\bar{1}$02}* (4)<br>{012}* (4)<br>{1$\bar{1}$2}* | {11$\bar{2}$}* (8)<br>{022}* (4) | {11$\bar{2}$} (4)<br>{002} (2) |
| 17.89 | {20$\bar{1}$} (12) | {211}* (4)<br>{12$\bar{1}$}* (4)<br>{$\bar{3}$21}* (4)<br>{2$\bar{3}$$\bar{1}$}* (4)<br>{31$\bar{1}$}* (4)<br>{1$\bar{3}$1}* (4) | {241}* (8)<br>{311}* (8)<br>{1$\bar{5}$1}* (8) | {2$\bar{1}$$\bar{1}$} (4)<br>{121} (4)<br>{031} (4) |
| 18.62 | {200} (6) | {202}* (4)<br>{0$\bar{2}$2}* (4)<br>{$\bar{2}$22}* (4) | {222}* (8)<br>{0$\bar{4}$2}* (4) | {20$\bar{2}$} (2)<br>{022} (4) |
| 18.71 | {11$\bar{2}$} (6) | {030} (2)<br>{300} (2)<br>{3$\bar{3}$0} (2) | {330} (4)<br>{060} (2) | {130} (4)<br>{200} (2) |
| 21.63 | {20$\bar{2}$} (6) | {220} (4)<br>{040} (2) | {260}* (4)<br>{$\bar{2}$20}* (4)<br>{080} (2) | {220} (4)<br>{040} (2) |
| 23.40 | {210} (12) | {113} (4)<br>{123} (4)<br>{213} (4) | {133} (8)<br>{203} (4) | {21$\bar{3}$} (4)<br>{013} (4)<br>{12$\bar{3}$} (4) |
| 23.60 | {21$\bar{2}$} (12) | {131}* (4)<br>{311}* (4)<br>{$\bar{4}$11}* (4)<br>{$\bar{1}$41}* (4)<br>{3$\bar{4}$1}* (4)<br>{4$\bar{3}$1}* (4) | {171}* (8)<br>{421}* (8)<br>{3$\bar{5}$1}* (8) | {23$\bar{1}$} (4)<br>{211} (4)<br>{14$\bar{1}$} (4) |

## 4.4   Results and Discussion

Figure 4.2 shows the temperature dependence of the powder diffraction pattern
of thiourea/chlorocyclohexane recorded at the Synchrotron Radiation Source.
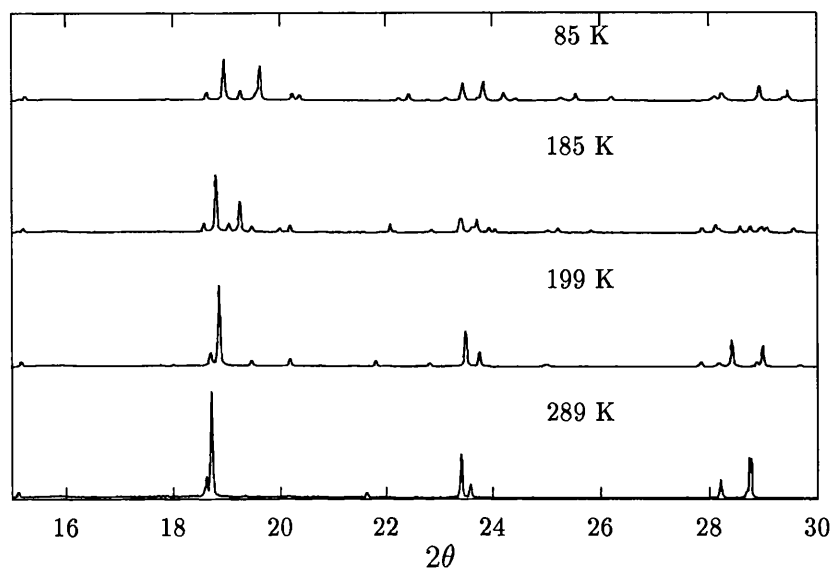


**Figure 4.2:** Diffraction pattern of the thiourea/chlorocyclohexane at various temperatures. Only the region from $15° \leq 2\theta \leq 30°$ is shown and the changes occuring in the diffraction pattern on crossing the phase transition temperature are clearly visible.

### 4.4.1   Determination of Lattice Parameters and Space Group in the High Temperature Phase and the Low Temperature Phase

The ambient temperature (289 K) X–ray powder diffractogram can be indexed
on the basis of a rhombohedral lattice, with lattice parameters a = 10.442 Å
and $\alpha$ = 104.22°. The systematic absences are consistent with the space group
$R\bar{3}c$, as determined previously from single crystal X–ray diffraction data [52].

Upon lowering the temperature to 199 K, new low–intensity peaks evolve, which cannot be indexed on the basis of the rhombohedral unit cell. They are attributed to pure thiourea, which is known [88] to form as a decomposition product of the inclusion compound under irradiation with X–rays. Only one sample was used to obtain all diffractograms discussed here, and it can be seen that these peaks become more prominent as the experiment progresses.

In Figure 4.3 a section of the powder diffractogram is shown, together with the indexing of the peaks. The peaks due to pure thiourea are also indicated.

At 185 K, after crossing the phase transition temperature, a clear splitting of the peaks is observed. The peaks indexed as $(10\bar{1})$ and $(110)$ in the high temperature phase (Figure 4.3, top) each split into two peaks with an approximate intensity ratio of 1:2 (Figure 4.3, bottom). The low intensity peak indexed as $(201)$ in the high temperature phase has separated into at least two peaks in the low temperature phase. Since the respective intensities of these peaks barely exceed the level of background scattering, the exact mode of splitting cannot be determined. For the two peaks in the high temperature phase indexed as $(11\bar{2})$ and $(20\bar{2})$ respectively, the splitting is well defined. Below the phase transition temperature, the first of these two peaks separates into two peaks with an intensity ratio close to 1:1. The second, more intense peak, also generates two new peaks, this time with an intensity ratio of 2:1.

Beyond the scattering angle of $2\theta = 20°$ the number of peaks in close proximity increases rapidly in both phases. This makes a definite determination of the origin of the new peaks difficult if not impossible. The amount of information contained in the $2\theta$ range below $20°$ is, however, sufficient to rule out the proposed hexagonal to monoclinic transition, since this would require all of the peaks in the high temperature phase discussed so far to generate three daughter peaks (see Table 4.1). Clearly this is not the case.
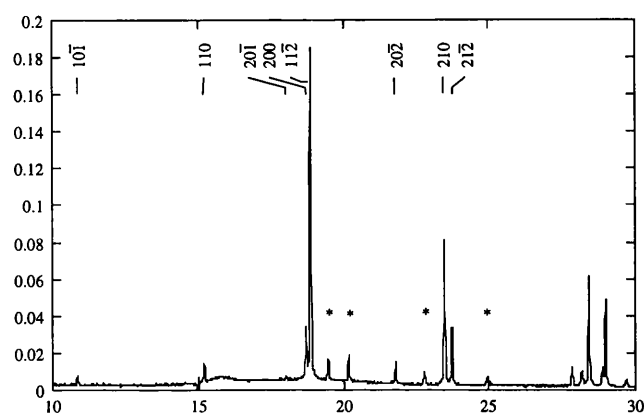
(a) 199 K
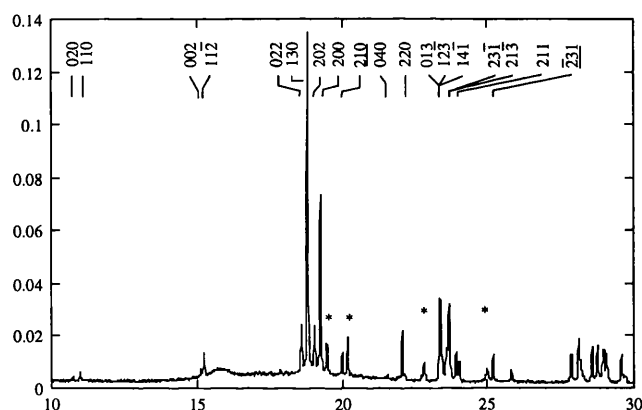


(b) 185 K

**Figure 4.3:** Comparison of the low $2\theta$ peaks in the diffractograms at 199 K and 185 K. The peak splitting is evident. Some peaks have been indexed for easier comparison with Table 4.1. Those peaks due to decomposition of the inclusion compound and formation of a thiourea impurity are marked with an asterisk. Those peaks appearing for the first time in the low temperature phase due to the loss of C–centering are underlined.

From the appearance of the peaks in the range $21.6° \leq 2\theta \leq 23.6°$, it is not possible to distinguish between the other two proposed models. It is in this region that the first differences should become apparent, yet the overlap of peaks precludes any interpretation based on the proposed models.

Since the unit cell generated by the rhombohedral to monoclinic transition is considerably smaller (and therefore simpler) than that generated by

the rhombohedral to orthorhombic transition, the peaks at $2\theta = 10.73°(020)$; $10.99°(110)$; $15.11°$ and $15.22°(11\bar{2})$ were tentatively indexed assuming the transition to monoclinic symmetry. These peaks are sufficient to determine the lattice parameters for the unit cell as a $= 9.8$ Å, b $= 16.0$ Å, c $= 12.5$ Å, and $\beta = 113.95°$. From these lattice parameters, expected peak positions can be calculated and compared to the experimental diffractograms. All of the peaks in the diffractogram (except for those unambiguously assigned to the pure thiourea phase) can be indexed on the basis of this unit cell.

In the diffractogram recorded at 185 K, some new peaks appear, which cannot be assigned to the pure thiourea phase. These peaks represent genuine reflections from the inclusion compound, which previously had insignificant intensity due to the symmetry of the high temperature phase: the monoclinic unit cell within the rhombohedral lattice is C–centred, and hence the reflections with indices where $h + k$ is odd (in the monoclinic description) are absent. In the new phase, C–centering is clearly lost, and these reflections are no longer required to have zero intensity.

The intensities of the diffraction maxima in the low temperature phase are consistent with the space group $P2_1/a$. The associated point group $2/m$ is the holosymmetric point group of the monoclinic crystal system. For the high temperature phase, the point group is $\bar{3}m$, which is the holosymmetric point group in the trigonal crystal system, yet the intensity ratios of some daughter peaks in the low temperature phase do not behave as predicted (see Section 2.2.1 and Table 4.1). Recalling that the guest molecules display a high degree of dynamic disorder in the high temperature phase, this observation is not wholly surprising. If the transition is associated with a freezing of this motion, the electron density of the guest substructure will become localized and will contribute to the diffraction pattern of the low temperature phase differently than the electron density of the dynamically disordered guest in the high temperature phase (see also Chapter 6).

## 4.4.2 Rietveld Refinements of the Synchrotron X–Ray Powder Diffractograms

**High Temperature Phase**

The first structural model for the Rietveld refinement calculations contained only the host substructure taken from the single crystal X–ray diffraction results. This model did not lead to a well behaved refinement. The guest substructure clearly represents a significant contribution to the diffraction pattern, even though the guest molecules are substantially disordered [52, 74, 89, 90].

The second initial structural model for the refinement calculations contained the complete set of parameters determined previously [52] from single crystal diffraction data. In this model, the time averaged electron density distribution of the disordered guest substructure is approximated by discrete positions with appropriate fractional occupancy and high atomic displacement parameters. However, this structural model also led to a poorly behaved refinement.

To obtain a satisfactory refinement of the structure of the high temperature phase, the following strategy was adopted. The parameters previously determined for the host and guest substructures [52] were used, but only the parameters of the host substructure were refined. Following this refinement, the guest atoms were removed from the model and a difference Fourier calculation was performed using only the host atoms as a structural model. Peaks in the difference Fourier map positioned within the tunnel were used as initial structural model for the guest molecules, one representing a chlorine atom and two representing carbon atoms.

Bearing in mind that the point symmetry of the guest molecule is $m$ (whereas the point symmetry of a general position along the tunnel is $\mathcal{3}$) and that the guest molecules are dynamically disordered at sufficiently high

temperature [52, 74] it is not surprising that no combination of peaks found in the difference Fourier map represents a recognizable structure for chloro-cyclohexane. However, as the guest molecules clearly contribute to the same peaks in the diffraction pattern, the time averaged symmetry of the guest substructure must be the same as that of the host substructure. To fit the diffraction pattern satisfactorily, a structural model accounting for intensity contributions from both the host and the guest substructures must be employed. Within the constraints of the program used for the refinements, the only way to account for the guest electron density is to introduce discrete atoms with appropriate fractional site occupancies and high atomic displacement parameters. Therefore little physical significance can be assigned to the refined parameters of the guest atoms.

The complete structural model was then refined. Constraints based on standard molecular geometry were applied to the bond lengths and bond angles of the thiourea molecule [2]. The values of the restraints are given in Table 4.4. The initial site occupancies for the guest atoms were fixed as $\frac{1}{6}$ for chlorine and $\frac{1}{2}$ for each of the carbon atoms. These occupancies represent two chlorocyclo-hexane molecules per unit cell and a stoichiometry of one chlorocyclohexane molecule per three thiourea molecules.

Atomic coordinates and isotropic atomic displacement parameters were refined for all atoms. In the final stages of the calculations the site occupancy of the guest atoms was allowed to vary simultaneously with the atomic displacement parameter. Here, this is not critical since these parameters are not subject to any interpretation and serve only to optimize the representation of the guest atoms within the limitations of the refinement program. In general, these two parameters should not be refined simultaneously, as they are highly correlated.

---

[2]Within GSAS, it is not possible to constrain the bond angles directly. Bond angles can, however, be constrained sufficiently by constraining next–nearest neighbour distances.

The final refined structural parameters at 289 K are reported in Table 4.2 and the experimental and calculated X–ray powder diffractograms are compared in Figure 4.4. The final refined structure is shown in Figure 4.5

**Table 4.2:** Refined structural parameters for the high temperature phase of thiourea/chlorocyclohexane at 289 K. The rhombohedral setting of the unit cell is used (space group $R\bar{3}c$; a = 10.1224(1) Å, $\alpha$ = 104.2204(3)°). Goodness–of–fit indices are $R_p$ = 0.096, $R_{wp}$ = 0.135.

| atom | x/a | y/b | z/c | $U_{iso}$ / Å$^2$ | site occupancy |
|------|-----|-----|-----|-------------------|----------------|
| host |     |     |     |                   |                |
| S | -0.5531(2) | $\frac{3}{4}$ | 0.0531(2) | 0.095(5) | 1 |
| C | -0.6585(7) | $\frac{3}{4}$ | 0.1585(7) | 0.040(5) | 1 |
| N | 0.1912(7) | 0.6729(8) | 0.1113(7) | 0.096(4) | 1 |
| guest |     |     |     |                   |                |
| Cl | 0.170(5) | 0.009(6) | 0.168(5) | 0.31(3) | 0.30(3) |
| C(1) | 0.37(1) | 0.21(1) | 0.23(1) | 0.20(3) | 0.40(8) |
| C(2) | 0.095(4) | 0.107(4) | 0.269(3) | 0.18(3) | 0.9(1) |
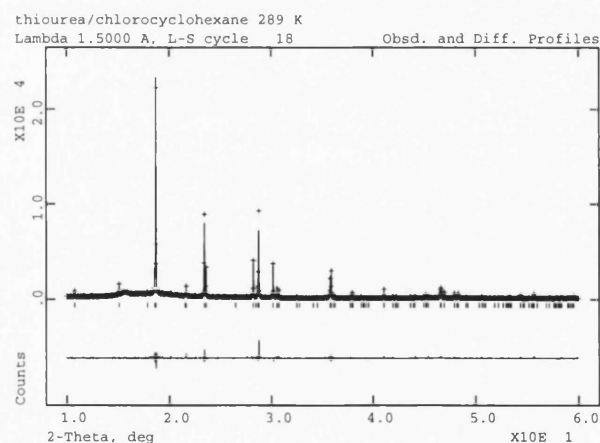


**Figure 4.4:** Comparison of the experimental diffractogram of thiourea/chlorocyclohexane inclusion compound at 289 K to the calculated diffractogram. The crosses represent the experimental data and the full line is the calculated diffractogram. Beneath the difference diffractogram is shown.

**Figure 4.5:** Stucture of the high temperature phase of thiourea/chlorocyclo-hexane determined at 289 K. The structure is viewed along the tunnel axis and the positions of the guest "atoms" used in the refinement calculations are shown.

Similar structural properties were derived in the Rietveld refinement from the X-ray powder diffractogram recorded at 199 K. The final refined structural parameters at 199 K are reported in Table 4.3, and the experimental and calculated X-ray powder diffractograms are compared in Figure 4.6.

**Table 4.3:** Refined structural parameters for the high temperature phase of thiourea/chlorocyclohexane at 199 K. The rhombohedral setting of the unit cell is used (space group $R\bar{3}c$; a = 10.0553(2) Å, $\alpha$ = 104.0961(4)°). Goodness–of–fit indices are: $R_p$ = 0.126, $R_{wp}$ = 0.211.

| atom | x/a | y/b | z/c | $U_{iso}$ / Å$^2$ | site occupancy |
|------|-----|-----|-----|---------|----------------|
| host |     |     |     |         |                |
| S | -0.5491(3) | $\frac{3}{4}$ | 0.0491(3) | 0.1040(3) | 1 |
| C | -0.664(1) | $\frac{3}{4}$ | 0.164(1) | 0.089(9) | 1 |
| N | 0.1889(8) | 0.6723(9) | 0.0961(8) | 0.046(4) | 1 |
| guest |     |     |     |         |                |
| Cl | 0.189(6) | 0.012(6) | 0.162(5) | 0.01(3) | 0.10(2) |
| C(1) | 0.438(8) | 0.396(5) | 0.273(6) | 0.20(1) | 0.60(6) |
| C(2) | 0.397(7) | 0.222(7) | 0.323(7) | 0.20(1) | 0.78(8) |



**Figure 4.6:** Comparison of the experimental diffractogram of thiourea/chlorocyclohexane inclusion compound at 199 K to the calculated diffractogram. The crosses represent the experimental data and the full line is the calculated diffractogram. Beneath the difference diffractogram is shown.
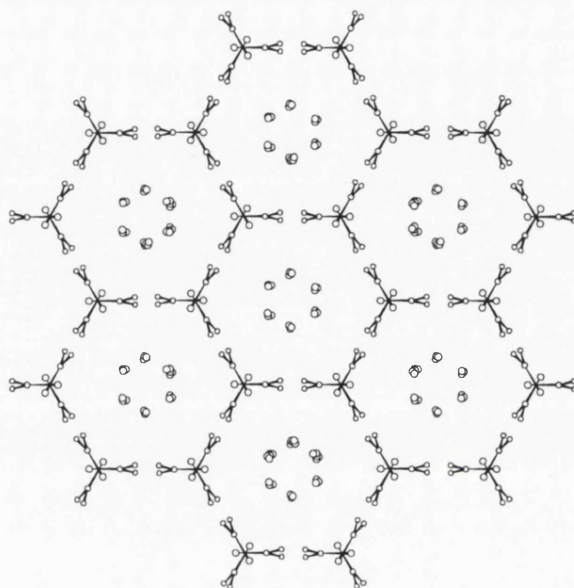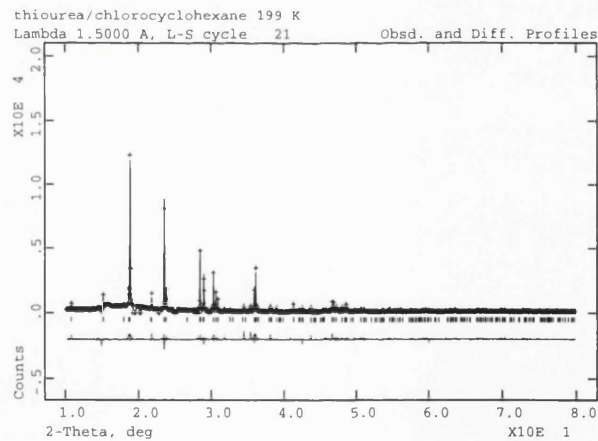
### Low Temperature Phase

For the Rietveld refinement of the low temperature phase the following strategy was adopted. The initial structural model contained the coordinates of the host atoms in the high temperature phase, transformed to the monoclinic description according to the transformation specified in Equation 4.5. The initial positions of the guest atoms were determined from the positions of appropriate peaks (namely those located within the tunnel) in the difference Fourier map calculated for the initial, unrefined host substructure. For this initial structural model, only the parameters of the host substructure were refined until a satisfactory fit to the experimental data was achieved.

The positions of the guest atoms were then discarded and redetermined from a difference Fourier map calculated for a model comprising this refined host substructure only. The resulting difference Fourier map contained one dominant peak, which was assigned to the chlorine atom of the guest molecule. From other significant peaks in the difference Fourier map, plausible positions for the carbon atoms of the guest molecule were recognized.

The complete structure (i.e. both host and guest substructures) was then refined. Constraints based on standard molecular geometries (see Table 4.4 and footnote on page 94) were applied to the bond lengths and bond angles of both the thiourea and chlorocyclohexane molecules.

Isotropic atomic displacement parameters were refined, with common values used for each atom type of the host, and a common value used for the carbon atoms of the guest.

The free refinement of the common isotropic atomic displacement parameter for the nitrogen atoms of the thiourea led to this parameter refining towards an unreasonably low value; this problem could be overcome only by fixing this parameter at a standard value ($0.025$ Å$^2$). The site occupancies of all atoms were fixed at 1. The final refined structural parameters at 85 K are given in Table 4.5, and the experimental and calculated X–ray powder diffrac-

tograms are compared in Figure 4.7. The final refined structure is shown in Figure 4.8 .

**Table 4.4:** Values of constraints used for the thiourea molecule and for the chlorocyclohexane molecule. The bond angles were constrained indirectly by constraining the next–nearest neighbour distance. Both the value of the bond angle and the next–nearest neighbour distance are given.

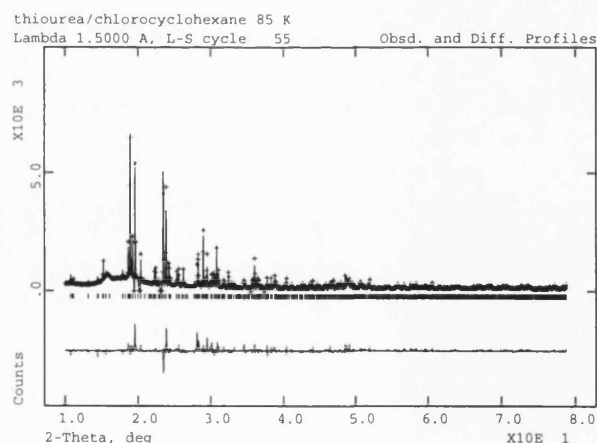| Atoms | Distance / Å | Bond Angle |
|-------|-------------|------------|
| host | | |
| S–C | 1.72 | |
| C–N | 1.35 | 120° |
| S–N | 2.67 | 120° |
| N–N | 2.34 | 120° |
| guest | | |
| Cl–C | 1.92 | |
| Cl–C–C | 2.81 | 109.47° |
| C–C | 1.52 | |
| C–C–C | 2.48 | 109.47° |



**Figure 4.7:** Comparison of the experimental diffractogram of thiourea/chlorocyclohexane inclusion compound at 85 K to the calculated diffractogram. The crosses represent the experimental data and the full line is the calculated diffractogram. Beneath the difference diffractogram is shown.

**Table 4.5:** Refined structural parameters for the low temperature phase of thiourea/chlorocyclohexane at 85 K (space group $P2_1/a$; $a = 9.6511(3)$ Å, $b = 15.9636(4)$ Å, $c = 12.4784(4)$ Å, $\beta = 114.22°$). Goodness-of-fit indices are: $R_p = 0.134$, $R_{wp} = 0.190$. Parameters labelled [F] were fixed at standard values during the refinement calculation (see text for discussion).

| atom | x/a | y/b | z/c | $U_{iso}/Å^2$ |
|---|---|---|---|---|
| host | | | | |
| S(1) | 0.543(1) | 0.2005(5) | 0.779(1) | 0.016(2) |
| S(2) | 0.488(1) | 0.1381(6) | 0.4226(9) | 0.016(2) |
| S(3) | 0.599(1) | 0.1434(6) | 0.129(1) | 0.016(2) |
| C(1) | 0.531(4) | 0.083(1) | 0.782(3) | 0.029(7) |
| C(2) | 0.666(3) | 0.198(2) | 0.474(3) | 0.029(7) |
| C(3) | 0.431(3) | 0.209(2) | 0.070(3) | 0.029(7) |
| N(1) | 0.527(3) | 0.047(1) | 0.875(2) | 0.0250 [F] |
| N(2) | 0.694(3) | 0.238(2) | 0.574(2) | 0.0250 [F] |
| N(3) | 0.352(3) | 0.207(2) | 0.140(2) | 0.0250 [F] |
| N(4) | 0.394(3) | 0.251(1) | 0.971(2) | 0.0250 [F] |
| N(5) | 0.465(3) | 0.053(1) | 0.667(2) | 0.0250 [F] |
| N(6) | 0.750(3) | 0.211(2) | 0.409(2) | 0.0250 [F] |
| guest | | | | |
| Cl | 0.117(1) | 0.0752(7) | 0.901(2) | 0.095(5) |
| C(4) | 0.926(3) | 0.049(1) | 0.765(2) | 0.024(5) |
| C(5) | 0.094(3) | 0.043(2) | 0.200(3) | 0.024(5) |
| C(6) | 0.922(3) | 0.019(2) | 0.342(3) | 0.024(5) |
| C(7) | 0.035(3) | 0.094(2) | 0.374(3) | 0.024(5) |
| C(8) | 0.021(4) | 0.101(1) | 0.247(3) | 0.024(5) |
| C(9) | 0.008(4) | 0.062(2) | 0.670(3) | 0.024(5) |
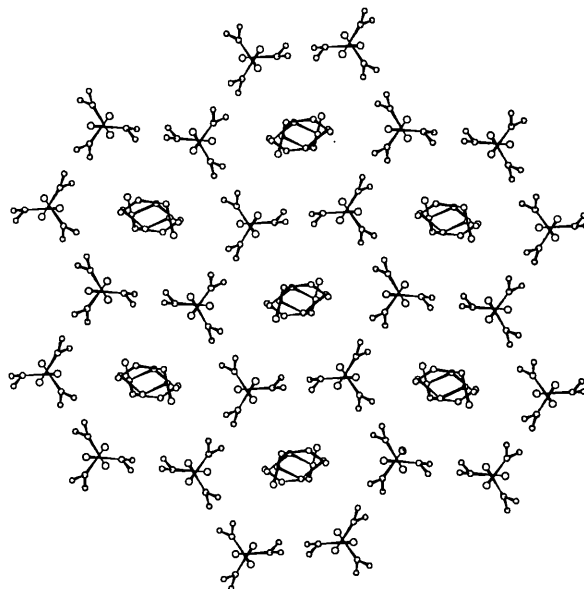
**Figure 4.8:** Stucture of the low temperature phase of thiourea/chlorocyclo-hexane determined at 85 K. The structure is viewed along the tunnel axis.
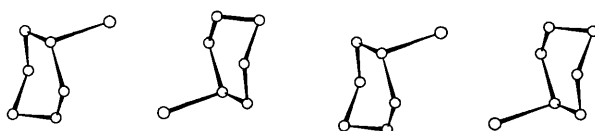


**Figure 4.9:** Guest substructure in the refined crystal structure of the thiourea/chlorocyclohexane inclusion compound at 85 K, viewed perpendicular to the tunnel axis.

The host substructure (Figure 4.8) in the low temperature phase is clearly a distorted form of the host substructure in the high temperature phase (Figure 4.5), with no change in the hydrogen bonding connectivity.

Unlike the situation in the high temperature phase, the guest molecules have well defined positions in the low temperature phase (see Figures 4.5, 4.8 and 4.9). The geometry of the cyclohexane ring is distorted from the standard chair conformation and may be better described as a distorted envelope

conformation (the carbon atom $(C(4))$ bonded to chlorine lies closer to the mean plane of the cyclohexane ring than expected for a chair conformation, see Figure 4.10).
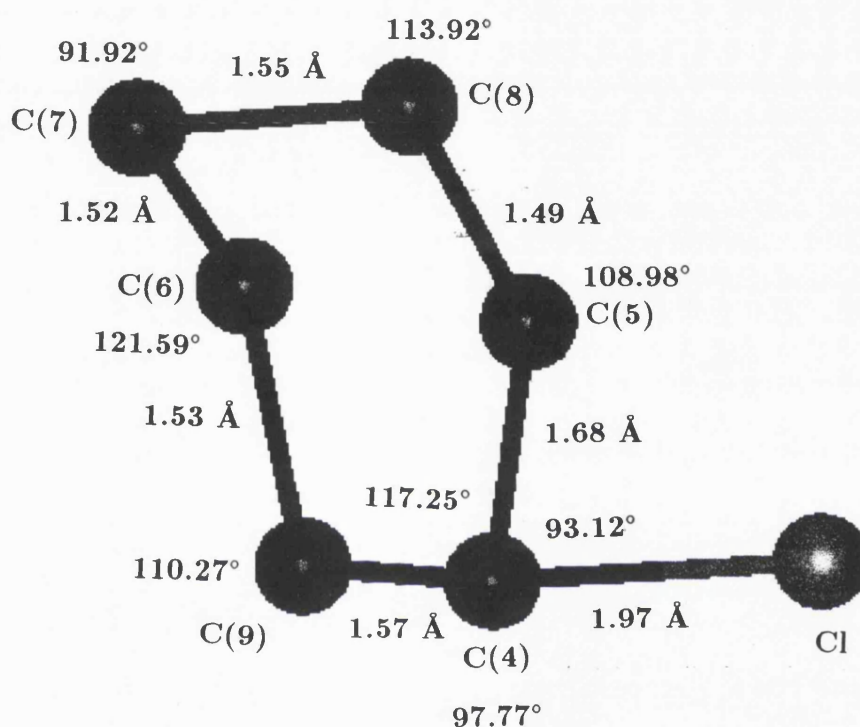


**Figure 4.10:** Geometry of chlorocyclohexane determined from the X–ray powder diffractogram at 85 K.

The chlorine atom is assigned unambiguously to the axial orientation with respect to the cyclohexane ring, providing direct structural evidence in support of conclusions reached previously by spectroscopic investigations [74, 75]. The geometry of the chlorocyclohexane molecule in the final refined structure is specified in Figure 4.10. Although some bond lengths and angles deviate significantly from standard values, the majority lie acceptably close to standard values.

An accurate determination of the geometry of the guest molecules is not expected from these Rietveld refinement calculations. One reason for this is the fact that, from high-resolution solid state $^{13}C$ NMR studies [74], it is

known that a small proportion ($\leq 10\%$) of the guest molecules exist in the equatorial conformation in the low temperature phase. It was not considered justified to include this conformational disorder within the structural models considered here. Nevertheless, the fact that this disorder exists in the actual structure, but has been omitted from the structural models used in the refinement calculations, will undoubtedly deteriorate the quality of the refined structure.

The orientation of the chlorocyclohexane guest molecule is such that the C(4)–Cl vector forms an angle of *ca.* 66° with respect to the tunnel axis. Within a given tunnel, adjacent guest molecules have opposite orientations with respect to the tunnel axis, giving rise to an ordered arrangement with two guest molecules in the periodic repeat distance along the tunnel and an alternation of head–head and tail–tail interactions between adjacent guest molecules. The intermolecular chlorine–chlorine distance between adjacent guest molecules (related by head–head interaction) is 4.6 Å. The isotropic atomic displacement parameter for the chlorine atom is significantly higher than for any other atom in the structure. This could possibly be related to the conformational disorder mentioned above, although no definite physical conclusions will be drawn here.

The difference Fourier map calculated for the final refined structure has three peaks with magnitude $\geq 1e\text{Å}^{-3}$, reflecting slight discrepancies between the refined structure and the experimental data. Two of these peaks are close to the sulfur and carbon atoms of the thiourea molecule and can be attributed to the fact that anisotropic atomic displacement parameters were not used. The other peak with magnitude $\geq 1e\text{Å}^{-3}$ in the difference Fourier map is similarly located close to the chlorine atom of the guest molecule. It is relevant to recall that hydrogen atoms were not included in the structural model, and their absence from the structural model could therefore, in principle, give rise to peaks at appropriate positions in the difference Fourier map.

The structural properties determined in the Rietveld refinement from the X-ray powder diffractogram recorded at 185 K are very similar to those determined at 85 K, with a similar conformation and mode of ordering of the guest molecules. The intermolecular chlorine–chlorine distance between adjacent guest molecules is 4.5 Å at 185 K. The final refined structural parameters at 185 K are reported in Table 4.6, and the experimental and calculated X–ray powder diffractograms are compared in Figure 4.11.

**Table 4.6:** Refined structural parameters for the low temperature phase of thiourea/chlorocyclohexane at 185 K. (space group $P2_1/a$; a = 9.6511(3) Å, b = 15.9636(4) Å, c = 12.4784(4) Å, $\beta$ = 114.22°). Goodness–of–fit indices are: $R_p$ = 0.134, $R_{wp}$ = 0.190.

| atom | x/a | y/b | z/c | $U_{iso}/Å^2$ |
|------|-----|-----|-----|---------------|
| host |  |  |  |  |
| S(1) | 0.538(1) | 0.1986(8) | 0.773(1) | 0.041(2) |
| S(2) | 0.481(1) | 0.1424(8) | 0.416(1) | 0.041(2) |
| S(3) | 0.578(1) | 0.1485(8) | 0.111(1) | 0.041(2) |
| C(1) | 0.507(5) | 0.088(1) | 0.765(3) | 0.049(9) |
| C(2) | 0.659(3) | 0.163(2) | 0.456(3) | 0.049(9) |
| C(3) | 0.395(3) | 0.198(2) | 0.052(3) | 0.049(9) |
| N(1) | 0.521(3) | 0.043(2) | 0.859(3) | 0.029(4) |
| N(2) | 0.692(3) | 0.228(2) | 0.567(3) | 0.029(4) |
| N(3) | 0.332(3) | 0.218(2) | 0.130(3) | 0.029(4) |
| N(4) | 0.375(3) | 0.247(2) | 0.952(2) | 0.029(4) |
| N(5) | 0.479(3) | 0.043(2) | 0.668(3) | 0.029(4) |
| N(6) | 0.728(3) | 0.206(2) | 0.387(3) | 0.029(4) |
| guest |  |  |  |  |
| Cl | 0.115(2) | 0.051(1) | 0.894(2) | 0.36(1) |
| C(4) | 0.921(3) | 0.046(2) | 0.767(3) | 0.104(9) |
| C(5) | 0.099(4) | 0.048(3) | 0.200(4) | 0.104(9) |
| C(6) | 0.916(4) | 0.013(3) | 0.338(4) | 0.104(9) |
| C(7) | 0.058(4) | 0.077(2) | 0.395(3) | 0.104(9) |
| C(8) | 0.050(5) | 0.104(2) | 0.279(4) | 0.104(9) |
| C(9) | 0.015(5) | 0.068(2) | 0.687(4) | 0.104(9) |
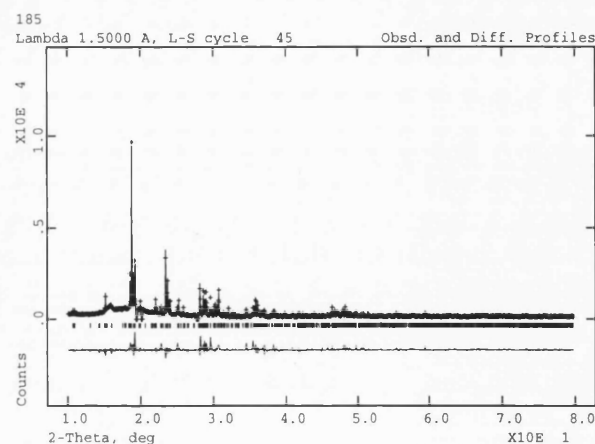
**Figure 4.11:** Comparison of the experimental diffractogram of thiourea/chlorocyclohexane inclusion compound at 185 K to the calculated diffractogram. The crosses represent the experimental data and the full line is the calculated diffractogram. Beneath the difference diffractogram is shown.

## 4.5 Conclusions

With this experiment, it has been demonstrated that X–ray powder diffraction combined with Rietveld refinement calculations is a viable method for following structural changes across low temperature phase transitions in complex systems. Although in the high temperature phase of the thiourea/chlorocyclohexane inclusion compound the guest molecules are substantially disordered [52, 74], a satisfactory refinement of the diffraction profile was obtained. The resulting structure was in good agreement with a previous experiment employing single crystal X–ray diffraction [52].

The structure of the low temperature phase of the inclusion compound was determined for the first time. The metric symmetry is monoclinic and the space group of the structure is $P2_1/a$. The host substructure is similar to that found in the high temperature phase, the tunnels being distorted

from the ideal hexagonal shape found in the high temperature phase (see Figure 4.8). In addition, the guest molecules are localized within the tunnels of the host substructure. The guest molecular structure determined here, though far from ideal, supports previous observations *via* NMR and IR spectroscopy with respect to the preference for the axial conformer [74, 75]. The guest molecular structure also shows the limitations of the method. It is entirely possible that the distortion of the cyclohexane ring is a manifestation of the equilibrium distribution of the axial and equatorial conformers that are present in the inclusion compound, though in substantially different proportions. However, the data quality was not deemed sufficient to incorporate a more sophisticated model of the guest substructure than that presented above. The guest molecules adopt a head–head/tail–tail ordering, with an intermolecular chlorine–chlorine distance of 4.6 Å at 85 K. This correlates well with results from EXAFS experiments on the thiourea/bromocyclohexane system [54], where the bromocyclohexane guest molecules were found to adopt a similar head–head/tail–tail ordering with a intermolecular bromine distance of 3.82 Å.

Although a low temperature, monoclinic phase of a thiourea inclusion compound has been previously investigated employing single crystal X–ray diffraction ([91], the guest was 1,5–cyclooctadiene, an ambient temperature structure has not been reported), previous attempts to investigate phase transitions using this technique [77, 86] have not been successful. X–ray powder diffraction avoids the problems associated with crystal twinning, which often accompanies high symmetry to low symmetry phase transitions.

# Chapter 5

# Molecular Dynamics of Tetrakis(trimethylsilyl)silane in the Solid State

## Abstract

Incoherent quasielastic neutron scattering (IQNS) spectroscopy has been used to investigate the dynamic properties of solid tetrakis(trimethylsilyl)silane ($Si[Si(CH_3)_3]_4$, TTMSS). This material is known to undergo a phase transition to a plastic crystal phase at *ca.* 240 K. The evolution of the elastic intensity as a function of temperature between 4.5 K and 300 K indicates three distinct dynamic regimes, with changes in dynamic behaviour at 120 K and 240 K. Detailed consideration of quasielastic broadening in the IQNS spectra (including consideration of the effects of multiple scattering) has established the following information on the dynamic processes occurring on the experimental timescale within each of these regimes. Below 120 K, there are only molecular vibrational motions with no quasielastic broadening in the IQNS spectra. Between 120 K and 240 K, the dynamic properties are interpreted as 3–fold jumps of the $CH_3$ group about the Si–$CH_3$ bond. Above 240 K, two different dynamic models

have been considered: (a) combined 3-fold jumps of the $CH_3$ group about the Si–$CH_3$ bond and 3-fold jumps of the $Si(CH_3)_3$ group about the Si–$Si(CH_3)_3$ bond; (b) isotropic reorientational diffusion. Model (a) fails to fit the IQNS spectra, whereas model (b) provides an acceptable fit to the IQNS spectra in the temperature range investigated (245 K – 300 K) for the high-temperature phase. The isotropic reorientational diffusion is considerably slower than the 3-fold jumps of the $CH_3$ group about the Si–$CH_3$ bond.

## 5.1 Introduction

Solid tetrakis(trimethylsilyl)silane ($Si[Si(CH_3)_3]_4$; TTMSS; Figure 5.1) is known [92] to undergo a phase transition at $T_t \sim 238$ K – 241 K. Above this temperature the material behaves as a plastic crystal (see Chapter 1). Recently, temperature dependent high–resolution solid state $^{13}C$ and $^{29}Si$ NMR spectroscopic investigations of TTMSS have been reported [74], and have provided new insights into the dynamic properties of this material. First, the results from these studies will be summarized. The phases above and below the phase transition temperature $T_t$ will hereafter be referred to as the high temperature (HT) phase and the low temperature (LT) phase respectively.

In the HT phase, the high–resolution solid state $^{13}C$ NMR spectrum contains a single narrow peak, implying that all $CH_3$ carbons are equivalent on the $^{13}C$ NMR timescale. This can be interpreted on the basis of rapid molecular motion (rapid with respect to the $^{13}C$ NMR timescale) allowing all $^{13}C$ nuclei to experience the same average environment on the timescale of the measurement. Rapid isotropic motion of each molecule about a fixed centre of mass is consistent with this observation. On lowering the temperature below 233 K, the $^{13}C$ NMR spectrum changes from one peak to two peaks with 3:1 intensity ratio. On further decreasing the temperature, the spectrum develops into a set of three peaks with 1:2:1 intensity ratio at 182 K and into four peaks
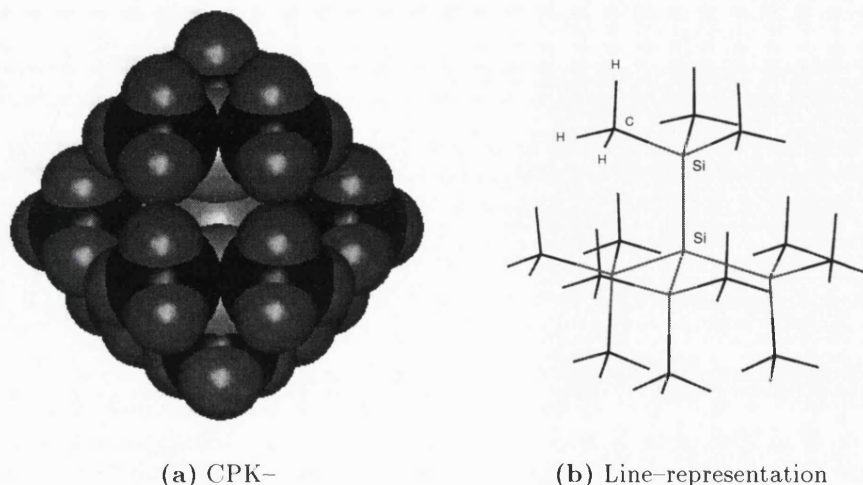
with 1:1:1:1 intensity ratio below 172 K.



(a) CPK–                                  (b) Line–representation

**Figure 5.1:** Molecular structure of a single molecule of tetrakis(trimethyl-silyl)silane. The globular nature of the molecule is particularly clear in the CPK–representation to the left. The line–drawing to the right shows the bonding within the molecule.

The high–resolution solid state $^{29}$Si NMR results are in good agreement with the observations from $^{13}$C NMR. Specifically, in the HT phase, the high–resolution solid state $^{29}$Si NMR spectrum contains a single peak for the $Si(CH_3)_3$ groups and a single peak for the central silicon atom. On entering the LT phase, the signal due to the $Si(CH_3)_3$ groups becomes two peaks with 3:1 intensity ratio.

Based on these $^{13}$C and $^{29}$Si NMR results, the following types of motion were proposed [74] for the LT phase of TTMSS:

**A**: Rotation of the whole molecule about a fixed axis coincident with one of the Si–Si bonds and

**B:** Rotation of each $Si(CH_3)_3$ group about the relevant $Si-Si(CH_3)_3$ bond.

Rotation of each $CH_3$ group about the relevant $Si-CH_3$ bond was assumed to be rapid on the experimental timescale at all temperatures studied.

The generation of two peaks with 3:1 intensity ratio in the $^{13}C$ and $^{29}Si$ NMR spectra upon entering the LT phase suggests that one $Si(CH_3)_3$ group (denoted type [a]) becomes crystallographically inequivalent from the other three $Si(CH_3)_3$ groups (denoted type [b]). Thus, although the crystal structure of TTMSS in the LT phase is not yet known, the $^{13}C$ and $^{29}Si$ NMR results suggest that the TTMSS molecule may lie on a crystallographic 3–fold symmetry axis which is coincident (on average) with the Si[c]–Si[a] bond (where Si[c] denotes the central Si atom). In terms of the dynamic properties, it is clear that rapid type **B** rotation of the type [b] $Si(CH_3)_3$ groups is required in order for all nine $CH_3$ carbons of the type [b] $Si(CH_3)_3$ groups to become equivalent. The spectral changes occurring from *ca.* 208 K to 152 K can be understood completely in terms of type **B** rotation of the type [b] $Si(CH_3)_3$ groups becoming progressively hindered with decreasing temperature. It is possible that the molecule may be rotating about the axis coincident with the Si[c]-Si[a] bond in the LT phase. However, although the occurrence of this motion is consistent with the available evidence, interpretation of the $^{13}C$ NMR spectra does not require that there is rapid motion of this type in the LT phase.

Solid state $^2H$ NMR studies of a natural abundance sample of TTMSS have also been reported [93, 94]. The $^2H$ NMR spectrum of the high temperature phase comprises a single narrow line (with a linewidth of *ca.* 1 kHz), and is consistent with rapid isotropic reorientation of the TTMSS molecules. However, a dynamic model comprising rapid 4–site, 90° jumps about the 2–fold axes of the tetrahedron formed by the silicon atoms of the $Si(CH_3)_3$ groups, together with rapid rotation of the $Si(CH_3)_3$ groups about the $Si-Si(CH_3)_3$ bonds and rapid rotation of the $CH_3$ groups about the $Si-CH_3$ bonds, is also

consistent with this observation. Thus, these different dynamic models for the HT phase cannot be distinguished on the basis of the $^2$H NMR results alone.

Clearly the solid state NMR results described above have provided interesting insights into the dynamic properties of solid TTMSS, although several aspects remain to be understood in more depth.

In this chapter, the application of incoherent quasielastic neutron scattering (IQNS) spectroscopy to extend our understanding of the dynamic behaviour of solid TTMSS is described. In this regard, it is important to emphasize the complementarity between IQNS spectroscopy and the solid state NMR techniques described above, in terms of the contrasting characteristic timescales of these techniques. It is also relevant to recall that incoherent neutron scattering for TTMSS is dominated by scattering from the $^1$H nuclei (see Section 2.3).

## 5.2 Experimental

TTMSS was obtained commercially and used as purchased. Since TTMSS is hygroscopic, the sample was ground to a fine powder in a glove box under a dry atmosphere. The sample was loaded into the sample container inside the glove box.

IQNS spectra were recorded on the backscattering spectrometer IRIS at the ISIS neutron spallation source (Rutherford Appleton Laboratory, Didcot, England). The instrumental resolution was approximately 15 $\mu$eV (full width at half maximum height), the neutron wavelength was $\lambda_0 = 6.6$ Å, using the graphite analysers PG(002). The corresponding experimental timescale is of the order of $\tau \leq 500 \times 10^{-12} s$.

Spectra were recorded with the polycrystalline sample of TTMSS in a square, flat–plate aluminium container, the plane of which was oriented at 150° with respect to the incident neutron beam (Figure 5.2).
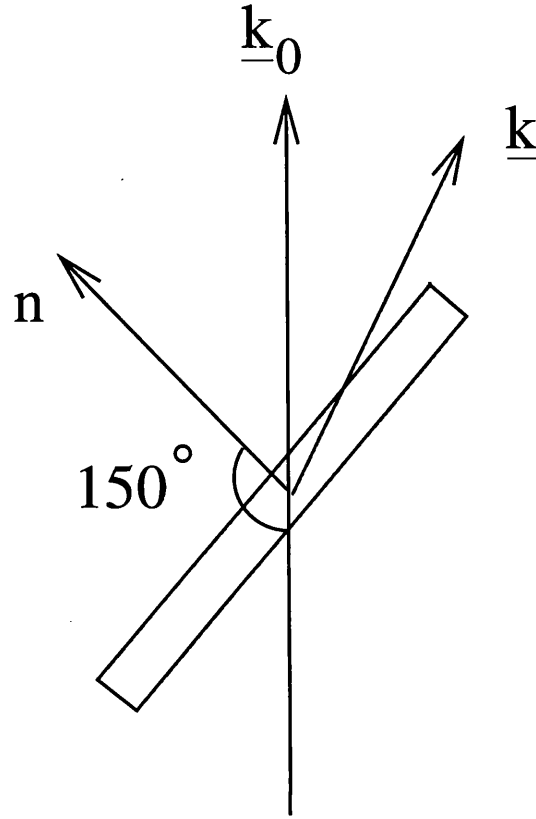
**Figure 5.2:** Schematic illustration of the experimental scattering geometry.

Initially, an elastic scan was performed to provide qualitative insights into the temperature dependence of the dynamics of TTMSS. Spectra were recorded (duration 15 mins) at 4.5 K, 50 K, 70 K, 90 K, and thereafter from 100 K to 300 K in steps of 5 K. Incoherent quasielastic neutron scattering spectra were then recorded at several temperatures above and below $T_t$. The detectors were normalized using the spectrum of a vanadium standard with the same dimensions as the sample of TTMSS, and the IQNS spectrum of TTMSS recorded at 4.5 K was used to determine the instrumental lineshape. Data reduction was performed using the standard ISIS programs ICON and ACORN within the IRIS Data Analysis Package. ACORN subtracts the scattering due to the sample container and carries out absorption corrections, whereas ICON normalizes the data to the incident neutron flux. Fitting of theoretical models to the experimental data was carried out using standard least squares

fitting programs [95] which were modified to account for the energy dependent background (arising from contamination by the PG(004) analyser reflection). Theoretical scattering functions corrected for multiple scattering were calculated using a modified version of the program MUSCADE [96].

## 5.3  Qualitative Analysis of Results

In the first stage of the analysis, the evolution of the elastic intensity as a function of temperature was assessed from an elastic scan. The plot of the elastic intensity versus temperature (Figure 5.3) shows three distinct dynamic regimes for TTMSS in the temperature range 4.5 K - 300 K. Below 120 K, the decrease of the elastic intensity with increasing temperature arises from the molecular vibrational motions (i.e. the Debye-Waller term, Equation 2.45); no quasielastic broadening is evident in the quasielastic profiles recorded in this temperature range. Between 120 K and 240 K, the elastic intensity decreases more rapidly with increasing temperature, and quasielastic broadening is evident in the quasielastic profiles, corresponding to the onset of large amplitude reorientational motion of TTMSS. At 240 K, there is a sharp decrease in the elastic intensity, consistent with the occurrence of a solid state phase transition involving a new reorientational process of TTMSS. This result is in good agreement with the phase transition temperature reported previously [74, 92] for TTMSS.

In the HT phase above 240 K, the elastic intensity is small (in the experimental Q range) indicating the onset of very large amplitude reorientational motions of the TTMSS molecules.
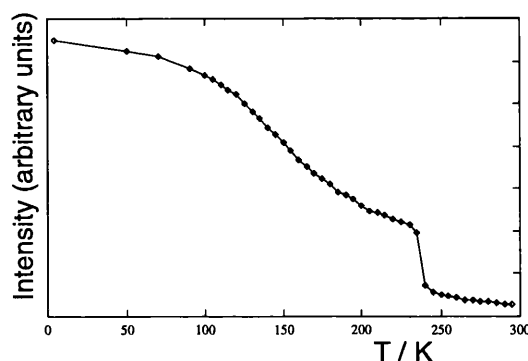
**Figure 5.3:** Plot of the elastic intensity as a function of temperature. The three different dynamic regimes are clearly visible. The first dynamic regime extends up to *ca.* 120 K and is associated with vibrational motion. Above that the slope of the curve changes indicating the onset of reorientational motion. The phase transition at 240 K is accompanied by a steep decrease of the elastic intensity.

For the LT phase, the EISF is independent of temperature and tends towards $\frac{1}{3}$ at large Q. For the HT phase, the EISF suggests that there is additional large amplitude reorientational motion of TTMSS. More detailed discussions of the EISFs and the quasielastic profiles for the LT phase and the HT phase are given in Section 5.5.

# 5.4   Dynamic Models for Solid TTMSS

On the basis of the above observations, different types of motion are considered, which are effective on the IQNS timescale for the $^{1}$H nuclei of the TTMSS molecule in different temperature regimes. The following dynamic models have been considered in this regard.

**Model I:** 3–fold jumps of the $CH_3$ group about the $Si–CH_3$ bond.

For a polycrystalline sample, the scattering law for 3–fold jumps of the $CH_3$ group about the $Si–CH_3$ bond [44] is given by Equation 2.46 with $N = 1$ and

the structure factors

$$A_0(Q) = \frac{1}{3}(1 + 2j_0(Qr))$$
$$A_1(Q) = \frac{2}{3}(1 - j_0(Qr))$$

(5.1)

where r represents the jump distance for the $^1$H nuclei of the $CH_3$ group and $j_0(Qr)$ is the spherical Bessel function of zero order. The width (half width at half maximum, HWHM) $\Delta_1$ of the Lorentzian function $\mathcal{L}(\omega)$ is:

$$\Delta_1 = \frac{3}{2\tau(\text{Si--C})}$$

(5.2)

where $\tau(\text{Si--C})$ represents the correlation time for the 3–fold jump motion of the $CH_3$ group about the $Si-CH_3$ bond. For this dynamic model, the EISF is independent of temperature and tends towards $\frac{1}{3}$ for sufficiently large Q. As this model requires only one Lorentzian function, the scattering functions for second order and third order scattering (Equations 2.52 and 2.54) involve Lorentzian functions with widths $2\Delta_1$ and $3\Delta_1$ respectively.

**Model II**: Combined 3–fold jumps of the $CH_3$ group about the $Si-CH_3$ bond and 3–fold jumps of the $Si(CH_3)_3$ group about the $Si-Si(CH_3)_3$ bond.

3–fold jump motion of the $CH_3$ group about the $Si-CH_3$ bond combined with a 3–fold jump motion of the $Si(CH_3)_3$ group about the $Si-Si(CH_3)_3$ bond is considered next. In the case of a polycrystalline sample, the scattering law [44] for this dynamic model is given by Equation 2.46 with N = 3 and the following

structure factors:

$$A_0(Q) = \frac{1}{27}(3 + 6j_0(Qr_2) + 2j_0(Qr_3) + 4j_0(Qr_4) + 4j_0(Qr)5)$$

$$+ 2j_0(Qr_6) + 2j_0(Qr_7) + 4j_0(Qr_8)$$

$$A_1(Q) = \frac{1}{27}(6 - 6j_0(Qr_2) + 4j_0(Qr_3) - 4j_0(Qr_4) - 4j_0(Qr_5)$$

$$- 2j_0(Qr_6) - 2j_0(Qr_7) + 8j_0(Qr_8)$$

$$A_2(Q) = \frac{1}{27}(6 + 12j_0(Qr_2) - 2j_0(Qr_3) - 4j_0(Qr_4) - 4j_0(Qr_5) \qquad (5.3)$$

$$- 2j_0(Qr_6) - 2j_0(Qr_7) - 4j_0(Qr_8)$$

$$A_3(Q) = \frac{1}{27}(12 - 12j_0(Qr_2) - 4j_0(Qr_3) + 4j_0(Qr_4) + 4j_0(Qr_5)$$

$$+ 2j_0(Qr_6) + 2j_0(Qr_7) - 8j_0(Qr_8)$$

where $r_i$ (i = 2, 3, ..., 8) represent jump distances relevant to this model (*vide infra*). The widths (HWHM) $\Delta_i$ of the three Lorentzian functions $\mathcal{L}_i(\omega)$ for this model are:

$$\Delta_1 = \frac{3}{2\tau(\text{Si–C})}$$

$$\Delta_2 = \frac{3}{2\tau(\text{Si–Si})} \qquad (5.4)$$

$$\Delta_3 = \Delta_1 + \Delta_2$$

where $\tau(\text{Si–C})$ represents the correlation time for the 3–fold jump motion of the $CH_3$ group about the $Si–CH_3$ bond and $\tau(\text{Si–Si})$ represents the correlation time for the 3–fold jump motion of the $Si(CH_3)_3$ group about the $Si–Si(CH_3)_3$ bond.

**Model III**: Isotropic reorientational diffusion.

The scattering law for isotropic reorientational diffusion of the whole molecule

is given [97] by Equation 2.46 with $N = \infty$ and the following structure factors:

$$A_0(Q) = [j_0(Qr)]^2$$
$$A_i(Q) = (2i + 1)[j_i(Qr)]^2 \tag{5.5}$$

where r is the radius of the sphere on which the $^1$H nucleus is considered to diffuse and $j_i$ is the spherical Bessel function of $i^{th}$ order. The widths (HWHM) $\Delta_i$ of the Lorentzian functions $\mathcal{L}_i(\omega)$ are given by:

$$\Delta_i = i(i + 1)D_R \tag{5.6}$$

where $D_R$ is the isotropic rotational diffusion coefficient.

## 5.5 Results and Discussion

First the dynamic properties of the LT phase are discussed, for which the EISF tends towards $\frac{1}{3}$ at high $Q$ and is independent of temperature (Figure 5.4). The qualitative observations discussed in Section 5.3 suggest that a dynamic model comprising 3–fold jumps of the $CH_3$ group about the Si–$CH_3$ bond (i.e. Model I) is appropriate for the LT phase. However, comparison between the theoretical EISF derived for this model (from Equation 5.1 with a jump distance r = 1.73 Å) and the experimental EISF shown in Figure 5.4 indicates that it is necessary to consider multiple scattering. The theoretical EISF, corrected for multiple scattering (Equation 2.56), is also shown in Figure 5.4, and is in good agreement with the experimental EISF. In correcting the theoretical EISF for multiple scattering, the effective scattering cross-section per unit volume was determined using the powder density calculated from the mass of the sample divided by the volume of the sample container.
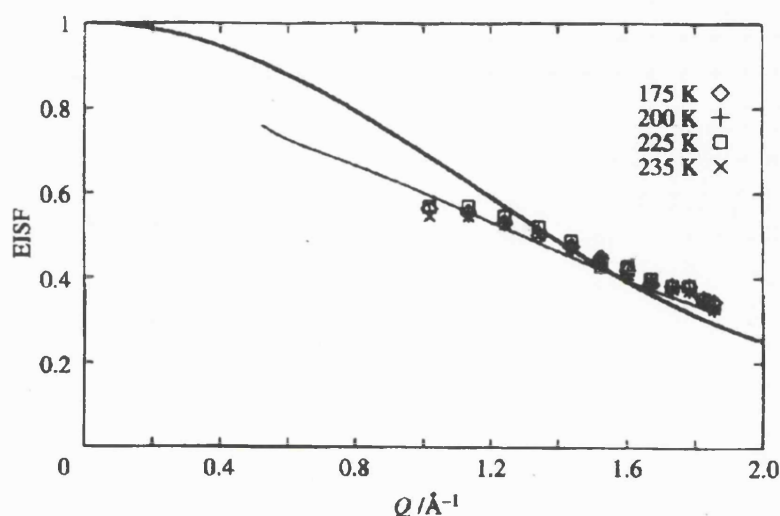
**Figure 5.4:** Experimental EISF for the spectra recorded below the phase transition temperature $T_t$ (temperatures are indicated in the legend). The thin line represents the theoretical EISF for three fold jump rotation corrected for multiple scattering, the thick line represents the same model without corrections for multiple scattering.

Initially, Model I was fitted (Figure 5.5) to the experimental IQNS profiles (all scattering angles considered simultaneously), with only the structure factors corrected for multiple scattering. The best fit parameters are given in Table 5.1. The effective gyration radius obtained from fitting the model to the experimental spectra is $r_g = r/(2cos(30°)) = 1.0$ Å, in good agreement with the expected gyration radius for the $^1$H nuclei of a $CH_3$ group reorienting about the Si–$CH_3$ bond. The full multiple scattering correction was considered for the spectrum recorded at $Q = 1.6$ Å$^{-1}$, and the results are reported in Table 1. The correlation time ($\tau^*$(Si–C)) derived from this fit is larger by about 5 % than the correlation time ($\tau$(Si–C)) determined taking into account only the effects of multiple scattering on the structure factors. On the basis of these results, it is clear that the 3–fold jump motion of the $CH_3$ group about the Si–$CH_3$ bond is the only motion occurring on the experimental timescale ($\tau \leq 500 \times 10^{-12}s$) in the LT phase.

(a) $Q = 1.13$ Å$^{-1}$

(b) $Q = 1.34$ Å$^{-1}$

(c) $Q = 1.53$ Å$^{-1}$

(d) $Q = 1.67$ Å$^{-1}$
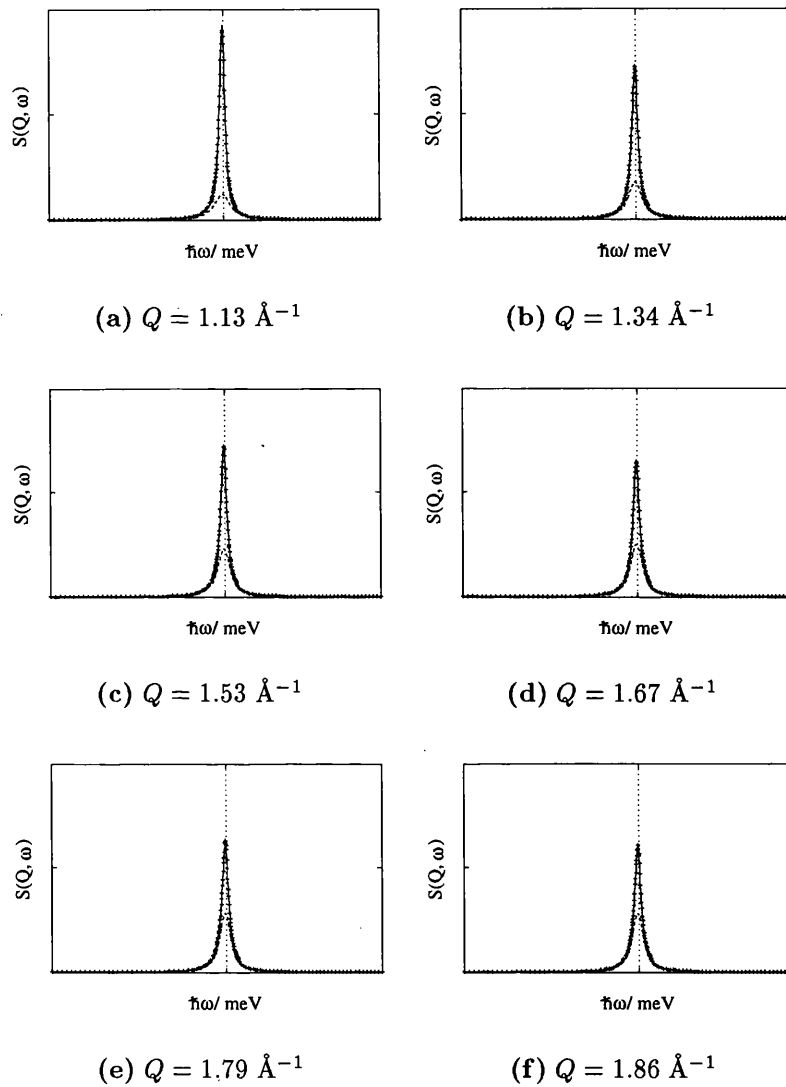
(e) $Q = 1.79$ Å$^{-1}$

(f) $Q = 1.86$ Å$^{-1}$

**Figure 5.5:** Comparison between the experimental IQNS spectra (points) and the fitted spectra (solid line) assuming Model I for the low temperature phase at 175 K. The dashed line represent the quasielastic contribution.

**Table 5.1:** Parameters obtained from fitting Model I to the IQNS data obtained in the low temperature phase. Structure factors are corrected for multiple scattering. The values $\tau^*(Si-C)$ are those obtained by fitting the spectrum at $Q = 1.6$ Å$^{-1}$ using the full multiple scattering correction.

| T / K | $\Delta_1$ / meV | $\tau(Si-C)$ / s | $\tau^*(Si-C)$ / s | $r_g$ / Å | $< u^2 >$ / Å$^2$ |
|---|---|---|---|---|---|
| 175 | $1.29 \times 10^{-2}$ | $76.4 \times 10^{-12}$ | $81.3 \times 10^{-12}$ | 1.03 | $3.14 \times 10^{-2}$ |
| 200 | $2.85 \times 10^{-2}$ | $34.6 \times 10^{-12}$ | $36.8 \times 10^{-12}$ | 1.02 | $3.31 \times 10^{-2}$ |
| 225 | $4.73 \times 10^{-2}$ | $20.8 \times 10^{-12}$ | $22.1 \times 10^{-12}$ | 0.99 | $3.78 \times 10^{-2}$ |
| 235 | $5.21 \times 10^{-2}$ | $18.9 \times 10^{-12}$ | $20.0 \times 10^{-12}$ | 1.00 | $4.39 \times 10^{-2}$ |

Assuming Arrhenius behaviour for the temperature dependence of $\tau(Si-C)$, i.e.

$$\tau(Si-C) = \tau_0(Si-C) \exp\left(E_a/RT\right) \qquad (5.7)$$

(Figure 5.6) the activation energy found is $E_a = 8.07$ kJ mol$^{-1}$ and correlation time $\tau_0$ is $\tau_0(Si-C) = 0.29 \times 10^{-12}$ s. The corresponding parameters determined on the assumption of Arrhenius behaviour for the temperature dependence of $\tau^*(Si-C)$ are: $E_a^* = 8.07$ kJ mol$^{-1}$; $\tau_0^*(Si-C) = 0.31 \times 10^{-12}$ s.
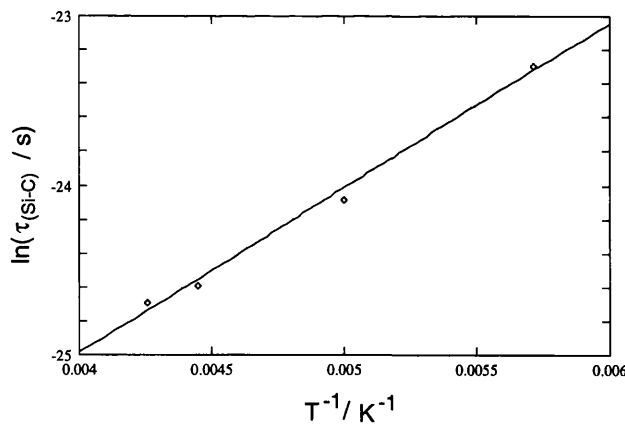


**Figure 5.6:** Plot of $\tau$ versus $1/T$. The (symbols) denote the experimental values, the line shows the fit to the data.

For the HT phase Models II and III were considered. For Model II, the width $\Delta_1$ of the Lorentzian function representing reorientation of the $CH_3$ group about the Si–$CH_3$ bond was fixed by extrapolation from the data for the LT phase. This assumes that there is no discontinuity in the methyl group dynamics on crossing the phase transition. Model II requires seven jump distances $r_i$, which were determined from an idealised geometry of the TTMSS molecule (with standard bond lengths and tetrahedral bond angles).
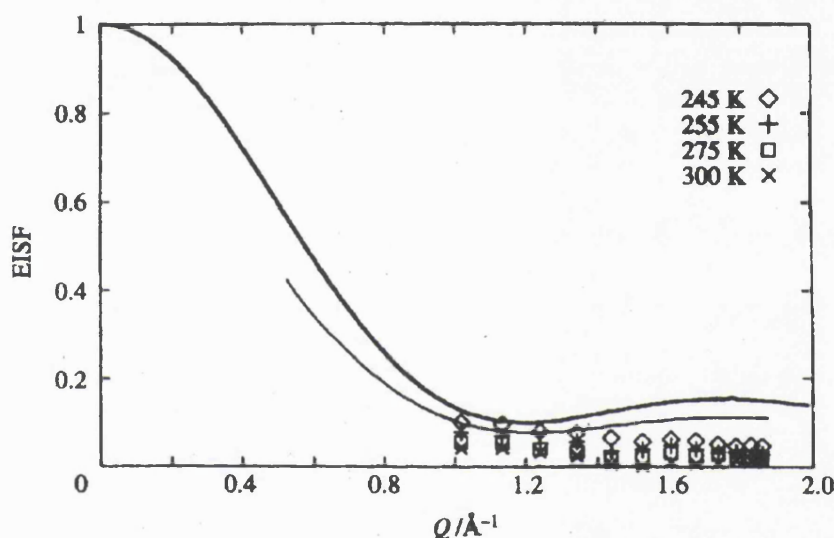


**Figure 5.7:** Experimental EISF extracted for the spectra recorded above the phase transition (temperatures are given in the legend). The thick full line represents the theoretical EISF for Model II, the thin full line represents the same model corrected for multiple scattering.

By fixing the bond angles at their ideal values, the only length parameter is the Si...H distance (for the Si atom of the $Si(CH_3)_3$ group), denoted $r_{Si-H}$. This represents a simplified approach in which the molecular geometry is severely constrained. Using $r_{Si-H} = 2.45$ Å for the Si...H distance in the idealised molecular geometry, satisfactory fits are not obtained for the EISF, even when the effects of multiple scattering are taken into account (Figure 5.7). Comparing the theoretical EISF and the experimental EISF (Figure 5.7), a clear temperature dependence is evident, with the experimental EISF gener-

ally lower than the theoretical EISF. The quasielastic profiles (Figure 5.8) are also not fitted satisfactorily using Model II with $r_{Si-H} = 2.45$ Å. In addition, attempts to refine $r_{Si-H}$ did not give good fits to the quasielastic profiles (leading to values of $r_{Si-H}$ ranging from 1.5 Å to 2.7 Å). In conclusion, Model II cannot fit the experimental data satisfactorily.



(a) $Q = 1.13$ Å$^{-1}$        (b) $Q = 1.34$ Å$^{-1}$

(c) $Q = 1.53$ Å$^{-1}$        (d) $Q = 1.67$ Å$^{-1}$

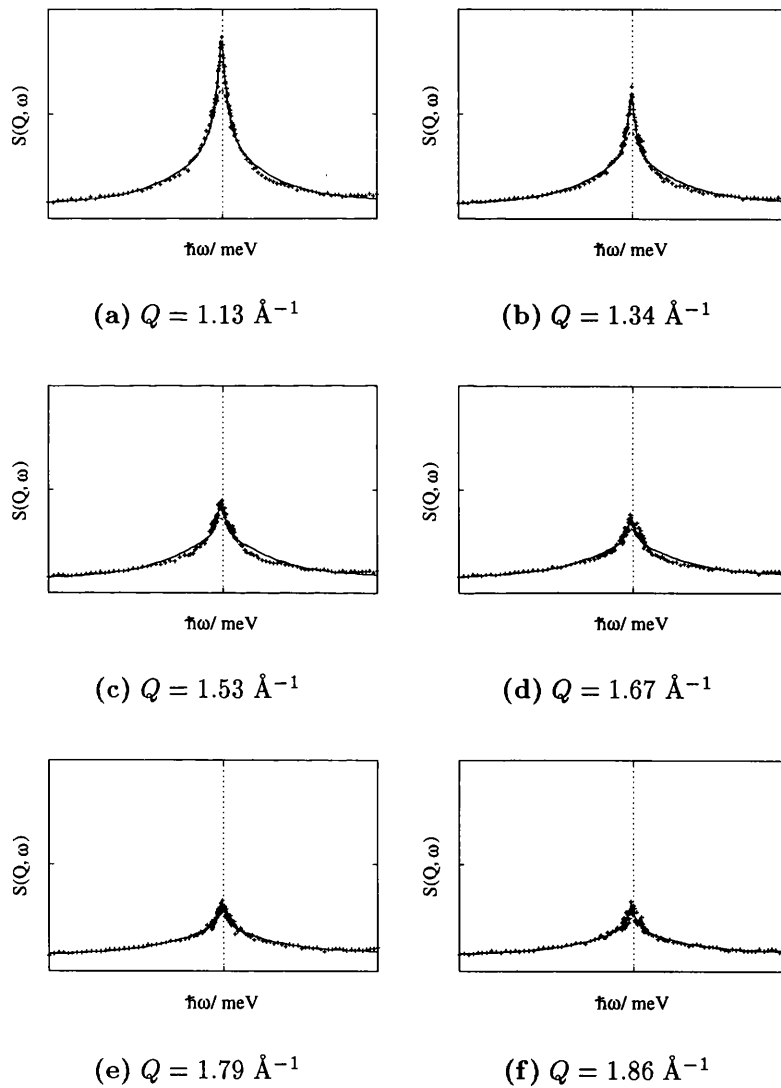(e) $Q = 1.79$ Å$^{-1}$        (f) $Q = 1.86$ Å$^{-1}$

**Figure 5.8:** Comparison between the experimental IQNS spectra (points) and the fitted spectra (solid line) assuming Model II for the low temperature phase at 300 K. The dashed line represents the quasielastic contribution.

Model III (isotropic reorientational diffusion of the $^1$H nuclei on the surface of a sphere) yields improved results. The infinite sum in Equation 2.46 was truncated after i = 12, since higher terms have no significant effect in the observed Q range. At the highest temperature considered (300 K), the experimental EISF and the theoretical EISF are in good agreement for this model (Figure 5.9). At lower temperatures in the HT phase, the experimental EISF curve follows the same shape as the theoretical EISF curve, but the experimental EISF curve lies higher by an amount that increases with decreasing temperature. This behaviour could be consistent with either of the following explanations: (a) the motion is not completely isotropic on the experimental timescale at these temperatures, with the degree of anisotropy decreasing (i.e. the model of isotropic reorientational diffusion becoming a better description of the dynamics) as the temperature is increased; (b) the larger widths at higher temperature allow a more reliable estimate of the EISF. At all temperatures considered in the HT phase, the experimental quasielastic profiles can be fitted well using Model III, with only the structure factors corrected for multiple scattering and taking the idealised value r = 4.5 Å for the radius of the sphere [1]. In carrying out these fits, only spectra in the Q range 1.53 Å$^{-1}$ – 1.87 Å$^{-1}$ were considered, as the spectra in this range are less affected by multiple scattering. Parameters relating to the fitting of Model III to the quasielastic profiles for the HT phase are given in Table 5.2, and the fitted spectra at 300 K are shown in Figure 5.10. From these fits, the rotational diffusion coefficient $D_R$ has been obtained as a function of temperature.

---

[1]The radius of the sphere of diffusion was determined from standard bondlengths assuming tetrahedral bond angles.
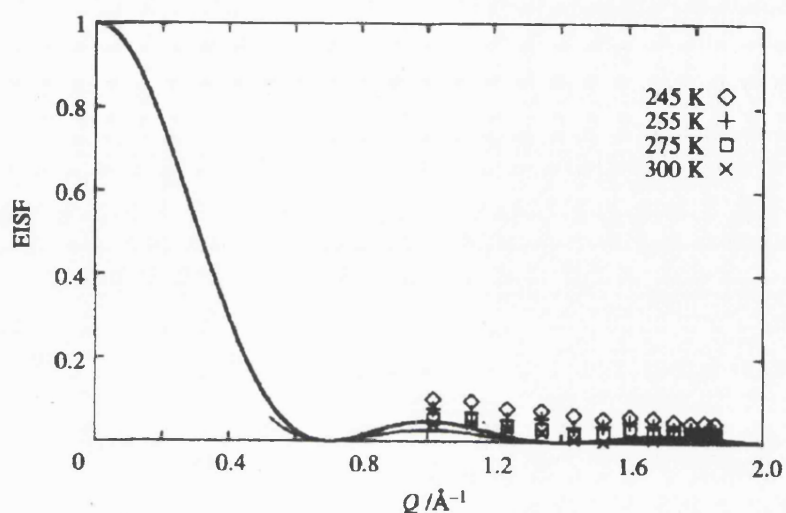
**Figure 5.9:** Experimental EISF extracted from the spectra recorded above the phase transition (symbols, the temperatures are indicated in the legend). The thick full line represents the theoretical EISF for Model III, the thin line represents the same model corrected for multiple scattering.

**Table 5.2:** Parameters obtained from fitting Model III to the IQNS spectra recorded for the high temperature phase.

| T / K | $\Delta_1$ / meV | $D_R$ / $s^{-1}$ |
|-------|------------------|------------------|
| 245 | $1.27 \times 10^{-3}$ | $0.96 \times 10^9$ |
| 255 | $1.55 \times 10^{-3}$ | $1.18 \times 10^9$ |
| 275 | $2.00 \times 10^{-3}$ | $1.52 \times 10^9$ |
| 300 | $2.54 \times 10^{-3}$ | $1.93 \times 10^9$ |

Assuming Arrhenius behaviour for the temperature–dependence of $D_R$,

$$D_R = D_0 \exp\left(-E_a/RT\right) \tag{5.8}$$

the following parameters are obtained: $E_a = 7.62$ kJ mol$^{-1}$; $D_0 = 4.17 \times 10^{10}$ s$^{-1}$. This isotropic reorientational diffusion is considerably slower than the 3–fold jumps of the $CH_3$ group about the Si–$CH_3$ bond.

(a) $Q = 1.13$ Å$^{-1}$

(b) $Q = 1.34$ Å$^{-1}$

(c) $Q = 1.53$ Å$^{-1}$

(d) $Q = 1.67$ Å$^{-1}$

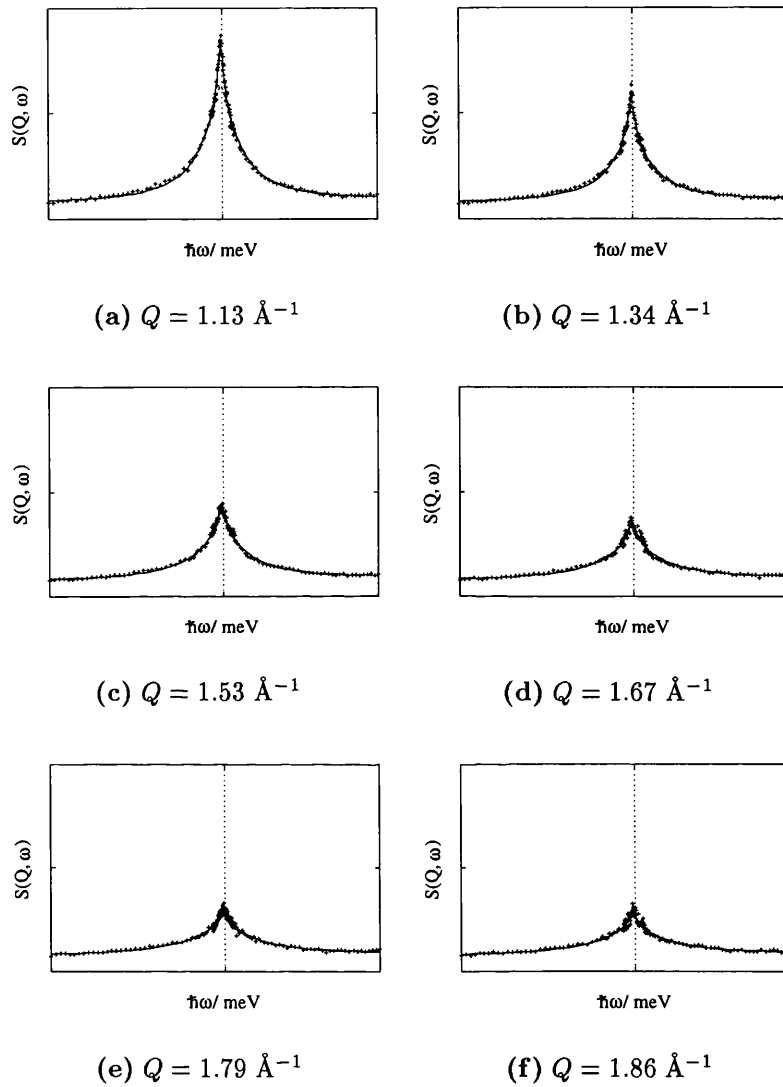(e) $Q = 1.79$ Å$^{-1}$

(f) $Q = 1.86$ Å$^{-1}$

**Figure 5.10:** Comparison between the experimental IQNS spectra (points) and the fitted spectra (solid line) assuming Model III for the low temperature phase at 300 K. The dashed line represents the quasielastic contribution.

## 5.6   Conclusions

It is interesting to compare the parameters ($E_a^* = 8.07$ kJ mol$^{-1}$; $\tau_0^*$(Si–C) = $0.31 \times 10^{-12}$ s) relating to the methyl group reorientation in TTMSS with those determined using the same technique for methyl group reorientation in other materials containing groups of the type X(CH$_3$)$_3$. It has been reported that $E_a = 10.6$ kJ mol$^{-1}$ and $\tau_0$(Si–C) = $1.05 \times 10^{-12}$ s for methyl group reorientation in trimethyloxosulphonium iodide (CH$_3$)$_3$SOI [98], and $E_a = 9.3$ kJ mol$^{-1}$ and $\tau_0$(C–C) = $2.6 \times 10^{-12}$ s for methyl group reorientation in pivalic acid (CH$_3$)$_3$CCO$_2$H [99] (assuming Arrhenius behaviour in both cases). The trend of increasing $\tau_0$ (i.e. slower reorientation) is in the order X = Si, S, C, which correlates qualitatively with the order of decreasing X–CH$_3$ bond distance [100]. Undoubtedly, several factors contribute to this observed trend, including the fact that the extent of interaction between the different CH$_3$ groups in the X(CH$_3$)$_3$ group will depend on the X–CH$_3$ bond distance. A more quantitative assessment of this issue would be possible if data on the methyl group reorientational dynamics in a series of materials closely related to TTMSS were available (*vide infra*).

As discussed in Section 5.1, the dynamic properties of TTMSS have been investigated previously by high-resolution solid state $^{13}$C and $^{29}$Si NMR (in both the LT and HT phases) and by wide–line solid state $^2$H NMR (at ambient temperature). The characteristic timescales of these techniques (typically $\tau \approx 10^{-3} - 10^{-1}$ s for lineshape analysis of high–resolution $^{13}$C NMR spectra and $\tau \approx 10^{-8} - 10^{-3}$ s for lineshape analysis of wide–line $^2$H NMR spectra) are substantially slower than the characteristic timescale of IQNS spectroscopy ($\tau \leq 500 \times 10^{-12}$ s in the work reported here), and these different approaches therefore provide complementary information on the dynamic properties. For the LT phase of TTMSS, only the methyl group reorientation is effective on the IQNS timescale, and the occurrence of this motion clearly cannot be es-

tablished from the $^{13}$C NMR lineshape analysis techniques discussed in [74]. Interpretation of the $^{13}$C NMR results for the LT phase invoked two additional motions (rotation of each $Si(CH_3)_3$ group about the relevant Si–Si bond, and reorientation of the whole molecule about an axis coincident with one of the Si–Si bonds). Coalescence phenomena arising from both of these motions are observed in the $^{13}$C NMR spectrum just below the phase transition temperature, and these motions occur on timescales of the order of $10^{-3} - 10^{-2}$s; this is consistent with the conclusion from the results discussed here that neither of these motions is effective on the timescale of the IQNS technique. For the HT phase, the $^2$H NMR spectrum at ambient temperature is a single sharp line, consistent with isotropic reorientation which is rapid (i.e. $\tau \leq 10^{-8}$ s) with respect to the timescale of the $^2$H NMR technique. Again, the conclusion from the IQNS spectra that isotropic reorientation is effective on the IQNS timescale for the HT phase is in agreement with the $^2$H NMR results.

In order to understand more deeply the dynamic properties of TTMSS, an important aspect of future research in this area should be to consider the dynamics of chemically related solids, including materials of the type $X[Si(CH_3)_3]_{4-n}[C(CH_3)_3]_n$ (with X = Si, C and n = 0 - 4), many of which are known to undergo transitions to plastic crystal phases at sufficiently high temperature. Indeed, high–resolution solid state $^{13}$C and $^{29}$Si NMR studies [101] of one of these materials ($C[Si(CH_3)_3]_4$) have already revealed interesting and important contrasts with the structural and dynamic properties of TTMSS.

# Chapter 6

# Molecular Dynamics of Cyclohexane and Chlorocyclohexane in Their Thiourea Inclusion Compounds

## Abstract

Incoherent quasielastic neutron scattering (IQNS) has been used to investigate the dynamic properties of cyclohexane and chlorocyclohexane guest molecules in their thiourea inclusion compounds. Thiourea inclusion compounds comprise a crystalline thiourea host structure containing linear tunnels within which the guest molecules are enclosed. Both inclusion compounds are known to undergo solid state phase transitions (at *ca.* 149 K in the case of the thiourea–$d_4$/cyclohexane inclusion compound and *ca.* 192 K for the thiourea–$d_4$/chlorocyclohexane inclusion compound) which are associated with a substantial change in the dynamic characteristics of the guest molecules. Detailed consideration of the quasielastic broadening of the IQNS spectra has established differences between the dynamic properties of the guest molecules in

these different thiourea inclusion compounds. For the thiourea-$d_4$/cyclohexane inclusion compound the guest dynamics can be described as a combination of a 3-fold jump motion of the cyclohexane molecule about the molecular axis and a 3-fold jump motion of the molecular axis about the tunnel axis. Below *ca.* 143 K the 3-fold jump motion about the tunnel axis is no longer detectable. However, the experimental spectra at 143 K cannot be described by the 3-fold jump motion of the cyclohexane molecule about the molecular axis, even though there is still substantial broadening of the spectra. For the thiourea-$d_4$/chlorocyclohexane inclusion compound a satisfactory fit was not obtained for any of the dynamic models considered. This is probably due to the very limited $Q$ range available for fitting the data, due to sizable coherent contributions to the scattering at small $Q$ values as well as inelastic scattering at intermediate $Q$ values.

# 6.1    Introduction

The fact that the thiourea-$d_4$/cyclohexane inclusion compound exhibits at least one low temperature solid–solid phase transition has been known since early studies by Clément *et al.* [85]. Several experimental techniques were used to evaluate the properties of the inclusion compound, including $^{14}N$ Nuclear Quadrupole Resonance (NQR) from the nitrogen atoms of the thiourea host. Four different regions with distinct properties were established. From ambient temperature to *ca.* 242 K a nitrogen resonance was not observed. Below *ca.* 242 K to *ca.* 148 K a single resonance was seen. This observation is consistent with the known crystal structure (space group R3c) of the thiourea/cyclohexane inclusion compound in this temperature range, where all nitrogen atoms are symmetry equivalent. Between *ca.* 148 K and 129 K the experimental data were ambiguous, whereas below *ca.* 129 K five nitrogen resonances were observed. Based on these findings, four "phases" were proposed

in [85]. This assignment of phases was later modified [81] on the basis of more accurate NQR experiments combined with the results of Differential Thermal Analysis (DTA) and X-ray diffraction experiments.

Three temperature regions with significantly different physical properties of both the host and guest substructures can be distinguished. In the temperature range from ambient temperature to $ca.$ 148 K (the high temperature phase) the host substructure is the well known rhombohedral phase [49], as described in Chapter 4. From $^1$H NMR second moment measurements [77] and $^2$H NMR experiments [83, 102] it appears that in this phase the cyclohexane molecules are in rapid, "quasi–isotropic" motion. Poupko $et$ $al.$ [83] found good agreement between the $^2$H NMR spectra measured in this temperature range and spectra simulated on the basis of rapid chair–chair interconversions.

At approximately 148 K the host substructure changes. Clément $et$ $al.$ [81] determined the lattice parameters of the phase below 147 K and assigned the space group P2/c, although the structure was not determined. In the temperature region from 148 K to 129 K (the intermediate phase), the lengths of the a– and b–axes vary monotonously, whereas the length of the c–axis (tunnel axis) remains constant. Nuclear quadrupole resonance (NQR) experiments support the observed lowering of the symmetry: in the high temperature phase all nitrogen atoms from the thiourea host are symmetry equivalent and hence only one NQR signal is observed. Below $ca.$ 148 K, four resonances appear [81] (at a slightly lower temperature still, one of the resonances separates into two distinct resonances) indicating that the nitrogen atoms experience different local environments. Differential thermal analysis does not show a peak at 148 K, and the observed changes were ascribed to a second order phase transition. At the transition temperature, the dynamics of the guest molecules change, as observed via $^1$H NMR second moment measurements [81] and $^2$H NMR experiments [83, 102]. The motion of the guest molecules is fast (on the $^2$H NMR timescale) throughout the intermediate phase.

Poupko *et al.* [83] described three species of cyclohexane in the temperature region between 150 K and 130 K. Initially a new species evolves at the expense of the species exhibiting chair–chair interconversion. The motion of this new species is consistent with reorientation of the cyclohexane molecule about its 3–fold axis combined with biaxial wobbling of the molecule. As the temperature is lowered, the chair–chair interconversion disappears completely and a third species appears to evolve. The motion of the third species is ascribed to reorientation of the cyclohexane molecule about its 3–fold axis alone.

At *ca.* 130 K the "wobbling" species has disappeared. This temperature corresponds to a first order phase transition as observed with DTA. In addition, a discontinuity of the NQR frequencies of the thiourea nitrogen atoms is observed, as well as the appearance of a sixth nitrogen resonance. Below 130 K the lattice parameters of host substructure remain virtually constant. In this phase, Poupko *et al.* [83] interpreted the $^2$H NMR spectra in terms of rapid 3–fold jump rotation of the guest molecules about their 3–fold axis, with the 3-fold axis fixed in space.

For the thiourea–$d_4$/chlorocyclohexane inclusion compound, little has been published regarding the dynamics of the guest molecules. From $^{13}$C NMR studies [74, 103, 89] it is clear that the guest molecule exists predominantly in the axial conformation, which is in contrast to the behaviour of the same molecule in its pure, liquid and vapour phases, in which it exists predominantly in the equatorial conformation [70, 71, 72].

Line shape analysis of $^{13}$C CP/MAS spectra at various temperatures [89] showed that the guest molecules undergo chair–chair interconversions with a temperature dependent rate constant.

In order to gain a more detailed understanding of the dynamic properties of guest molecules in their thiourea inclusion compounds, incoherent quasielastic neutron scattering (IQNS) experiments were carried out. Using deuterated thiourea as the host matrix and guest molecules with natural iso-

topic abundances, the experiments focus selectively on the dynamic properties
of the cyclohexane and chlorocyclohexane guest molecules. Semi–oriented,
polycrystalline samples were used, with all crystals oriented along their nee-
dle axis, corresponding to the crystallographic c–axis and tunnel axis. The
crystals were randomly oriented with respect to rotation around the c–axis.

The semi–oriented samples allow two scattering geometries to be studied,
one with the momentum transfer vector $\underline{Q}$ perpendicular to the the tunnel
axis ($Q_\perp$), and one with $\underline{Q}$ predominantly parallel to the tunnel axis ($Q_\parallel$) (see
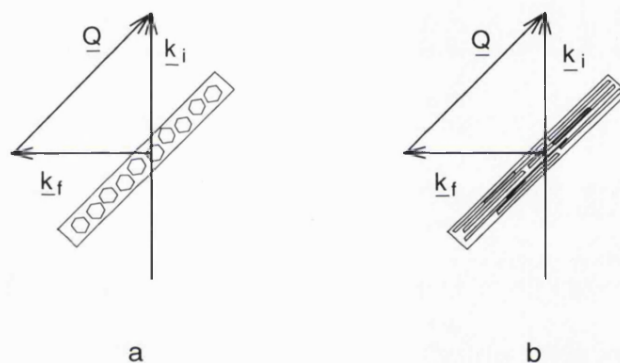Figure 6.1).



**Figure 6.1:** Comparison of the relative sample orientations for the scattering
vector $\underline{Q}$ perpendicular to the tunnel axis ($Q_\perp$, a) and for the scattering vector
parallel to the tunnel axis ($Q_\parallel$, b).

Using these two experimental geometries allows the separation of mo-
tional components perpendicular to the tunnel axis and perpendicular to the
tunnel axis, respectively. For the $Q_\parallel$ geometry, the momentum transfer vector
is strictly parallel to the tunnel axis only for one specific scattering angle. For
the remaining angles, the observed scattering will, to a greater or lesser extent,
contain contributions with the momentum transfer perpendicular to the tunnel
axis.

# 6.2   Experimental

Thiourea-$d_4$/cyclohexane and thiourea-$d_4$/chlorocyclohexane were prepared by
the method described in Section 4.2.1. The solvent used for the preparation
of the inclusion compounds was $CH_3OD$. Thiourea-$d_4$ was used as purchased.

IQNS spectra were recorded on the time–of–flight spectrometer MIBE-
MOL at the Laboratoire Léon Brillouin, Saclay, France. The neutron wave-
length was $\lambda_0 = 6.0$ Å and the instrumental resolution at this wavelength
is *ca.* 80 $\mu$eV. The corresponding experimental timescale is of the order of
$\tau \leq 100 \times 10^{-12}$ s.

The sample was contained in a rectangular, aluminium sample holder,
the interior surface of which was grooved to facilitate orienting of the individual
crystals. The plane of the sample holder was oriented at an angle of $135°$ with
respect to the incident neutron beam.

For the thiourea–$d_4$/cyclohexane inclusion compound, spectra were re-
corded at five temperatures from 275 K to 115 K for both sample geometries.
For thiourea–$d_4$/chlorocyclohexane five spectra in each sample geometry were
recorded for temperatures ranging from 270 K to 50 K. The detectors were
normalized using a spectrum recorded for a vanadium sample with similar
dimensions to the samples of the thiourea inclusion compounds. The scattering
due to the sample environment was subtracted using spectra recorded with an
empty sample container.

Data reduction was performed using the program INX [104] and the data
were analysed using standard least squares fitting procedures.

## 6.3 Qualitative Discussion of the Experimental EISF

Initially an approximate experimental EISF was extracted from the experimental data using the following modified form of Equation 2.47,

$$A_0(\underline{Q}) = \frac{f\, I_{inc}^{el}(\underline{Q})}{f\, I_{inc}^{el}(\underline{Q}) + (1 - f)\, I_{inc}^{qe}(\underline{Q})} \tag{6.1}$$

in order to assess the $Q$–dependence as well as the temperature dependence of the EISF. For extracting the EISF, the experimental data were fitted to an arbitrary model scattering function, and the variable $f$ in Equation 6.1 accounts for any discrepancies between the experimental EISF and the theoretical EISF.

A single Lorentzian line was used, although this approach does not necessarily return accurate values for the EISF. The EISF extracted by this method should, however, give a first approximation to the true experimental EISF and as such will allow possible dynamic models to be identified.

Figure 6.2 shows the EISF as a function of the scattering vector $Q$ extracted from the data for the thiourea–$d_4$/cyclohexane inclusion compound.

The EISF for thiourea–$d_4$/cyclohexane exhibits a clear temperature dependence. At 270 K and 210 K, the EISF is similar within the experimental range of $Q$ values. Below 210 K, the EISF increases with decreasing temperature. As mentioned in Chapter 5, this behaviour can be due either to a change in the spatial characteristics of the motion, or by the motion slowing down to the extent that the instrumental resolution is no longer sufficient to distinguish the quasielastic broadening from elastic scattering.
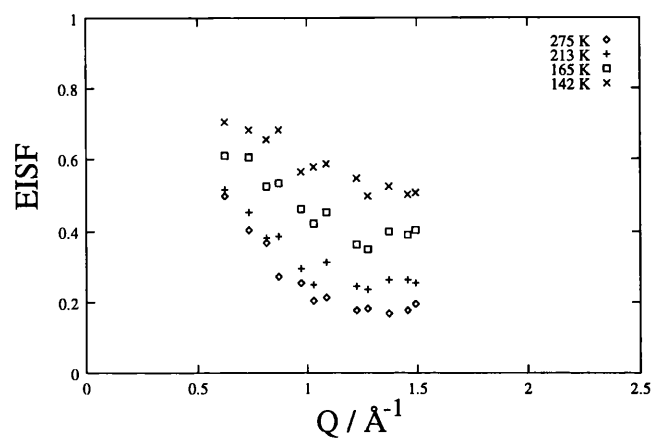
(a) $Q_{\parallel}$
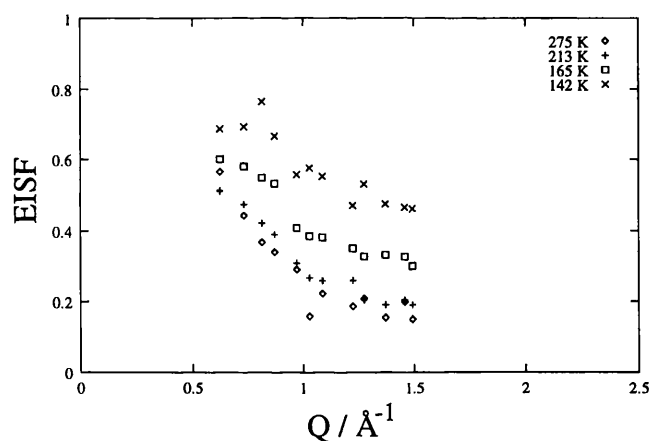


(b) $Q_{\perp}$

**Figure 6.2:** Experimental EISF for the thiourea–$d_4$/cyclohexane inclusion
compound extracted using a single Lorentzian line. (a) $Q_{\parallel}$ geometry, (b) $Q_{\perp}$
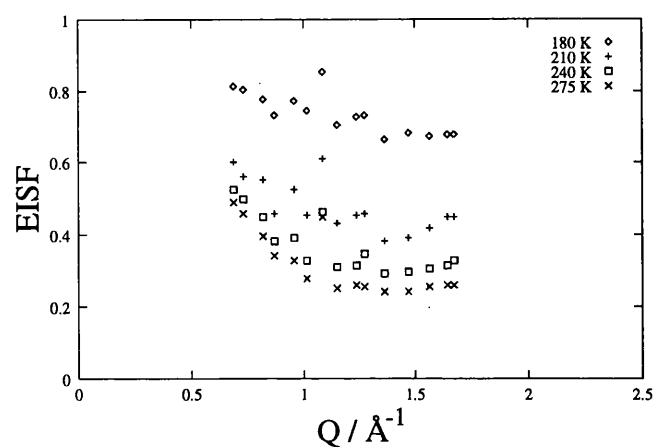geometry.

The EISFs appear to be very similar for both the $Q_{\perp}$ and the $Q_{\parallel}$ scat-
tering geometries. The immediate conclusion from this observation is that
the motion of the cyclohexane molecule has approximately equal components
along the tunnel axis and perpendicular to the tunnel axis. The comparison
is strictly valid only for $Q = 1.48$ $\text{Å}^{-1}$, corresponding to a scattering angle of
$90°$, at which the momentum transfer vector is exactly parallel to the tunnel

axis in $Q_{||}$ geometry.

In view of the temperature dependence of the EISF and the similarity of
the EISF for the $Q_{||}$ and $Q_\perp$ geometries, two possible types of dynamic model
may be proposed to account for the observed behaviour. The first involves
isotropic motion of the $^1$H nucleus within the tunnel, e.g. diffusion within a
sphere. The second involves jumps of the $^1$H nucleus between discrete sites,
but requires the molecule to be tilted within the tunnel, with the molecular
3–fold axis at an angle of approximately 45° with respect to the tunnel axis.
Rotation about the molecular 3–fold axis would then contribute in a similar
manner to both scattering geometries.

The observed temperature dependence could be explained, in the case of
isotropic diffusive motion, by a change in the characteristic length describing
the spatial extent of the motion (e.g. the radius of a sphere within which the
$^1$H nucleus diffuses). In the case of jump motion with the molecular 3–fold
axis tilted at an angle $\zeta$ with respect to the tunnel axis, a change in the EISF
may correspond to a change of the tilt angle. However, a significant deviation
of the tilt angle from ca. 45° would result in considerably different EISFs for
the $Q_{||}$ and $Q_\perp$ geometries (see Section 6.3). In contrast, the EISF initially
extracted from the experimental data remains similar for both experimental
geometries, regardless of the temperature dependence.

Due to the limited range of scattering angles considered, it is difficult to
determine a limiting value of the EISF at high $Q$. Nevertheless, it appears that,
at higher temperatures, the EISF tends towards a value around 0.2, whereas
at lower temperatures, the EISF tends towards higher values. No attempt will
be made to assign possible dynamic models from these limiting values, but
the combined evidence suggests motion consistent with a model that is more
complex than a simple 3–site jump motion.

**(a)** $Q_{\parallel}$
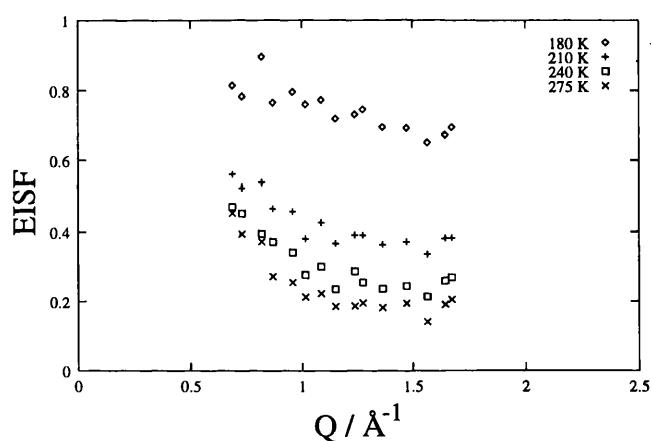


**(b)** $Q_{\perp}$

**Figure 6.3:** Experimental EISF for the thiourea–$d_4$/chlorocyclohexane inclusion compound extracted using a single Lorentzian line. (a) $Q_{\parallel}$ geometry, (b) $Q_{\perp}$ geometry.

In the case of the thiourea–$d_4$/chlorocyclohexane inclusion compound, the general behaviour of the approximate experimental EISF (Figure 6.3) is essentially the same as that of the approximate experimental EISF extracted for the thiourea–$d_4$/cyclohexane inclusion compound. However, subtle differences can be distinguished. The slope of the EISF appears less steep than in the case of thiourea–$d_4$/cyclohexane throughout the experimental temperature

range. In addition, the EISF for the three highest temperatures is consistently
lower in the $Q_{\parallel}$ scattering geometry compared to the $Q_{\perp}$ geometry. For the
lowest temperature, the EISF is again similar for both scattering geometries.

## 6.4   Dynamic Models

On the basis of the above observations, the following dynamic models have
been considered.

**Model I**: 3–Fold jump with the molecular axis tilted at an angle $\zeta$ with re-
spect to the tunnel axis.

This model is essentially the same as Model I described in Section 5.4. The
tilt of the molecular 3–fold axis with respect to the tunnel axis, together with
the fact that the samples are semi–oriented, requires a different averaging pro-
cedure, which is discussed in detail in Appendix A. The resulting scattering
law is given by Equation 2.46 with N = 1 and the structure factors

$$
\begin{aligned}
A_0(Q) &= \frac{1}{3}\left(1 + 2J_0(Qr\sin\psi\cos^2\tfrac{\zeta}{2})\right. \\
&\quad \times \left. J_0(Qr\sin\psi\sin^2\tfrac{\zeta}{2})\, J_0(Qr\cos\psi\sin\zeta)\right) \\
A_1(Q) &= \frac{2}{3}\left(1 - J_0(Qr\sin\psi\cos^2\tfrac{\zeta}{2})\right. \\
&\quad \times \left. J_0(Qr\sin\psi\sin^2\tfrac{\zeta}{2})\, J_0(Qr\cos\psi\sin\zeta)\right)
\end{aligned}
\tag{6.2}
$$

where $Q$ is the scattering vector, $r$ is the distance between the individual sites
occupied by the $^1H$ nucleus, $\zeta$ is the angle between the molecular 3–fold axis
and the tunnel axis, $\psi$ is the angle between $\underline{Q}$ and the tunnel axis, and $J_0$
denotes the cylindrical Bessel function of zero order. For the $Q_{\perp}$ scattering
geometry the Bessel function containing $\cos\psi$ becomes unity, since $\psi = 90°$.
Conversely, when $\underline{Q}$ is strictly parallel to the tunnel axis, the Bessel functions

containing $\sin \psi$ become unity.

The width of the Lorentzian function is given by

$$\Delta_1 = \frac{3}{2\tau_{C_m}} \tag{6.3}$$

where $\tau_{C_m}$ is the correlation time for the jump motion about the molecular 3-fold axis.

**Model II**: Combination of a 3-fold jump about the molecular 3-fold axis with a 3-fold jump of the whole molecule about the tunnel axis.

This model is related to Model III described in Section 5.4. In essence it is a simplification of this model, as the $^1$H nucleus is only allowed to jump on circles that intersect the starting site, and not to sites on circles that do not intersect the original site. It is described by Equation 2.46 with N = 8. The structure factors cannot be given analytically due to the non–spherical averaging required, and are averaged numerically. The scattering function is discussed in more detail in Appendix A. The widths (HWHM) are given by

$$\begin{aligned}
\Delta_1 &= \Delta_2 = \Delta_{C_t} = \frac{3}{2\tau_{C_t}} \\
\Delta_3 &= \Delta_6 = \Delta_{C_m} = \frac{3}{2\tau_{C_m}} \\
\Delta_4 &= \Delta_5 = \Delta_7 = \Delta_8 = \Delta_{C_t} + \Delta_{C_m} = \frac{3}{2\tau_{C_t}} + \frac{3}{2\tau_{C_m}}
\end{aligned} \tag{6.4}$$

where $\tau_{C_m}$ is the correlation time for the jump motion about the molecular 3-fold axis and $\tau_{C_t}$ is the correlation time for the jump motion about the tunnel axis.

**Model III**: Isotropic diffusion within a sphere.

Since the space available to the guest molecules within the tunnels of the thiourea host matrix is large, it is conceivable that the guest molecules experience random motion within the tunnels. The simplest description of this type of motion is isotropic diffusion within a sphere. This model is inherently isotropic so that the semi–oriented nature of the sample has no influence on the results, and the scattering function is independent of the orientation of $\underline{Q}$. It is described by Equation 2.46 with N $= \infty$ [105]. The structure factors are given by

$$A_0(Q) = \left[ \frac{3j_1(Qa)}{Qa} \right]^2$$

$$A_l(Q) = \frac{6(x_n^l)^2}{(x_n^l)^2 - l(l+1)} \left[ \frac{Qa\, j_{l+1}(Qa) - l j_l(Qa)}{(Qa)^2 - (x_n^l)^2} \right]^2 \tag{6.5}$$

where $a$ is the radius of the sphere of diffusion and $j_l$ denotes the spherical Bessel function of order $l$. The $x_n^l$ are factors determined by

$$l j_l(x_n^l) - x_n^l\, j_{l+1}(x_n^l) = 0 \qquad l < 0$$

$$j_1(x_n^0) = 0 \qquad l = 0 \tag{6.6}$$

The widths (HWHM) of the Lorentzian functions are given by

$$\Delta = (2l+1)\frac{(x_n^l)^2 \frac{D}{a^2}}{[(x_n^l)^2 \frac{D}{a^2}]^2 + \omega^2} \tag{6.7}$$

**Model IV**: Linear Diffusion.

For reasons discussed later, the EISF resulting from linear diffusion was also considered. Linear diffusion is described by Equation 2.46 with N = ∞ [106] and the structure factors

$$
\begin{aligned}
A_0(Q_z) &= \frac{2}{Q_z^2 l^2}\left(1 - \cos\left(Q_z l\right)\right) \\
A_n(Q_z) &= \frac{(2Q_z l)^2}{[(Q_z l)^2 - (n\pi)^2]^2}[1 - (-1)^n \cos\left(Q_z l\right)]
\end{aligned}
\tag{6.8}
$$

where $Q_z$ is the component of the scattering vector in the direction of the diffusion and $l$ is the diffusion length.

## 6.5   Results and Discussion

In order for a dynamic model to accurately describe the observed scattering function, it must fit the data for both the $Q_\parallel$ and $Q_\perp$ scattering geometries with the same set of width(s) and geometric parameters. As a consequence, the theoretical EISF calculated for a given model and for a given set of geometric parameters must agree with the experimental EISF in both experimental scattering geometries. The EISF can easily be calculated for different sets of geometric parameters. Comparing the theoretical EISF to the experimental EISF can serve as a first guide in identifying which of the models proposed might fit the experimental data and which models are not compatible with the experimental data. However, it is only by fitting the model to the experimental data that conclusive evidence regarding the correctness of a proposed dynamic model can be obtained. Initially, the experimental EISF discussed in Section 6.3 is compared to theoretical EISFs calculated using the models described in Section 6.4.
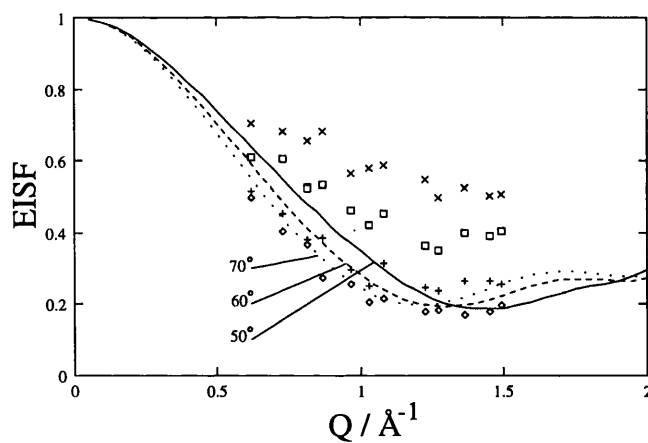
## 6.5.1   Thiourea–d$_4$/Cyclohexane

First, the experimental EISF is compared to the theoretical EISF calculated for
Model I. The cyclohexane molecule contains two distinct types of $^1$H nuclei,
corresponding to the axial and the equatorial positions. As a consequence
there are two distinct jump distances, denoted $r_{ax}$ for the axial hydrogen atoms
and $r_{eq}$ for the equatorial hydrogen atoms. Moreover, the observed scattering
function will represent the average of the scattering functions for the individual
types of hydrogen.

For this model, the molecular geometry is assumed to be rigid with ide-
alised bond lengths of 1.54 Å for the carbon–carbon bonds and 1.1 Å for the
carbon–hydrogen bonds. All bond angles are assumed to be exactly tetrahe-
dral. The corresponding jump distances are $r_{ax} = 1.471$ Å and $r_{eq} = 2.474$ Å.
These jump distances are treated as fixed parameters.

Figure 6.4 compares the experimental EISF for the $Q_{\parallel}$ scattering geom-
etry with the EISF calculated according to Model I with various tilt angles $\zeta$.
For $\zeta = 0°$, the EISF is unity for the scattering vector $\underline{Q}$ strictly parallel to
the tunnel axis, as can be seen in Figure 6.4 at $Q \approx 1.48$ Å$^{-1}$. At large tilt
angles ($70° \leq \zeta \leq 90°$), the theoretical EISF is similar to the experimental
EISF extracted for the data collected at 275 K and 213 K at low values of $Q$.
At higher $Q$ values, the experimental EISF and the theoretical EISF diverge
as the theoretical EISF begins to oscillate about the limiting value of $\frac{1}{3}$. At
165 K, no single theoretical EISF coincides with the experimental EISF. At
the lowest temperature (142 K), the experimental EISF is similar to the theo-
retical EISF calculated for $\zeta = 30°$ at low $Q$ but is higher than the theoretical
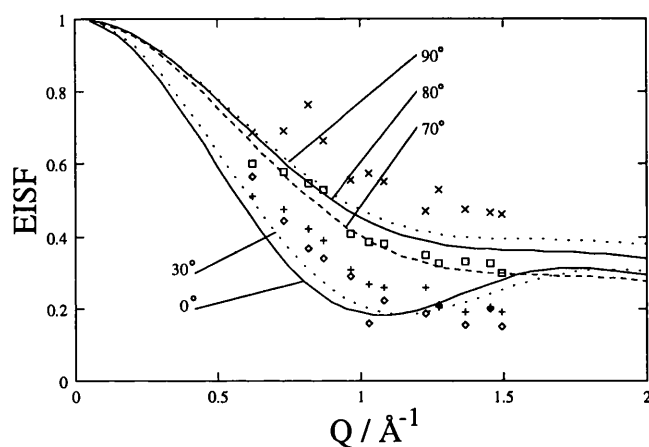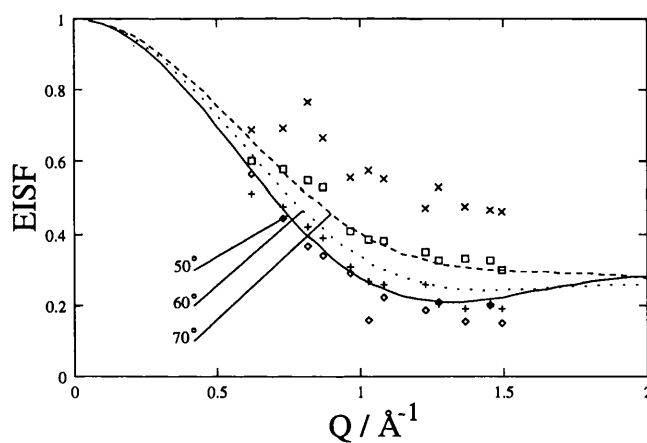EISF at higher $Q$.
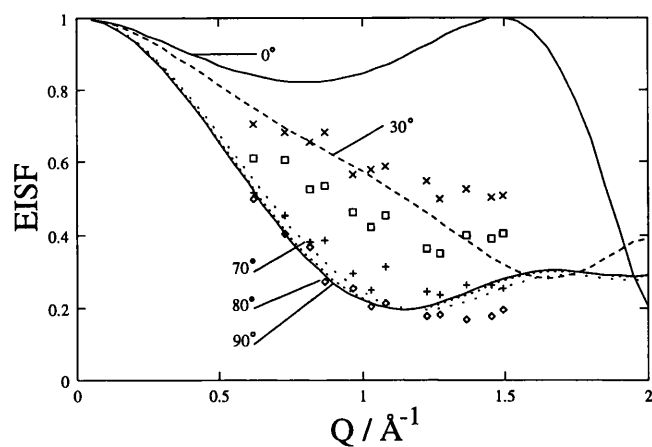
(a)



(b)

**Figure 6.4:** Comparison of the approximate experimental EISF for the $Q_{\parallel}$
scattering geometry of the thiourea–$d_4$/cyclohexane inclusion compound to
the theoretical EISF for Model I, calculated for various tilt angles $\zeta$ of the
molecular axis with respect to the tunnel axis. The symbols denote the ex-
perimental data ($\Diamond$ 275 K, + 213 K, $\square$ 165 K, and $\times$ 142 K), the lines denote
the theoretical EISFs and are labeled with the appropriate tilt angles.

(a)



(b)

**Figure 6.5:** Comparison of the approximate experimental EISF for the $Q_\perp$ scattering geometry of the thiourea–$d_4$/cyclohexane inclusion compound to the theoretical EISF for Model I, calculated for various tilt angles $\zeta$ of the molecular axis with respect to the tunnel axis. The symbols denote the experimental data ($\diamond$ 275 K, $+$ 213 K, $\square$ 165 K, and $\times$ 142 K), the lines denote the theoretical EISFs and are labeled with the appropriate tilt angles.

Figure 6.5 compares the experimental EISF extracted for the $Q_\perp$ scattering geometry to the theoretical EISF calculated with Model I. There are substantial differences in comparison to Figure 6.4. At low $Q$, the theoretical EISF calculated for $0° \leq \zeta \leq 30°$ is systematically lower than the experimental EISF for temperatures 275 K and 213 K. At $Q \approx 1.2$ Å$^{-1}$ the theoretical EISF crosses the experimental EISF to lie at higher values than the experimental EISF. The experimental EISF at 165 K is similar to the theoretical EISF calculated for $\zeta = 70°$, whereas the experimental EISF at 142 K is systematically higher than any of the theoretical EISFs.

To summarize, the Model I cannot describe the experimental data satisfactorily. Although individual theoretical EISFs appear to approximately describe individual data sets, the lack of consistency when comparing the $Q_\parallel$ and $Q_\perp$ scattering geometries suggests that this model cannot adequately account for the experimental data.

Model II is now considered. For this model, the molecular geometry is assumed to be rigid as described above for Model I. In addition, the molecule is assumed to be centred on the tunnel axis and therefore the jump distances required are fully determined by $r_{ax}$ and $r_{eq}$ and the angle $\zeta$ between the molecular 3–fold axis and the tunnel axis.

In the $Q_\parallel$ scattering geometry (Figure 6.6), at 275 K and 213 K, the experimental EISF lies within the range of the theoretical EISFs calculated for $45° \leq \zeta \leq 70°$. The agreement between the theoretical EISF and the experimental EISF is poor at high values of $Q$ ($Q \geq 1.2$ Å$^{-1}$), although the disagreement is not as strong as in the case of Model I. The experimental EISF for the two lowest temperatures lies consistently higher than any of the theoretical EISFs.
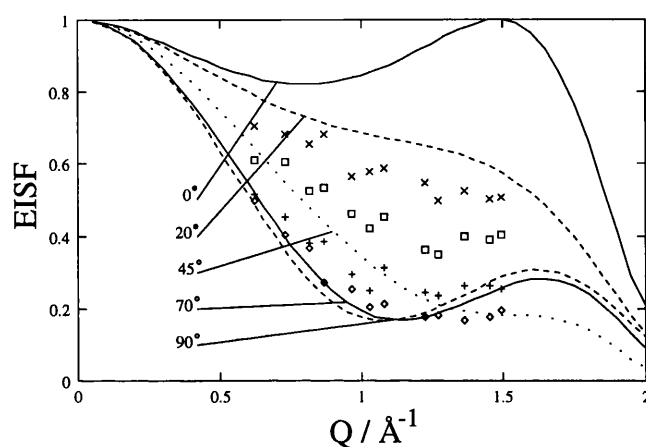
**Figure 6.6:** Comparison of the approximate experimental EISF for the $Q_{\parallel}$ scattering geometry of the thiourea–$d_4$/cyclohexane inclusion compound to the theoretical EISF for Model II calculated using various tilt angles $\zeta$ of the molecular axis with respect to the tunnel axis. The symbols denote the experimental data ($\lozenge$ 275 K, + 213 K, $\square$ 165 K, and × 142 K), the lines denote the theoretical EISFs and are labeled with the appropriate tilt angles.
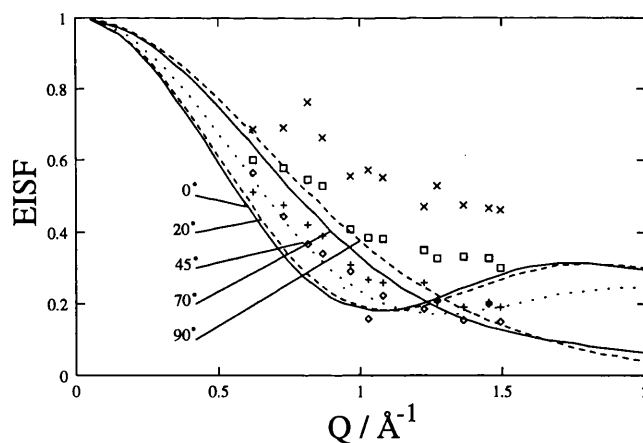


**Figure 6.7:** Comparison of the approximate experimental EISF for the $Q_{\perp}$ scattering geometry of the thiourea–$d_4$/cyclohexane inclusion compound to the theoretical EISF for Model II calculated using various tilt angles $\zeta$ of the molecular axis with respect to the tunnel axis. The symbols denote the experimental data ($\lozenge$ 275 K, + 213 K, $\square$ 165 K, and × 142 K), the lines denote the theoretical EISFs and are labeled with the appropriate tilt angles.
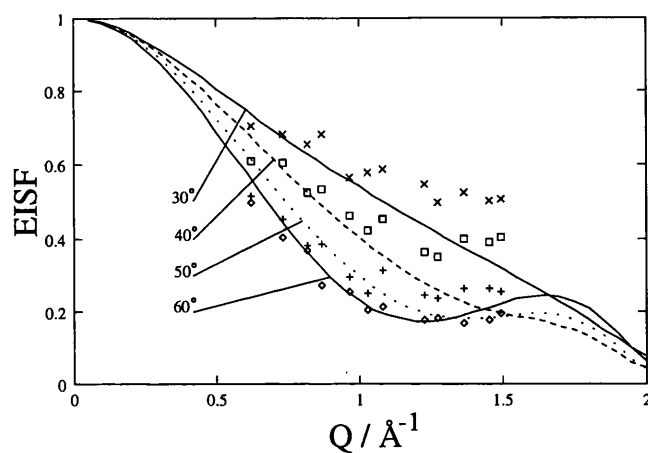
Figure 6.7 shows the comparison between the experimental EISF for the $Q_\perp$ scattering geometry and the theoretically calculated values for Model II. At 275 K and 213 K, the experimental EISF is similar to the theoretical EISFs for $\zeta$ in the range 45°–70°. The discrepancy between the experimental and theoretical EISFs at high $Q$ values is even less pronounced than for the $Q_\parallel$ scattering geometry. Again, the experimental EISF at 165 K and 143 K is consistently higher than any of the theoretical values.

On closer inspection (Figure 6.8), the closest agreement appears at tilt angles $50° \leq \zeta \leq 60°$ for both scattering geometries.

Finally, the experimental EISF is compared to the EISF calculated using Model III for various radii of the sphere of diffusion.

For both scattering geometries, the experimental EISF for all temperatures is lower than any of the theoretical EISFs calculated for radii $a$ of the sphere of diffusion up to 1.2 Å. For $a > 1.2$ Å, none of the theoretical EISFs agree with the experimentally determined values at any temperature (Figure 6.9).

(a) $Q_{\parallel}$
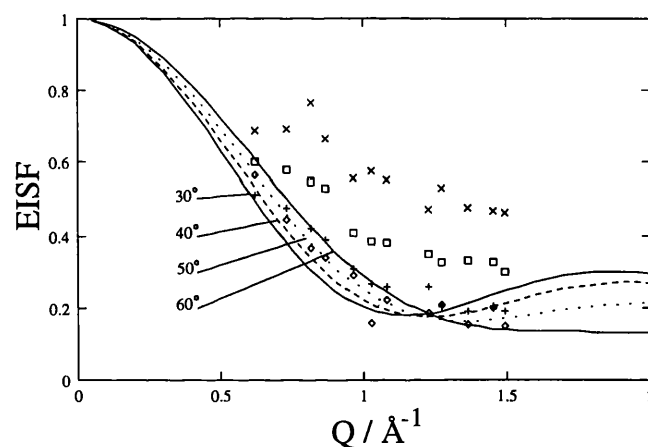


(b) $Q_{\perp}$

**Figure 6.8:** Comparison of the approximate experimental EISF for the $Q_{\parallel}$ scattering geometry (a) and the $Q_{\perp}$ scattering geometry (b) of the thiourea–$d_4$/cyclohexane inclusion compound to the theoretical EISF for Model II calculated using tilt angles $\zeta = 30°$ to $60°$. The symbols denote the experimental data ($\lozenge$ 275 K, + 213 K, $\square$ 165 K, and $\times$ 142 K), the lines denote the theoretical EISFs and are labeled with the appropriate tilt angles.

(a) $Q_{\parallel}$

(b) $Q_{\perp}$

**Figure 6.9:** Comparison between the theoretical EISF obtained from Model III using various radii $a$ for the sphere of diffusion and the experimental EISF for thiourea-$d_4$/cyclohexane (a) in the $Q_{\parallel}$ and (b) in the $Q_{\perp}$ scattering geometry. The symbols denote the experimental data ($\Diamond$ 275 K, + 213 K, $\Box$ 165 K, and $\times$ 142 K), the lines give the theoretical EISF and are labeled with the appropriate radius $a$.
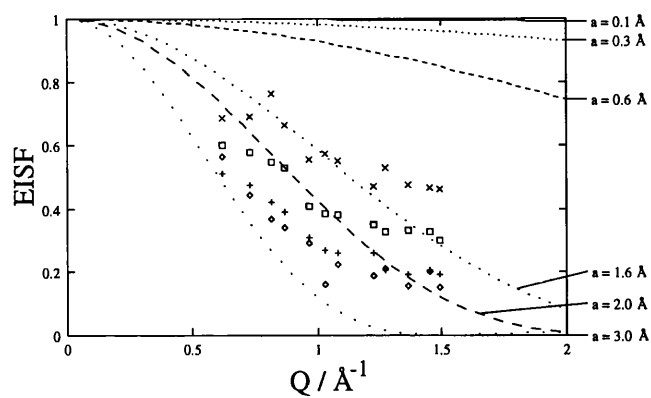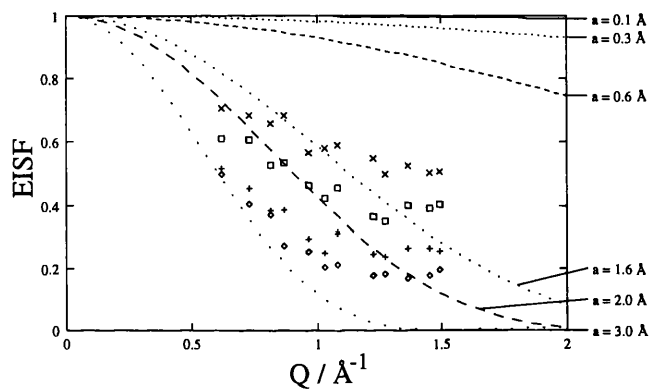
On the basis of the comparison between theoretical EISFs and the experimental EISF described above, Model II was considered for fitting to the experimental spectra.

The model dependent, variable parameters are the width parameters $\Delta_{C_m}$ and $\Delta_{C_t}$, and the angle of tilt $\zeta$. Allowing these parameters to vary freely and independently does not lead to satisfactory and consistent results for either of the experimental scattering geometries. Therefore the following strategy was adopted for the fits.

Figure 6.10 displays the structure factors for Model II for both scattering geometries. The structure factors for $Q_{\parallel}$ are shown in (a). In the experimental $Q$ range, the contribution from the quasielastic structure factors denoted $A_3(Q)$ and $A_6(Q)$ dominate the quasielastic scattering. The structure factors $A_3(Q)$ and $A_6(Q)$ are associated with Lorentzians characterised by the width $\Delta_{C_m}$ (Equation 6.4) and therefore reflect the motion about the molecular axis. The remaining structure factors $A_1(Q)$, $A_2(Q)$, $A_4(Q)$, $A_5(Q)$, $A_7(Q)$, and $A_8(Q)$ are negligible in the experimental $Q$ range. As a consequence, the widths of the spectra in the $Q_{\parallel}$ scattering geometry will reflect predominantly the motion about the molecular axis and should be less sensitive to the motion about the tunnel axis.

In contrast, the $Q_{\perp}$ scattering geometry is entirely dominated by the structure factors $A_4(Q)$ and $A_8(Q)$. As a result, the scattering will reflect both the motion about the molecular axis and the tunnel axis.
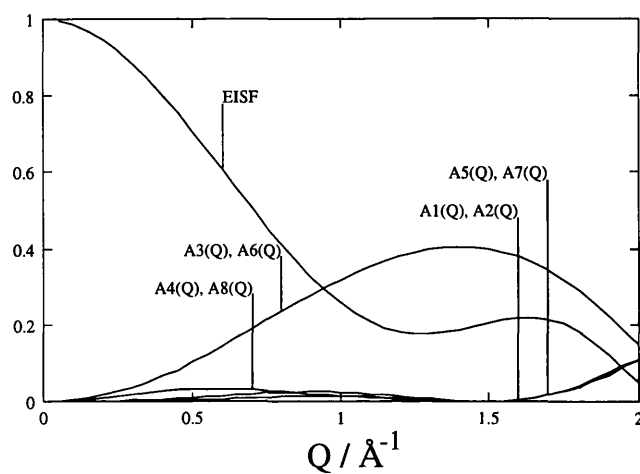
(c) $Q_{\|}$
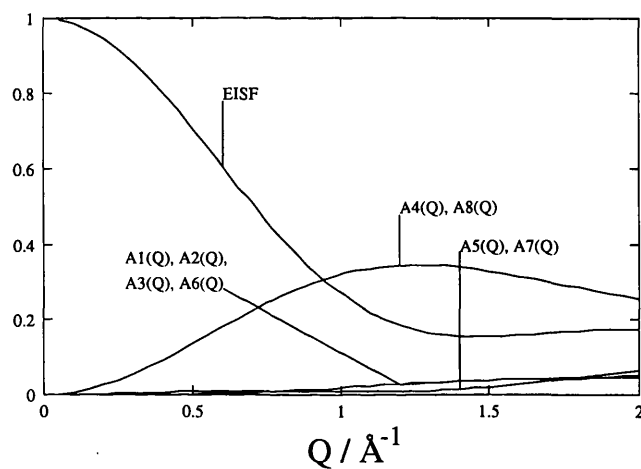


(d) $Q_{\perp}$

Figure 6.10: Structure factors calculated for Model II with tilt angle $\zeta$ = 55°. (a) for $Q_{\|}$, (b) for $Q_{\perp}$ scattering geometry.

To determine the width parameters, the spectra were fit, in the first in-
stance, using a fixed tilt angle $\zeta$. For the $Q_{\parallel}$ scattering geometry, the width
parameter $\Delta_{C_t}$ was initially fixed to an arbitrary value. The width $\Delta_{C_m}$ deter-
mined in this manner was then used as a fixed parameter in fitting the model
to the spectra for the $Q_{\perp}$ scattering geometry. The value thus obtained for
$\Delta_{C_t}$ was then used as a fixed parameter in a repeated fit of the $Q_{\parallel}$ scattering
geometry. This process was repeated several times until the width parameters
remained constant.

Table 6.1 gives the widths extracted from the initial fits of Model II
together with the characteristic times $\tau_{C_t}$ and $\tau_{C_m}$. As expected, the width
of the Lorentzian lines decreases with decreasing temperature, indicating that
the motion of the cyclohexane molecule slows down. $\Delta_{C_m}$ is generally greater
than $\Delta_{C_t}$, indicating that the motion of the molecule about the molecular axis
is faster than the motion of the molecular axis about the tunnel axis.

**Table 6.1:** Lorentzian line widths and correlation times for thiourea–$d_4$/cyclo-
hexane from Model II.

| T / K | $\Delta_{C_m}$ / meV | $\tau_{C_m}$ / s | $\Delta_{C_t}$ / meV | $\tau_{C_t}$ / s |
|---|---|---|---|---|
| 275 | 0.197 | $3.15 \times 10^{-11}$ | 0.145 | $4.27 \times 10^{-11}$ |
| 213 | 0.111 | $5.59 \times 10^{-11}$ | 0.054 | $1.15 \times 10^{-10}$ |
| 165 | 0.046 | $1.35 \times 10^{-10}$ | 0.023 | $2.64 \times 10^{-10}$ |
| 143 | 0.031 | $2.03 \times 10^{-10}$ | 0.002 | $3.65 \times 10^{-9}$ |

For T = 143 K, $\Delta_{C_t}$ is considerably below the instrumental resolution
and the motion associated with this width parameter is therefore not strictly
observable on the experimental timescale. It is noteworthy that this is below
the phase transition temperature ($T_t$ = 149 K). Two explanations for this
behaviour can be offered. The low value of $\Delta_{C_t}$ can either be due to the
motion slowing to such an extent that its characteristic time $\tau_{C_t}$ is no longer
within the experimental timescale or due to the fact that this motion freezes

at a temperature above 143 K but below 165 K. If the 3-fold jump about the tunnel axis freezes above 143 K, Model II is no longer applicable. If, on the other hand, the motion merely slows to the extent that it is no longer resolved, the experimental EISF will appear larger than it actually is since the scattering due to this particular motion of the cyclohexane molecule will no longer be distinguishable from the elastic scattering.

To test which of the two scenarios is the more likely, Model I was fitted to the experimental data for T = 143 K. If the 3-fold jump motion about the tunnel axis ceases, only the 3-fold jump about the molecular axis remains. In this case, Model I is applicable and should fit the observed scattering function. The results from these fits will be discussed later.

From the correlation times obtained from the fits with Model II, activation parameters have been extracted assuming Arrhenius behaviour ($\tau = \tau_0 \exp(E_a/RT)$, Figure 6.11). Only the correlation times of the fits at temperatures from 275 K to 163 K were considered. The resulting values for $\tau_0$ and $E_a$ are $\tau_{0,C_m} = 3.44 \times 10^{-12}$ s and $E_a = 5.01$ kJ mol$^{-1}$ for the motion about the molecular axis and $\tau_{0,C_t} = 3.06 \times 10^{-12}$ s and $E_a = 6.19$ kJ mol$^{-1}$ for the motion about the tunnel axis.



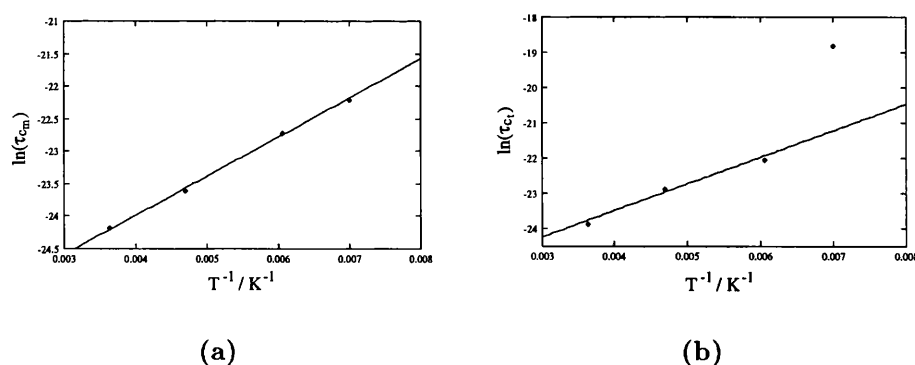(a)                               (b)

**Figure 6.11:** Plot of $\ln \tau/s$ *versus* $T^{-1}$ / $K^{-1}$ for $\tau_{C_m}$ (a) and $\tau_{C_t}$ (b)

In the final fits of Model II the width parameters were kept constant at the values obtained from the initial fits discussed above. The only model

dependent variable parameter was the angle of tilt $\zeta$. Initially $\zeta$ was allowed to vary freely. For T = 275 K, this approach led to consistent values of $\zeta$ in both scattering geometries ($\zeta$ = 53.32° for $Q_{\parallel}$, $\zeta$ = 57.33° for $Q_{\perp}$ geometry). For T = 213 K, the final value for $\zeta$ is similar to the value obtained at 275 K only in the $Q_{\parallel}$ scattering geometry ($\zeta$ = 55.49°). In the $Q_{\perp}$ scattering geometry the final value for $\zeta$ is much lower than the value obtained for the $Q_{\parallel}$ scattering geometry. However, the agreement between the calculated spectra and the experimental spectra is poor and the experimental EISF differs considerably from the theoretical EISF. Therefore $\zeta$ was fixed at the value found for the $Q_{\parallel}$ scattering geometry and the fitting was repeated. This lead to a significant improvement in the agreement between the calculated and experimental spectra as well as between the experimental EISF and the theoretical EISF (see Figure 6.12).

Figure 6.13 shows the fits of the experimental data to the calculated spectra for Model II.
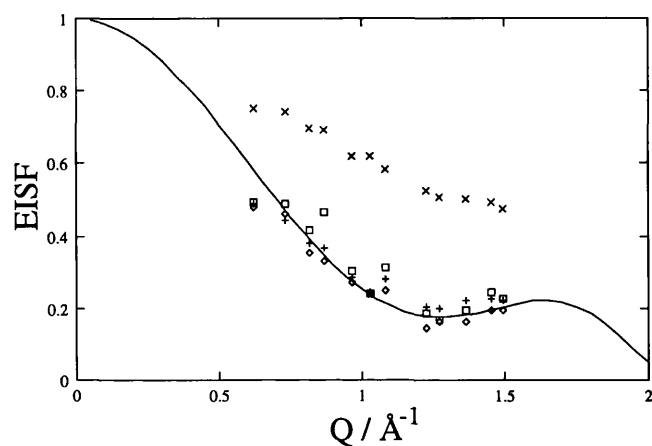
(c) $Q_\parallel$
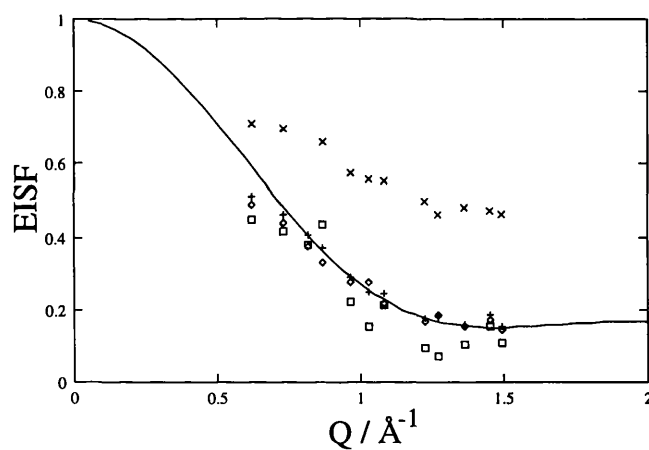
(d) $Q_\perp$

**Figure 6.12:** Experimental EISF for the thiourea-$d_4$/cyclohexane inclusion compound extracted from the fits with Model II. The full line represents the theoretical EISF calculated for $\zeta = 55.49°$ the symbols represent the experimental data ($\lozenge$ 275 K, + 213 K, $\square$ 165 K, and × 142 K). (a) $Q_\parallel$ scattering geometry, (b) $Q_\perp$ scattering geometry.

(a) $Q = 0.62$ Å$^{-1}$

(b) $Q = 0.62$ Å$^{-1}$

(c) $Q = 0.97$ Å$^{-1}$

(d) $Q = 0.97$ Å$^{-1}$

(e) $Q = 1.27$ Å$^{-1}$

(f) $Q = 1.27$ Å$^{-1}$

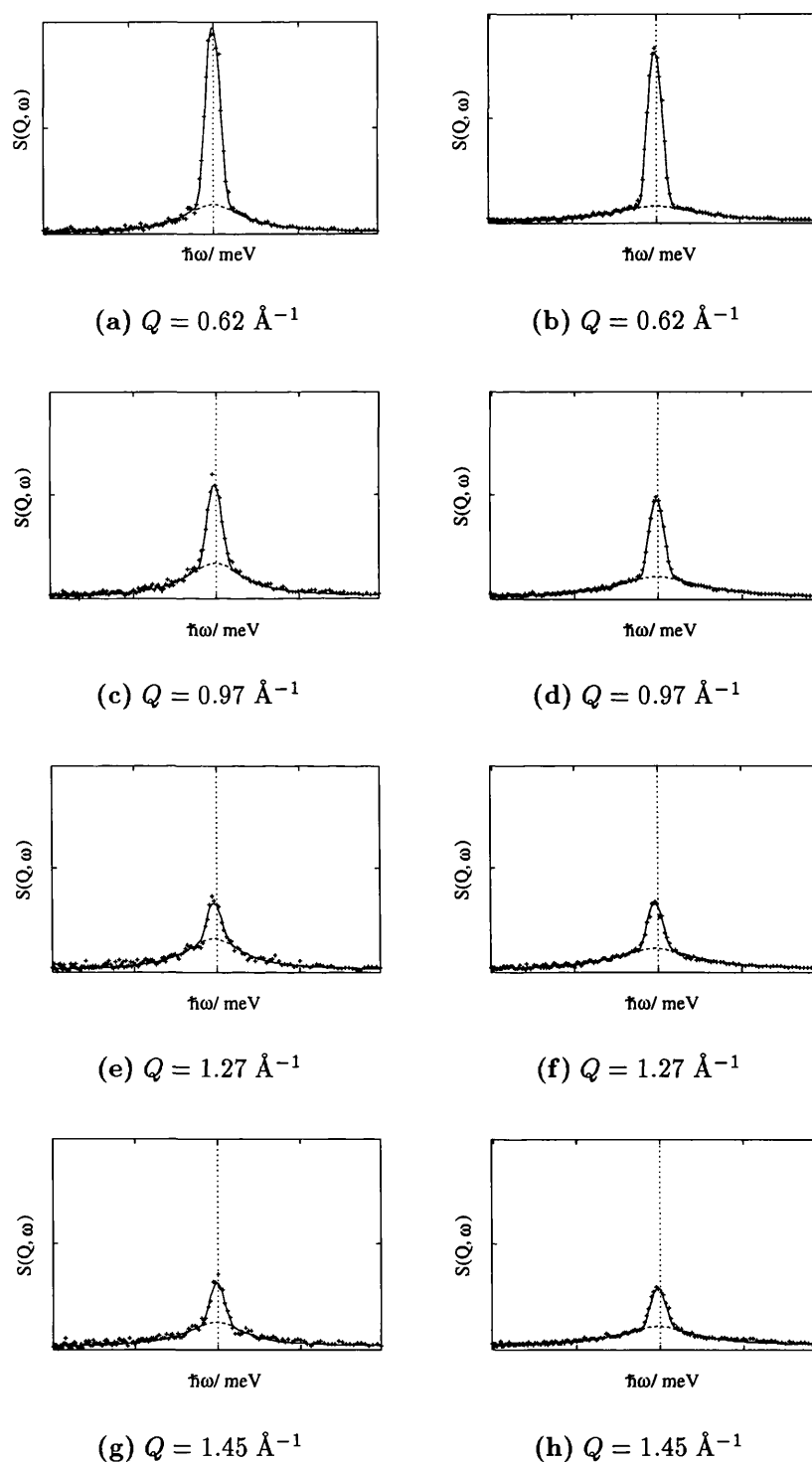(g) $Q = 1.45$ Å$^{-1}$

(h) $Q = 1.45$ Å$^{-1}$

**Figure 6.13:** Comparison between the experimental spectra at T = 273 K and calculated spectra assuming Model II. The points represent the experimental data, the full line is the fit, and the dashed line shows the quasielastic contribution. (a), (c), (e), (g) $Q_{\parallel}$ scattering geometry, (b), (d), (f), (h) $Q \perp$ scattering geometry.

For the spectra recorded at 165 K and 143 K varying $\zeta$ did not result in satisfactory fits. The angle was therefore fixed at the value obtained from the $Q_\parallel$ scattering geometry at T = 213 K. At 165 K this leads to acceptable agreement between the calculated and experimental spectra. The agreement between the experimental EISF and the theoretical EISF is less good. A systematic increase in the experimental EISF extracted from the fits for the $Q_\parallel$ scattering geometry is observed, whereas the experimental EISF extracted for the $Q_\perp$ scattering geometry varies considerably within the experimental $Q$ range and is generally lower than the theoretical EISF.

At 143 K the agreement between the experimental spectra and the calculated spectra is also acceptable, although the experimental EISF is considerably higher than the theoretical EISF.

The Debye–Waller factors resulting from these fits are found to be high. The values range from 0.383 Å$^2$ for the $Q_\parallel$ scattering geometry at T = 275 K to 0.0984 for the $Q_\perp$ scattering geometry at T = 143 K. In addition the Debye–Waller factor appears to depend upon the scattering geometry. Together with the magnitude of the Debye–Waller factor, this might indicate the presence of a further, anisotropic component to the observed quasielastic scattering, the amplitude of which would necessarily be small compared with the amplitude of the motion described by Model II. In this respect linear diffusion (Model IV) with a small diffusion length $l$ and differing diffusion lengths $l_\parallel$ and $l_\perp$ for motion parallel and perpendicular to the tunnel axis, respectively, can serve as a first approximation.

Figure 6.14 depicts the theoretical EISF for linear diffusion calculated for various values of the diffusion length $l$. The EISF is small within the experimental $Q$ range for values of $l \leq 0.5$ Å and even at $l = 2$ Å the theoretical EISF is still greater than the initially extracted experimental values. However, in order to fulfill the normalization condition (Equation 2.38) this model requires N $\geq$ 100 in Equation 2.46, even in the limited experimental $Q$

range.
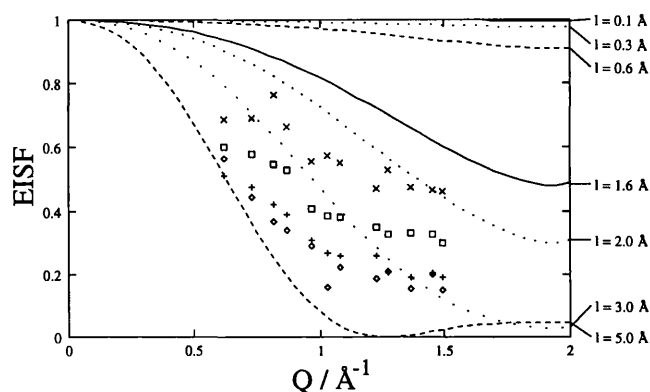


**(a)** $Q_{\parallel}$
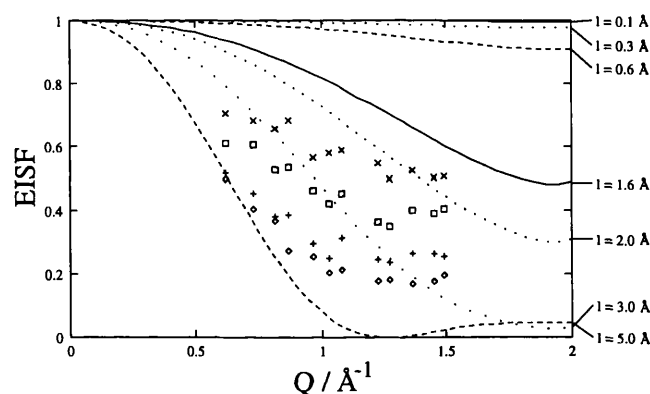


**(b)** $Q_{\perp}$

**Figure 6.14:** Comparison of the theoretical EISF for Model IV calculated using various values for the diffusion length $l$ to the experimental EISF for the thiourea-$d_4$/cyclohexane inclusion compound (a): $Q_{\parallel}$, (b): $Q_{\perp}$. The symbols denote the experimental data ($\Diamond$ 275 K, $+$ 213 K, $\Box$ 165 K, and $\times$ 142 K), the lines denote the theoretical EISFs and are labeled with the appropriate diffusion length.

Owing to the fact that this model alone cannot describe the experimental data it would have to be used in conjunction with, for example, Model II. A convolution of Model II and Model IV would then require in excess of 900 Lorentzian functions in Equation 2.46. It was therefore felt that the computational time required to fit such a model to the experimental data, together

with the poor quality of the experimental data did not justify the use of Model IV or a convolution of this model with other models to explore the origin of the high Debye–Waller factor.

In order to test the hypothesis of the 3–fold jump motion about the tunnel axis freezing above 143 K, Model I was fitted to the experimental data at this temperature. The jump lengths $r_{ax}$ and $r_{eq}$ were treated as fixed parameters. In the $Q_{\parallel}$ scattering geometry the resulting tilt angle is $\zeta = 52.32°$ and the linewidth of the Lorentzian is of the order of the instrumental resolution ($\Delta_{C_m} = 0.0707$ meV). However, the resulting theoretical EISF is consistently lower than the experimental EISF (Figure 6.15).

For the $Q_{\perp}$ scattering geometry the tilt angle and the width of the Lorentzian from the $Q_{\parallel}$ scattering geometry were used as fixed parameters. In this case the resulting theoretical EISF is considerably lower than the experimental EISF.

In conclusion, Model I cannot explain the dynamics of the cyclohexane molecule at 143 K. It is conceivable that the motion of the cyclohexane molecule consists of low amplitude oscillations such as a wobbling motion about the molecular axis, although slowing down of the motion described by Model II or even Model I to a degree where it is no longer resolved by the instrumental resolution would also appear to increase the EISF since the quasielastic scattering would no longer be distinguishable from the genuine elastic scattering.
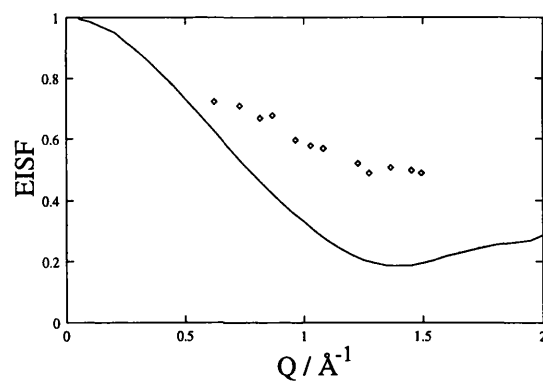
(c) $Q_{\|}$
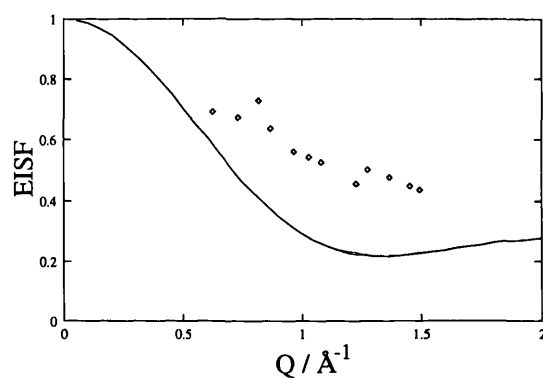


(d) $Q_{\perp}$

**Figure 6.15:** Experimental EISF ($\Diamond$) for the thiourea-$d_4$/cyclohexane inclusion compound extracted from the fits with Model I at T = 143 K. The full line represents the theoretical EISF calculated for $\zeta = 53.23°$. (a) $Q_{\|}$ geometry, (b) $Q_{\perp}$ scattering geometry.
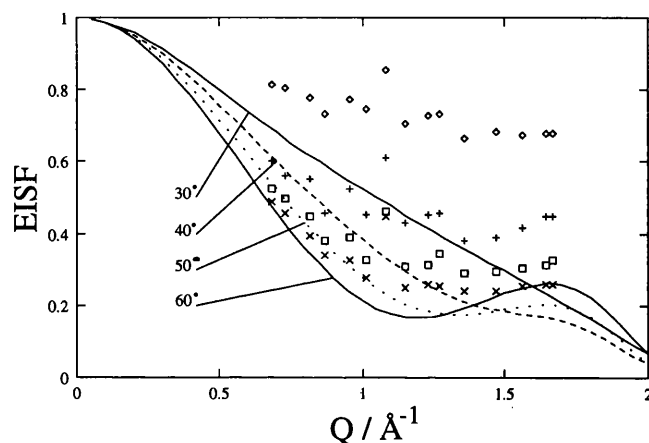
## 6.5.2 Thiourea–$d_4$/Chlorocyclohexane

Figure 6.16 compares the EISFs calculated for Model II to the approximate experimental EISF. The jump lengths $r_{ax}$ and $r_{eq}$ employed for Models I and II were the same as in the case of the thiourea–$d_4$/cyclohexane inclusion compound. Chlorocyclohexane, however, has one less axial hydrogen (in its thiourea inclusion compound, the chlorocyclohexane is predominantly in the axial conformation [70, 71, 72]) and the respective contributions of the axial and the equatorial hydrogen atoms to the observed scattering was weighted accordingly. Since the approximate experimental EISF for the thiourea–$d_4$/chlorocyclohexane is very similar to the approximate experimental EISF for the thiourea–$d_4$/cyclohexane, the comparison leads to essentially the same results as for cyclohexane, and on this basis Model II was also considered for fitting to the experimental data. The same procedure as described in subsection 6.5.1 was applied.

The results are similar in many ways to those found for the thiourea–$d_4$/cyclohexane, although there are large differences in details of the spectra and the experimental EISF extracted from the fits. The discussion is focused on these aspects.

In both the $Q_{\parallel}$ and the $Q_{\perp}$ scattering geometries, the intensities at the first three scattering angles ($Q = 0.69$ to $0.82$ Å$^{-1}$) are enhanced compared to the intensities at the other scattering angles. This is reflected in the experimental EISF (Figure 6.3) by a step between the third and the fourth points. This step is more pronounced at some temperatures than others.

Furthermore, enhanced elastic intensity is also seen at $Q = 1.08$ Å in the $Q_{\parallel}$ scattering geometry. These enhanced intensities are possibly due to coherent scattering from the ($10\bar{1}$) reflection and the ($110$) reflection of the thiourea inclusion compound. The reason why the coherent scattering is more pronounced here than in the thiourea–$d_4$/cyclohexane could be due to the

relatively large coherent scattering cross section of chlorine ($\sigma_c$ = 11.53 ×

$10^{-24}\, cm^2$).



(a)
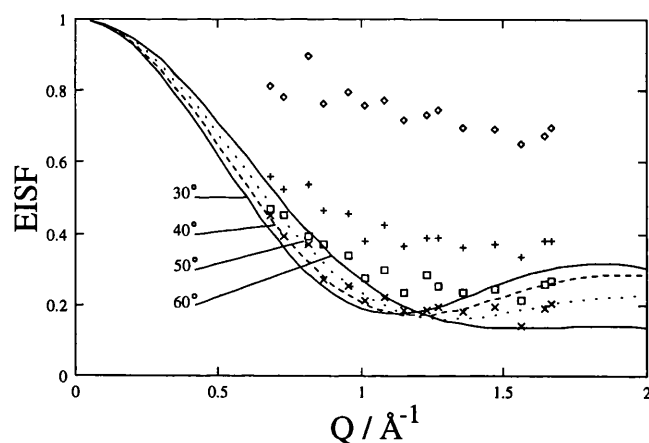


(b)

**Figure 6.16:** Comparison of the approximate experimental EISF for the the
thiourea–$d_4$/chlorocyclohexane inclusion compound to the theoretical EISF
for Model II calculated using various tilt angles $\zeta$ of the molecular axis with
respect to the tunnel axis. The symbols denote the experimental data ($\Diamond$
270 K, + 240 K, □ 210 K, and × 180 K), the lines denote the theoretical
EISFs and are labeled with the appropriate tilt angles.

The spectra recorded at scattering angles $\theta$ = 89.23° to 103.48° ($Q$ =
1.36 to 1.64 Å$^{-1}$) also show increased intensity (although this is not obvious

from the experimental EISF). Here, as shown in Figure 6.17, inelastic scatter-
ing close to the elastic line in the $Q_\perp$ scattering geometry is responsible for the
apparent increase in the intensity. The inelastic scattering is most prominent
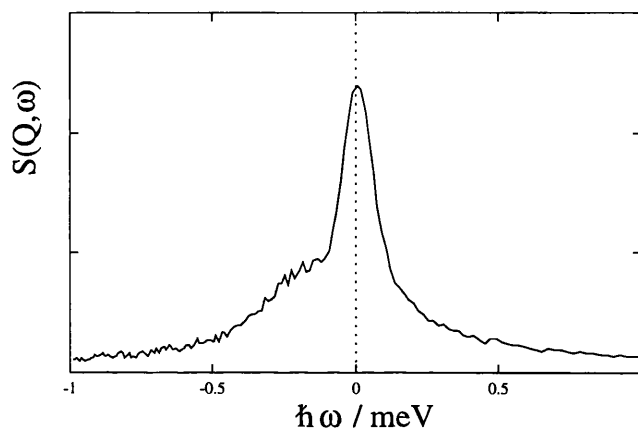at $\theta = 90.60°$ ($Q = 1.56\,\text{Å}^{-1}$).



**Figure 6.17:** IQNS spectrum of thiourea–$d_4$/chlorocyclohexane in the $Q_\perp$
scattering geometry. The experimental temperature is 270 K, the scattering
angle is 96.60° corresponding to a scattering vector $Q = 1.56$ Å$^{-1}$. The
inelastic scattering is clearly visible.

In the $Q_\parallel$ scattering geometry the inelastic scattering is not apparent,
although the intensity of the spectra is also increased: the angles at which
inelastic scattering occurs are close to the angle at which $Q$ is strictly parallel
to the tunnel axis in the $Q_\parallel$ scattering geometry; hence the contribution from
motion perpendicular to the tunnel axis will be small. For these reasons, the
spectra recorded at scattering angles $\theta = 38.25°$, $40.75°$, $45.83°$, $62.45°$, and
89.23 to 103.40° were excluded from consideration when fitting the spectra.

The fit of the spectra recorded at T = 275 K results in a tilt angle of
$\zeta = 60.20°$. The widths $\Delta_{C_m}$ and $\Delta_{C_t}$ are lower than those found for the
thiourea–$d_4$/cyclohexane inclusion compound at the same temperature (see
Table 6.2). In the $Q_\perp$ scattering geometry a satisfactory fit cannot be obtained
when treating the tilt angle $\zeta$ as a variable parameter. This is in contrast to
the behaviour of thiourea–$d_4$/cyclohexane, for which the tilt angles resulting

from the fits at this temperature in both scattering geometries are in close

agreement, even when the tilt angle is treated as a variable parameter in both

cases. Therefore the tilt angle in the $Q_\perp$ scattering geometry was fixed to the

value obtained in the $Q_\parallel$ scattering geometry. The resulting experimental EISF

is considerably lower than the theoretical EISF in both scattering geometries

(Figure 6.18).

**Table 6.2:** Lorentzian line widths and correlation times for thiourea–d$_4$/chloro-
cyclohexane from Model II.

| T / K | $\Delta_{C_m}$ / meV | $\tau_{C_m}$ / s | $\Delta_{C_t}$ / meV | $\tau_{C_t}$ / s |
|---|---|---|---|---|
| 270 | 0.115 | $5.41 \times 10^{-11}$ | 0.057 | $1.08 \times 10^{-10}$ |
| 240 | 0.079 | $7.83 \times 10^{-11}$ | 0.038 | $1.65 \times 10^{-10}$ |
| 210 | 0.046 | $1.35 \times 10^{-10}$ | 0.015 | $4.10 \times 10^{-10}$ |
| 180 | 0.014 | $4.36 \times 10^{-10}$ | 0.002 | $3.65 \times 10^{-9}$ |

For the lower temperatures, the tilt angle cannot be treated as a variable

parameter in the fits as this leads to inconsistent results. Therefore the angle

$\zeta$ was fixed at the value obtained at 270 K. At T = 240 K and 210 K, the

calculated spectra fit the experimental spectra well. The experimental EISF is

similar to the experimental EISF at T = 270 K to 210 K. In the $Q_\perp$ scattering

geometry the experimental EISF displays a regular trend, where the EISF is

lowest at T = 270 K and highest at T = 210 K. At all three temperatures,

though, the experimental EISF is lower than the theoretical EISF. In the $Q_\parallel$

scattering geometry the experimental EISF at T = 240 K is lower than the

experimental EISF at T = 270 K, whereas the experimental EISF at T =

210 K is greater than the experimental EISF at T = 270 K.
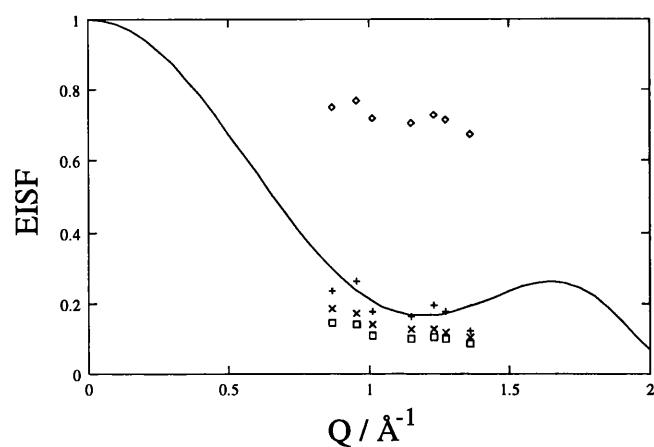
(a)
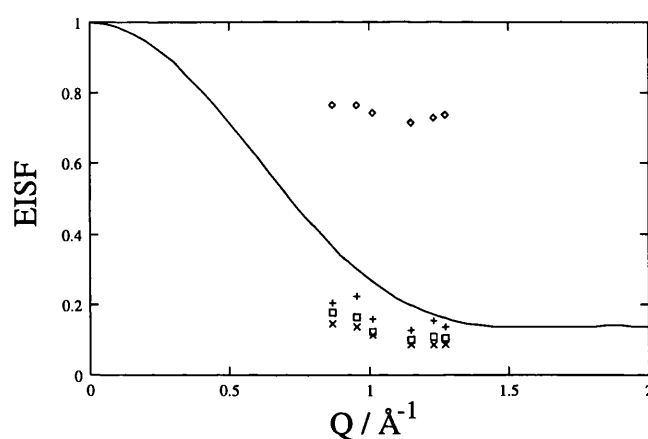


(b)

**Figure 6.18:** Experimental EISF for the thiourea–$d_4$/chlorocyclohexane inclusion compound extracted from the fits with Model II. The full line represents the theoretical EISF calculated for $\zeta = 60.20°$, the symbols represent the experimental data ($\Diamond$ 270 K, + 240 K, $\Box$ 210 K, and $\times$ 180 K). (a) $Q_{\parallel}$ scattering geometry, (b) $Q_{\perp}$ scattering geometry.

Again the experimental EISF is generally lower than the theoretical EISF.

The reason for this behaviour is unclear. It is entirely possible that there is an

additional, small amplitude component to the motion of the chlorocyclohexane

molecule. However, the true dynamics of the chlorocyclohexane molecule in

its thiourea inclusion compound might be described by an entirely different

model than Model II. Several different types of motion can be envisaged, such as small amplitude oscillations of the molecular axis about an average tilt angle or oscillations of the molecular axis about the tunnel axis.

At T = 180 K, Model II fits reasonably well to the experimental spectra, but as for the thiourea–$d_4$/cyclohexane inclusion compound at T = 143 K, the experimental EISF is considerably higher than the theoretical EISF. The width parameter $\Delta_{C_t}$ is much lower than the instrumental resolution and the same conclusions must be drawn as those discussed above for the thiourea–$d_4$/cyclohexane inclusion compound at 143 K.

From the correlation times obtained from the fits, tentative activation parameters have been extracted assuming Arrhenius behaviour (*vide supra*, Figure 6.19). Only the correlation times derived from the fits at T = 270 K to 210 K were considered. The resulting values for $\tau_0$ and $E_a$ are $\tau_{0,C_m}$ = 2.16 × 10$^{-12}$ s and $E_a$ = 7.02 kJ mol$^{-1}$ for the motion about the molecular axis and $\tau_{0,C_t}$ = 9.11 × 10$^{-13}$ s and $E_a$ = 10.59 kJ mol$^{-1}$ for the motion about the tunnel axis.

Figure 6.20 shows the fits of the experimental data to the calculated spectra for Model II.



(a)                                  (b)
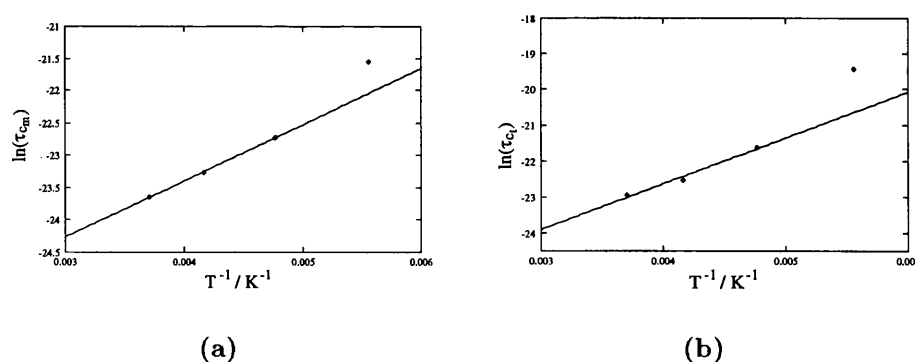
**Figure 6.19:** Plot of $\ln \tau / s$ *versus* T$^{-1}$ / K$^{-1}$ for $\tau_{C_m}$ (a) and $\tau_{C_t}$ (b)

**(a)** $Q = 0.87$ Å$^{-1}$

**(b)** $Q = 0.87$ Å$^{-1}$

**(c)** $Q = 1.15$ Å$^{-1}$

**(d)** $Q = 1.15$ Å$^{-1}$

**(e)** $Q = 1.36$ Å$^{-1}$

**(f)** $Q = 1.36$ Å$^{-1}$

**(g)** $Q = 1.64$ Å$^{-1}$

**(h)** $Q = 1.64$ Å$^{-1}$

**Figure 6.20:** Comparison between the experimental spectra at T = 270 K and
calculated spectra assuming Model II. The points represent the experimental
data, the full line is the fit, and the dashed line represents the quasielastic
contribution. (a), (c), (e), (g) $Q_{\parallel}$ scattering geometry, (b), (d), (f), (h) $Q\perp$
scattering geometry.

## 6.6 Conclusions

The study of the thiourea–$d_4$/cyclohexane and thiourea–$d_4$/chlorocyclohexane inclusion compounds *via* IQNS has provided valuable insights into the dynamics of the guest molecules at various temperatures.

Above the phase transition temperature of the thiourea–$d_4$/cyclohexane inclusion compound, the guest molecules have been shown to undergo motion consistent with a model combining 3–fold jumps of the cyclohexane molecule about the molecular axis with 3–fold jumps of the molecule about the tunnel axis of the host matrix. In this model the molecular ax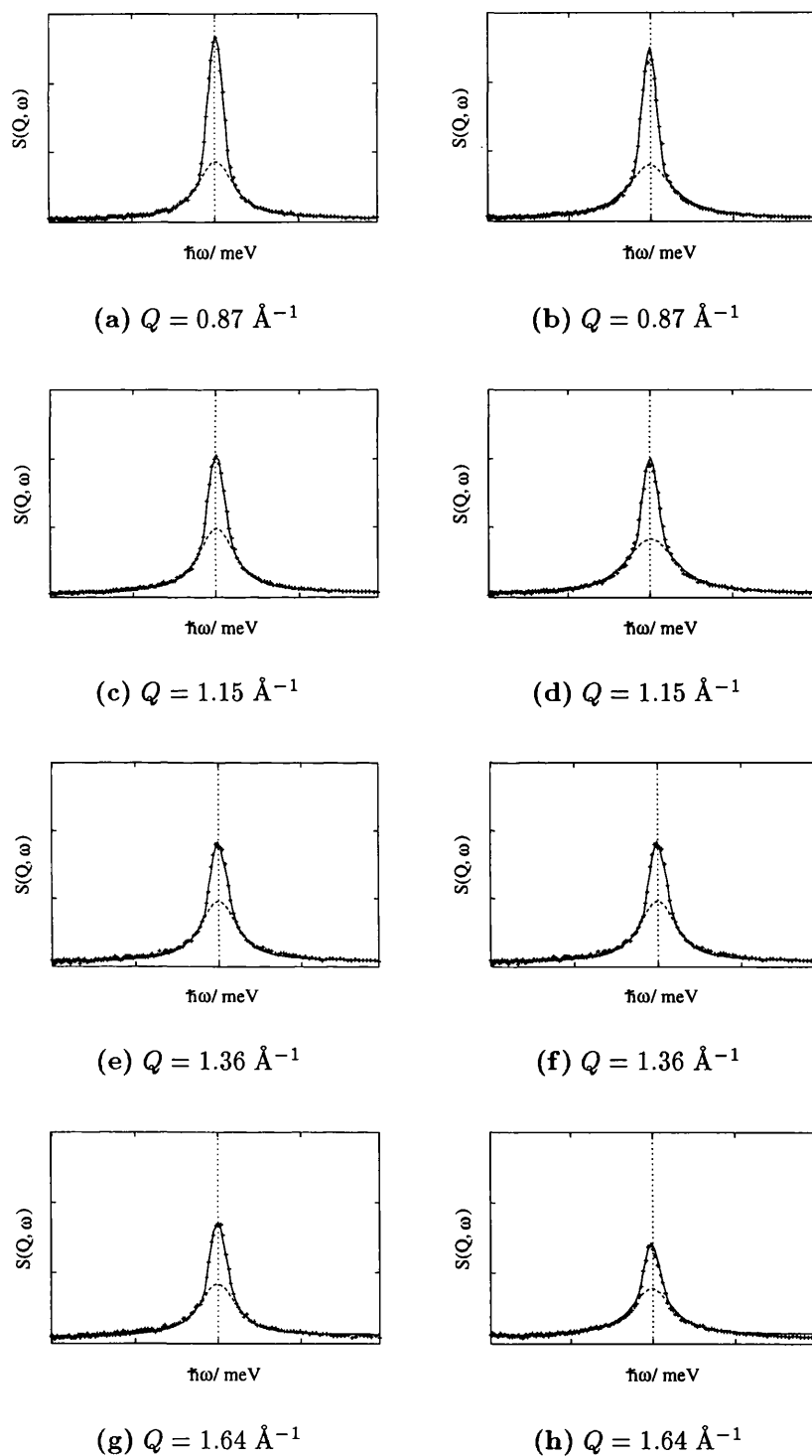is is tilted with respect to the tunnel axis and the tilt angle was determined to be *ca.* 55° at T = 275 K and 213 K. At 165 K, the tilt angle was not fitted unambiguously, but fits with the angle fixed to the value obtained at higher temperature describe the experimental data well.

Below the phase transition temperature ($T_t \approx$ 149 K [81]) the experimental data can no longer be accounted for by Model II, and it appears that this is due to lack of instrumental resolution.

The activation parameters for the two types of motion are $\tau_{0,C_m}$ = 3.44 × $10^{-12}$ s and $E_{a,C_m}$ = 5.01 kJ mol$^{-1}$ for the 3-fold jump motion about the molecular axis and $\tau_{0,C_t}$ = 3.08 × $10^{-12}$ s and $E_{a,C_t}$ = 6.19 kJ mol$^{-1}$ for the motion about the tunnel axis. These values compare favourably with the activation energy for reorientations of the cyclohexane molecule ($E_a \approx$ 5.8 kJ mol$^{-1}$ in the (N–methyl–1,2–diaminopropane)cadmium(II) tetracyanonickelate(II)/cyclohexane inclusion compound [107]. This value was estimated from temperature dependent $^2$H NMR lineshape studies assuming 12–fold jump motion of the deuterons. On the basis 3–fold jump rotation, Poupko *et al.* [83] determined an activation energy of $E_a \approx$ 10.5kJ mol$^{-1}$ for the cyclohexane molecule in the thiourea/cyclohexane inclusion compound from $^2$H NMR $T_1$ measurements. However, the temperatures for which the measurements were

made (and for which the 3–fold jump rotation was assumed to be applicable) were lower than 130 K and thus lower than the temperature range explored in the IQNS experiments presented above and it is not wholly unexpected to find a higher activation energy at these lower temperatures.

For the thiourea–$d_4$/chlorocyclohexane inclusion compound the same dynamic model was fitted to the experimental data. Here the fits did not yield conclusive evidence of the spatial characteristics of the guest molecular motion. This is probably due to the quality of the data in the experimental $Q$ range, since several spectra are strongly affected either by coherent elastic scattering or inelastic scattering close to the elastic line. The determination of the tilt angle relied on the $Q_{\parallel}$ scattering geometry at 270 K alone, yielding $\zeta = 60.20°$, which is higher than the angle found for thiourea–$d_4$/chlorocyclohexane. This tilt angle is in good agreement with the tilt angle of the chlorocyclohexane molecule determined *via* X–ray powder diffraction in the low temperature phase (see Chapter 4).

The general temperature dependence of the motion appears to be very similar to that of the thiourea–$d_4$/cyclohexane inclusion compound. At the three highest temperatures (T = 270 K, 240 K, and 210 K) the experimental EISF is similar to and consistently lower than the theoretical EISF calculated with a tilt angle of 60.20°. From the linewidths activation parameters were estimated to be $\tau_{0,C_m} = 2.16 \times 10^{-12}$ s and $E_{a,C_m} = 7.20$ kJ mol$^{-1}$ for the 3–fold jump motion about the molecular axis and $\tau_{0,C_t} = 9.11 \times 10^{-13}$ s and $E_{a,C_t} = 10.59$ kJ mol$^{-1}$ for the motion about the tunnel axis. These values must be treated with caution, although the trend of higher activation energies compared to the thiourea–$d_4$/cyclohexane inclusion compound is not unexpected considering the constraints imposed by the thiourea host matrix and the greater size of the chlorocyclohexane molecule.

In view of the poor quality of the data, it is clear that more work is required to understand the dynamic properties of chlorocyclohexane molecules

in their thiourea inclusion compounds. IQNS is an ideal tool for studying this type of problem. Further experiments, at higher resolution and possibly with a different $Q$ range should help to overcome the problems encountered in this study. However, as proposed dynamic models become more complex, so does their mathematical description, which could prove to be a limiting factor in further studies.

# Appendix A

# Scattering Functions and

# Averaging Procedures for

# Incoherent Quasielastic Neutron

# Scattering

## A.1 Averaging Procedures

A wealth of scattering functions for various dynamic models have been reported

in the literature ([44, 108] and references therein). Few dynamic models result

in an inherently isotropic scattering function. For polycrystalline and sem—

ioriented samples it is therefore necessary to average the scattering function

as given in Equation 2.46 over all possible orientations of the position vector

$\underline{r}$ of the hydrogen atom with respect to the scattering vector $\underline{Q}$.

For a polycrystalline sample the averaging is simply achieved by expressing the jump vector in terms of spherical polar coordinates and averaging over the polar and azimuthal angles, respectively. Powder samples are common and most scattering functions found in the literature have been reported as powder averages.

For a semi–oriented sample, it is essential that the vector $\underline{r}$ is expressed in a suitable coordinate system. In the jump models used in Chapter 6 the coordinates were defined as in Reference [109] and are shown in Figure A.1. The molecular frame of reference for cyclohexane is defined by the molecular three–fold axis $\underline{m}$ (coincident with the $\mathbf{Z}$ axis below), $\mathbf{Y}$, the position vector of the hydrogen nucleus in the molecular frame $\underline{r}$, and the angle $\phi$ defining the rotation of $\underline{r}$ with respect to $\mathbf{Y}$. The experimental coordinate system is defined by $\mathbf{x}$, $\mathbf{y}$, and $\mathbf{z}$, where $\mathbf{y}$ coincides with $\mathbf{Y}$, and $\mathbf{z}$ is defined to be coincident with the tunnel axis of the thiourea inclusion compound. The angles $\beta$ and $\alpha$ are the polar and azimuthal angles of $\underline{m}$, respectively, and $\theta$ and $\lambda$ are the polar and azimuthal angles of the scattering vector. $\beta$ defines the tilt of the molecule with respect to the tunnel axis.
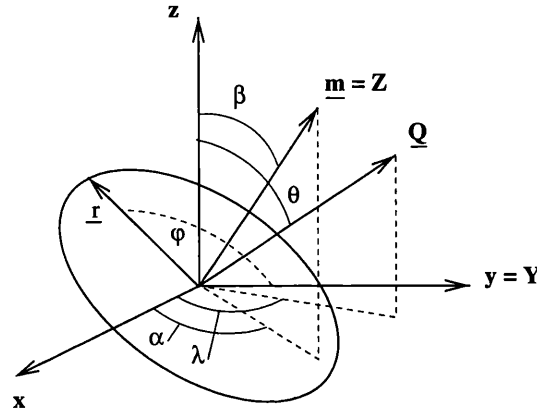
**Figure A.1:** Frame of reference used for the averaging of Q.r with respect to the jump models employed in Chapter 6.

In the molecular frame of reference, defined by the unit vectors $\hat{\underline{X}}$, $\hat{\underline{Y}}$, and $\hat{\underline{Z}}$ the position vector $\underline{r}$ is given by

$$\underline{r} = r\left(-\sin\phi\,\hat{\underline{X}} + \cos\phi\,\hat{\underline{Y}}\right) \tag{A.1}$$

where $\phi$ is the angle between $\underline{r}$ and $\hat{\underline{Y}}$.

The scalar product $\underline{Q}.\underline{r}$ is best expressed in the experimental frame of reference with unit vectors $\hat{\underline{x}}$, $\hat{\underline{y}}$, and $\hat{\underline{z}}$. In the experimental frame of reference the scattering vector is given by

$$\underline{Q} = Q\left(\sin\theta\cos\lambda\,\hat{\underline{X}} + \sin\theta\sin\lambda\,\hat{\underline{Y}} + \cos\theta\,\hat{\underline{Z}}\right) \tag{A.2}$$

The position vector $\underline{r}$ is transformed to the experimental frame of reference using the equation

$$\begin{bmatrix} \hat{\underline{x}} \\ \hat{\underline{y}} \\ \hat{\underline{z}} \end{bmatrix} = \begin{bmatrix} \sin\alpha & -\cos\alpha & 0 \\ \cos\alpha\cos\beta & \sin\alpha\cos\beta & -\sin\beta \\ \cos\alpha\sin\beta & \sin\alpha\sin\beta & \cos\beta \end{bmatrix} \begin{bmatrix} \hat{\underline{X}} \\ \hat{\underline{Y}} \\ \hat{\underline{Z}} \end{bmatrix} \tag{A.3}$$

Applying the transformation yields

$$
\begin{aligned}
\underline{r} = \; & r \left( -\sin \phi \sin \alpha \; + \; \cos \phi \cos \alpha \cos \beta \right) \underline{\hat{x}} \\
& + \; r \left( \sin \phi \cos \alpha \; + \; \cos \phi \sin \alpha \cos \beta \right) \underline{\hat{y}} \\
& - \; r \; \cos \phi \sin \beta \, \underline{\hat{z}}
\end{aligned}
\tag{A.4}
$$

and the scalar product is then

$$
\begin{aligned}
\underline{Q} \cdot \underline{r} = \; & Qr \left( -\sin \theta \cos \lambda \sin \phi \sin \alpha + \; \sin \theta \cos \lambda \cos \phi \cos \alpha \cos \beta \right. \\
& + \; \sin \theta \sin \lambda \sin \phi \cos \alpha \; + \; \sin \theta \sin \lambda \cos \phi \sin \alpha \cos \beta \\
& \left. - \; cos\theta \cos \phi \sin \beta \right)
\end{aligned}
\tag{A.5}
$$

Using standard trigonometric relations, Equation A.5 can be rewritten as

$$
\begin{aligned}
\underline{Q} \cdot \underline{r} = \; & Qr \left[ \sin \theta \left( \cos^2 \frac{\beta}{2} \cos \left( \phi - \lambda + \alpha \right) \right. \right. \\
& \left. \left. - \sin^2 \frac{\beta}{2} \cos \left( \phi + \lambda - \alpha \right) \right) - \cos \theta \sin \beta \cos \phi \right]
\end{aligned}
\tag{A.6}
$$

## A.2 Three–fold Jump Model

Scattering functions for simple jump models are straightforward to derive. Consider a particle jumping between three equivalent sites (see figure A.2). The jumps are assumed to be instantaneous and the particle has a residence time $\tau$ on any given site. The residence time $\tau$ is the inverse of the jump rate $k$. If the particle starts at a site denoted site 1 at time $t = 0$, the self correlation function is given by

$$
G(\underline{r}; \underline{r}_1, t) = p_{11}(t)\delta(\underline{r}) + p_{12}(t)\delta(\underline{r} - \underline{r}_{12}) + p_{13}(t)\delta(\underline{r} - \underline{r}_{13})
\tag{A.7}
$$

where $p_{ij}(t)$ denotes the probability of finding the particle on site $j$ at time $t$ if it started at site $i$ at time $t = 0$. $\underline{r}_{ij}$ denotes the jump vector between sites

$i$ and $j$ and the delta functions ensure that the probabilities exist only if the position vector of the particle is that of the relevant site.
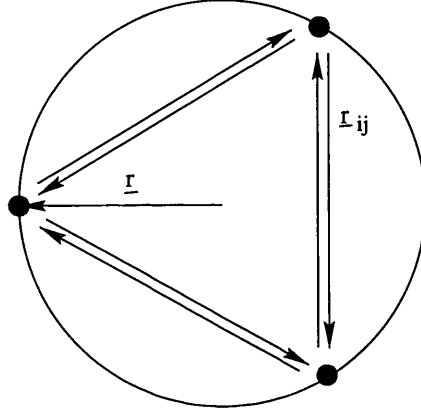


**Figure A.2:** Schematic diagram of the geometry of the three fold jump model. $\underline{r}$ denotes the position vector of the particle and $\underline{r}_{ij}$ denotes the jump vectors.

The initial task is to find expressions for the probabilities $p_{ij}$. With

$$\frac{d}{dt}p_{11} = -2kp_{11} + kp_{12} + kp_{13}$$

$$\frac{d}{dt}p_{12} = kp_{11} - 2kp_{12} + kp_{13} \qquad\qquad (A.8)$$

$$\frac{d}{dt}p_{13} = kp_{11} + kp_{12} - 2kp_{13}$$

the problem becomes that of finding the eigenvalues and eigenfunctions of this set of equations. The eigenvalues are determined *via*

$$\begin{vmatrix} -2k - \lambda & k & k \\ k & -2k - \lambda & k \\ k & k & -2k - \lambda \end{vmatrix} = 0 \qquad\qquad (A.9)$$

and there are three solutions, which are $\lambda_1 = 0$ and $\lambda_2 = \lambda_3 = 3k$. The

eigenfunctions are of the form

$$p_{ij}(t) = A \exp(-\lambda_1 t) + B \exp(-\lambda_2 t) + C \exp(-\lambda_3 t)$$

(A.10)

and the coefficients are determined from the initial conditions

$$p_{11}(t = 0) = 1 \qquad p_{12}(t = 0) = p_{13}(t = 0) = 0$$

and

(A.11)

$$p_{11}(t = \infty) = p_{12}(t = \infty) = p_{13}(t = \infty) = \frac{1}{3}$$

Explicitely, the probability functions are

$$p_{11}(t) = \frac{1}{3} + \frac{2}{3} \exp(-3k\lambda)$$

$$p_{12}(t) = p_{13}(t) = \frac{1}{3} + \frac{1}{3} \exp(-3k\lambda)$$

(A.12)

For a particle starting on site 2 or site 3 the probability functions are identical. The self correlation function is the average over all initial sites and is given by

$$G(\underline{r}, t) = (\frac{1}{3} + \frac{2}{3} \exp(-3kt)) \, \delta(\underline{r})$$

$$+ (\frac{2}{3} - \frac{2}{3} \exp(-3kt)) \, \delta(\underline{r} - \underline{r}_{12})$$

(A.13)

Fourier transforming with respect to $\underline{r}$ and rearranging yields

$$I(\underline{Q}, t) = (\frac{1}{3} + \frac{2}{3} \exp(i\underline{Q} \cdot \underline{r}_{12}))$$

$$+ (\frac{2}{3} - \frac{2}{3} \exp(\underline{Q} \cdot \underline{r}_{12})) \, \exp(-3kt)$$

(A.14)

Fourier transforming with respect to $t$ and taking the real part of the function

(the scattering function is a real function) results in

$$S(\underline{Q},\omega) = (\frac{1}{3} + \frac{2}{3}\exp{(i\underline{Q}.\underline{r}_{12})})$$
$$+ (\frac{2}{3} - \frac{2}{3}\exp{(i\underline{Q}.\underline{r}_{12})}) \frac{1}{\pi} \frac{\tau}{1 + \omega^2\tau^2} \qquad (A.15)$$

For a powder sample, the average over all possible orientations of $\underline{Q}$ with respect to $\underline{r}_{12}$ must be taken. Expressing the scalar product $\underline{Q}.\underline{r}_{12}$ in terms of spherical polar coordinates, this requires averaging over the azimuthal angle $\phi$ and the polar angle $\theta$. The scalar product is

$$\underline{Q}.\underline{r}_{12} = Qr_{12}\sin\theta\cos\phi \qquad (A.16)$$

Inserting Equation A.16 into Equation A.15, the average is

$$\frac{1}{4\pi}\int_0^\pi\int_0^{2\pi} d\theta \, d\phi \, \exp{(iQr_{12}sin\theta\cos\phi)} = j_0(Qr_{12})$$
$$\qquad (A.17)$$

where $j_0$ denotes the spherical Bessel function of zero order.

Finally, the scattering function for a three site jump model averaged for a powder sample is

$$S(\underline{Q},\omega) = (\frac{1}{3} + \frac{2}{3}j_0(Qr_{12})) + (\frac{2}{3} - \frac{2}{3}j_0(Qr_{12})) \frac{1}{\pi} \frac{\tau}{1 + \omega^2\tau^2}$$
$$\qquad (A.18)$$

# A.3   Derivation of the Scattering Function for Model II used in Chapter 6

This model is a simple convolution of two three site jump models.

For each of the two jumps the scalar product $\underline{Q}.\underline{r}$ must be averaged over the appropriate angles. Figure A.1 represents the experimental frame of

reference. The relevant angles over which $\underline{Q}.\underline{r}$ must be averaged are $\phi$ and $\alpha$. The intermediate scattering function can therefore be written as

$$I(\underline{Q},t) = \iiiint_0^{2\pi} d\alpha \, d\alpha_0 \, d\phi \, d\phi_0 \, \exp\left(-\underline{Q}[\underline{r}_0 - \underline{r}_t]\right)$$

$$\times \, P(\alpha,\alpha_0,t) \, P(\alpha_0)P(\phi,\phi_0,t)P(\phi_0) \tag{A.19}$$

where $P(\alpha,\alpha_0,t)$ is the probability function for finding the hydrogen in a position defined by $\alpha$ at time $t$ if it was at an initial position defined by $\alpha_0$ at time $t = 0$. $P(\phi,\phi_0,t)$ has the same meaning, and the functions $P(\alpha_0)$ and $P(\phi_0)$ are the distribution functions for the initial positions.

The distribution functions $P(\alpha_0)$ and $P(\phi_0)$ are given by

$$P(\alpha_0) = P(\phi_0) = \frac{1}{2\pi} \tag{A.20}$$

since all starting positions on the circle X are equally probable.

The distribution functions $P(\alpha,\alpha_0,t)$ and $P(\phi,\phi_0,t)$ are given by [110]:

$$P(\phi,\phi_0,t) = \frac{1}{N} \sum_{n=0}^{N-1} \exp\left(-|t|/\tau_n\right)$$

$$\times \exp\left(in[\phi - \phi_0]\right) \sum_p \delta(\phi - \phi_0 - \frac{2\pi p}{N})$$

$$P(\alpha,\alpha_0,t) = \frac{1}{N'} \sum_{n'=0}^{N'-1} \exp\left(-|t|/\tau_{n'}\right) \tag{A.21}$$

$$\times \exp\left(in'[\phi - \phi_0]\right) \sum_{p'} \delta(\alpha - \alpha_0 - \frac{2\pi p'}{N'})$$

Due to the delta function, the averages over $\phi$ and $\alpha$ yield non–zero terms only

when the conditions

$$\phi \; = \; \phi_0 \; + \; \frac{2\pi p}{N}$$

and                                                            (A.22)

$$\alpha \; = \; \alpha_0 \; + \; \frac{2\pi p'}{N'}$$

are fulfilled.

The scalar product $\underline{Q}.(\underline{r}_0 - \underline{r}_t)$ in Equation A.19 then becomes

$$
\begin{aligned}
\underline{Q}.(\underline{r}_0 - \underline{r}_t) \; = \; Q\,r\,[\sin\theta\,[\cos^2\frac{\beta}{2}(\cos(\phi_0 - \lambda + \alpha_0) \\
- \cos(\phi_0 + \frac{2\pi p}{N} - \lambda + \alpha_0 + \frac{2\pi p'}{N'})) \\
- \sin^2\frac{\beta}{2}(\cos(\phi_0 + \lambda - \alpha_0) \\
- \cos(\phi_0 + \frac{2\pi p}{N} + \lambda - \alpha_0 - \frac{2\pi p'}{N'}))] \\
- \cos\theta\,\sin\beta[\cos\phi_o - \cos(\phi_0 + \frac{2\pi p}{N})]]
\end{aligned}
$$
    (A.23)

In order to separate $\phi_0$ and $\alpha_0$, the scalar product is rewritten using standard trigonometric relations:

$$
\begin{aligned}
\underline{Q}.(\underline{r}_0 - \underline{r}_t) = Q\,r\,[\sin\theta\,[2\sin(\frac{\pi}{N}(p + p'))\cos^2\frac{\beta}{2} \\
- 2\sin(\frac{\pi}{N}(p - p'))\sin^2\frac{\beta}{2}]\cos(\alpha_0 - a)\,\sin\chi_0 \\
+ [2\sin(\frac{\pi}{N}(p + p'))\cos^2\frac{\beta}{2} \\
- 2\sin(\frac{\pi}{N}(p - p'))\sin^2\frac{\beta}{2}]\sin(\alpha_0 - a)\,\cos\chi_0 \\
- 2\sin\frac{\pi p}{N}\,\sin\chi_0\,\cos\theta\,\sin\beta \\
= A(x - y)\cos(\alpha_0 - a) + A'(x + y)\sin(\alpha_0 - a) - C
\end{aligned}
$$
    (A.24)

where the abbreviations

$$A = Q\,r\sin\theta\,\sin\chi_0$$

$$A' = Q\,r\sin\theta\,\cos\chi_0$$

$$C = 2\sin\frac{\pi p}{N}\,\sin\chi_0\,\cos\theta\,\sin\beta$$

$$x = 2\sin\left(\frac{\pi}{N}(p+p')\right)\cos^2\frac{\beta}{2}$$

$$\text{(A.25)}$$

and

$$y = 2\sin\left(\frac{\pi}{N}(p-p')\right)\sin^2\frac{\beta}{2}$$

are introduced to simplify the notation.

The intermediate scattering function can now be written as

$$I(\underline{Q},t) = \frac{1}{4\pi}\iint_0^{2\pi} d\alpha_0\,d\phi_0\sum_{p=1}^{3}$$

$$\times \sum_{p'=1}^{3}\exp\left(-i[A(x-y)\cos(\alpha_0-a) + A'(x+y)\cos(\alpha_0-a) - C]\right)$$

$$\times \frac{1}{N}\sum_{n=0}^{N-1}\exp\left(-|t|/\tau_n\right)\frac{1}{N'}\sum_{n'=0}^{N'-1}\exp\left(-|t|/\tau_{n'}\right)$$

$$\text{(A.26)}$$

and integrating over $\alpha_0$ yields

$$I(\underline{Q},t) = \frac{1}{2\pi}\int_0^{2\pi} d\phi_0\sum_{p=1}^{3}\sum_{p'=1}^{3}\exp\left(iC\right)J_0\left(\sqrt{(A(x-y))^2 + (A'(x+y))^2}\right)$$

$$\times \frac{1}{N}\sum_{n=0}^{N-1}\exp\left(-|t|/\tau_n\right)\frac{1}{N'}\sum_{n'=0}^{N'-1}\exp -\left(|t|/\tau_{n'}\right)$$

$$= \frac{1}{2\pi}\int_0^{2\pi} d\phi_0\sum_{p=1}^{3}\sum_{p'=1}^{3}\cos\left(2sin\frac{\pi p}{N}\,\sin\chi_0\,\cos\theta\,\sin\beta\right)$$

$$\text{(A.27)}$$

$$\times\,J_0(2Qr\,\sin\theta\,\sqrt{x^2+y^2+2xy\cos2\chi_0})$$

$$\frac{1}{N}\frac{1}{N'}\sum_{n=0}^{N-1}\sum_{n'=0}^{N'-1}\exp -\left(|t|/[\tau_n+\tau_{n'}]\right)$$

Equation A.27 cannot be integrated analytically and must be integrated numerically in the fits described in Chapter 6, in addition to applying a Fourier transformation in order to obtain $S(\underline{Q}, \omega)$.

# References

[1] Parsonage, N. G. and Stavely, L. A. K. *Disorder in Crystals*. Clarendon Press, Oxford, (1978).

[2] Timmermans, J. *Journal Physique Chemie* **35**, 25 (1938).

[3] Sherwood, J. N. *The Plastically Crystalline State*. John Wiley & Sons, Chichester, (1979).

[4] Davy, H. *Philosophical Transactions of the Royal Society* **101**, 155 (1811).

[5] Atwood, J. C., Davies, J. E. D., and MacNicol, D. D., editors. *Inclusion Compounds*, volume 1. Academic Press, London, (1984).

[6] Atwood, J. C., Davies, J. E. D., and MacNicol, D. D., editors. *Inclusion Compounds*, volume 2. Academic Press, London, (1984).

[7] Lehn, J. M., Atwood, J. L., Davies, J. E. D., MacNicol, D. D., and Vögtle, F., editors. *Comprehensive Supramolecular Chemistry*, volume 6, 7. Pergamon Press, Oxford, (1996).

[8] Atwood, J. C., Davies, J. E. D., and MacNicol, D. D., editors. *Inclusion Compounds*, volume 3. Academic Press, London, (1984).

[9] Oterospinar, F. J., Anguianoigea, S., Garciagonzalez, N., and Vilajato, J. L. *International Journal of Pharmaceutics* **75**, 37 (1991).

[10] Sanghavi, N. M., Choudhari, K. B., Matharu, R. S., and Vishanathan, L. *Drug Development and Industrial Pharmacy* **19**, 701 (1993).

[11] Tam, W., Eaton, D. F., Calabrese, J. C., Williams, I. D., Wang, Y., and Anderson, A. G. *Chemistry of Materials* **1**, 128 (1989).

[12] Anderson, A. G., Calabrese, J. C., Tam, W., and Williams, I. D. *Chemical Physics Letters* **134**, 392 (1987).

[13] Heald, S. M. and Tranquada, J. M. *Physical Methods of Chemistry, Determination of Structural Features of Crystalline and Amorphous Solids*, volume 5, chapter 3, 189. Wiley, New York (1986).

[14] Fricke, H. *Physical Review* **16**, 202 (1920).

[15] Hertz, G. *Zeitschrift für Physik* **3**, 19 (1920).

[16] Stern, E. A. *Physical Review B* **10**, 3027 (1974).

[17] Lee, P. A. and Pendry, J. B. *Physical Review B* **11**, 2795 (1975).

[18] Teo, B. K. and Joy, D. C., editors. *EXAFS Spectroscopy, Techniques and Application*, chapter 3, 13. Plenum Press, New York (1981).

[19] Stern, E. A., Sayers, D. E., and Lytle, F. W. *Physical Review B* **11**, 4836 (1975).

[20] Programs SPLINE and XFIT by P. J. Ellis, Department of Chemistry, University of Sydney, Australia, 1993.

[21] Ellis, P. J. and Freeman, H. C. *Journal of Synchrotron Radiation* **2**, 190 (1995).

[22] Rehr, J. J., Mustre de Leon, J., Zabinsky, S. I., and Albers, R. C. *Journal of the American Chemical Society* **113**, 5135 (1991).

[23] Joyner, R. W., Martin, K. J., and Meehan, P. *Journal of Physics C: Solid State Physics* **20**, 4005 (1987).

[24] Woolfson, M. M. *X–Ray Crystallography*. Cambridge University Press, Cambridge, (1970).

[25] Rietveld, H. M. *Acta Crystallographica* **22**, 151 (1967).

[26] March, A. *Zeitschrift für Kristallographie* **81**, 285 (1932).

[27] Dollase, W. A. *Journal of Applied Crystallography* **19**, 267 (1986).

[28] Young, R. A. and Wiles, D. B. *Journal of Applied Crystallography* **15**, 430 (1982).

[29] Young, R. A., editor. *The Rietveld Method.* Oxford Science Publications, Oxford, (1993).

[30] Larson, A. C. and Von Dreele, R. B. *GSAS Training and Technical Manual.* Los Alamos National Laboratory, Los Alamos, New Mexico, (1994).

[31] Louër, D. and Vargas, R. *Journal of Applied Crystallography* **15**, 542 (1982).

[32] Werner, P. E., Erikson, L., and Westdahl, M. J. *Journal of Applied Crystallography* **18**, 367 (1985).

[33] Visser, J. W. *Journal of Applied Crystallography* **2**, 89 (1969).

[34] Harris, K. D. M., Gameson, I., and Thomas, J. M. *Journal of the Chemical Society, Faraday Transactions* **86**, 3135 (1990).

[35] Larson, A. C. and Von Dreele, R. B. Technical Report LA–UR–86–748, Los Alamos National Laboratory, (1987).

[36] Le Bail, A., Duroy, H., and Fourquet, J. L. *Materials Research Bulletin* **23**, 447 (1988).

[37] Thompson, P., Cox, D. E., and Hastings, J. B. *Journal of Applied Crystallography* **20**, 79 (1987).

[38] Rietveld, H. M. *Journal of Applied Crystallography* **2**, 65 (1969).

[39] Squires, G. L. *Thermal Neutron Scattering*. Cambridge University Press, Cambridge, (1978).

[40] Lovesey, S. W. *Theory of Neutron Scattering from Condensed Matter*, volume 1. Oxford University Press, Oxford, (1984).

[41] Sears, V. F. *Neutron News* **3**, 26 (1992).

[42] Van Hove, L. *Physical Review* **95**, 249 (1954).

[43] Sears, V. F. *Advances in Physics* **24**, 1 (1975).

[44] Bée, M. *Quasielastic Neutron Scattering*. A. Hilger, Bristol (1988).

[45] Park, K.-M., Hashimoto, M., Kitazawa, T., and Iwamoto, T. *Chemistry Letters*, 1701 (1990).

[46] Nishikiori, S., Iwamoto, T., and Yoshino, Y. *Bulletin of the Chemical Society of Japan* **53**, 2236 (1980).

[47] Iwamoto, T. *The Hofmann-Type And Related Inclusion Compounds*, chapter 2. Volume 1 of Atwood et al. [5] (1984).

[48] Schlenk, Jr., W. *Justus Liebigs Annalen der Chemie* **572**, 142 (1951).

[49] Lenné, H.-U. *Acta Crystallographica* **7**, 1 (1954).

[50] Park, K.-M. and Iwamoto, T. *Jounal of the Chemical Society, Chemical Communications*, 72 (1992).

[51] Park, K.-M. and Iwamoto, T. *Journal of the Chemical Society, Dalton Transactions*, 1875 (1993).

[52] Harris, K. D. M. and Thomas, J. M. *Journal of the Chemical Society, Faraday Transactions* **86**, 1095 (1990).

[53] Shannon, I. J., Harris, K. D. M., Mahdyarfar, A., Johnston, P., and Joyner, R. W. *Journal of the Chemical Society, Faraday Transactions* **89**, 3099 (1993).

[54] Shannon, I. J., Jones, M. J., Harris, K. D. M., Siddiqui, M. R. H., and Joyner, R. W. *Journal of the Chemical Society, Faraday Transactions* **91**, 1497 (1995).

[55] Chernov, V. A., Nikitenko, S. G., and Danilenko, A. M. *Nuclear Instruments and Methods in Physics Research A* **359**, 248 (1995).

[56] Lund, A., Nicholson, D. G., Lamble, G., and Beagley, B. *Journal of Materials Chemistry* **4**, 1723 (1994).

[57] Cassagneau, T., Hix, G. B., Jones, D. J., Maireless-Torres, P., and Rhomari, M. *Journal of Materials Chemistry* **4**, 189 (1994).

[58] Sankar, G., Wright, P. A., Natarajan, S., Thomas, J. M., Greaves, G. N., Dent, A. J., Dobson, B. R., Ramsdale, C. A., and Jones, R. H. *Journal of Physical Chemistry* **97**, 9550 (1993).

[59] Pandya, K. I., Heald, S. M., Hriljac, J. A., Petrakis, L., and Fraissard, J. *Journal of Physical Chemistry* **100**, 5070 (1996).

[60] Barrett, P. A., Sankar, G., Catlow, C. R. A., and Thomas, J. M. *Journal of Physical Chemistry* **100**, 8977 (1996).

[61] Thomas, J. M. and Greaves, G. N. *Catalysis Letters* **20**, 337 (1993).

[62] Angla, B. *Comptes Rendus* **224**, 402 (1947).

[63] Angla, B. *Comptes Rendus* **224**, 1166 (1947).

[64] Takemoto, K. and Sonoda, N. *Inclusion Compounds of Urea, Thiourea and Selenourea*, chapter 2. Volume 2 of Atwood et al. [6] (1984).

[65] Harris, K. D. M. and Hollingsworth, M. D. *Urea, Thiourea and Selenourea Inclusion Compounds.* Volume 6 of Lehn et al. [7] (1996).

[66] Shindo, T., Shindo, M., Ohnuma, H., and Kabuto, C. *Bulletin of the Chemical Society of Japan* **66**, 1941 (1993).

[67] Truter, M. R. *Acta Crystallographica* **22**, 556 (1967).

[68] Gopal, R., Robertson, B. E., and Robertson, J. S. *Acta Crystallographica* **C45**, 257 (1989).

[69] Clément, R., Claude, R., and Mazières, C. *Journal of the Chemical Society, Chemical Communications*, 654 (1974).

[70] Lanaurdie, M. *Comptes Rendus* **235**, 154 (1952).

[71] Klæboe, P., Lothe, J. J., and Lunde, K. *Acta Chemica Scandinavica* **10**, 1465 (1956).

[72] Kozima, K. and Sakashita, K. *Bulletin of the Chemical Society of Japan* **31**, 796 (1958).

[73] Klæboe, P. *Acta Chemica Scandinavica* **23**, 2641 (1969).

[74] Aliev, A. E. and Harris, K. D. M. *Journal of the Americal Chemical Society* **115**, 6369 (1993).

[75] Gustavsen, J. E., Klæboe, P., and Kvila, H. *Acta Chemica Scandinavica* *A* **32**, 25 (1978).

[76] George, A. R. and Harris, K. D. M. *Journal of Molecular Graphics* **13**, 138 (1995).

[77] Clément, R., Mazières, C., Gourdji, M., and Guibé, L. *Journal of Chemical Physics* **67**, 5381 (1977).

[78] Lowery, M. D., Wittebort, R. J., Sorai, M., and Hendrickson, D. N. *Journal of the American Chemical Society* **112**, 4214 (1990).

[79] Nakai, T., Terao, T., Imashiro, F., and Saika, A. *Chemical Physics Letters* **132**, 554 (1986).

[80] Heyes, S. J., Clayden, N. J., and Dobson, C. M. *Journal of Physical Chemistry* **95**, 1547 (1991).

[81] Clément, R., Gourdji, M., and Guibé, L. *Journal of Magnetic Resonance* **20**, 345 (1975).

[82] Müller, K. *Journal of Physical Chemistry* **96**, 5733 (1992).

[83] Poupko, R., Fourman, E., Müller, K., and Luz, Z. *Journal of Physical Chemistry* **95**, 407 (1991).

[84] Gibb, T. C. *Journal of Physics C, Solid State Physics* **9**, 2627 (1976).

[85] Clément, R., Gourdji, M., and Guibé, L. *Molecular Physics* **21**, 247 (1971).

[86] Hough, E. and Nicolson, D. G. *Journal of the Chemical Society, Dalton Transactions*, 15 (1978).

[87] Hahn, T., editor. *International Tables For Crystallography*, volume A: Space Group Symmetry. International Union of Crystallography, D. Reidel Publishing Company, Dordrecht, (1987).

[88] Harris, K. D. M. *Journal of Solid State Chemistry* **84**, 280 (1990).

[89] Müller, K. *Magnetic Resonance in Chemistry* **30**, 228 (1992).

[90] McKinnon, M. S. and Wasylishen, R. E. *Chemical Physics Letters* **130**, 565 (1986).

[91] Garneau, I., Raymond, S., and Brisse, F. *Acta Crystallographica* **C51**, 538 (1995).

[92] Breed, L. W. and Murril, E. *Inorganic Chemistry* **10**, 641 (1971).

[93] Aliev, A. E. and Harris, K. D. M. *Mendeleev Communications*, 153 (1993).

[94] Aliev, A. E., Harris, K. D. M., and Apperley, D. C. *Chemical Physics Letters* **226**, 193 (1994).

[95] Bée, M. Technical Report 84BE05T, Institut Laue Langevin, (1984).

[96] Bée, M. PhD thesis, University of Lille, (1980).

[97] Sears, V. F. *Canadian Journal of Physics* **44**, 1999 (1966).

[98] Bée, M., Jobic, H., and Sourisseau, C. *Journal of Physics C* **18**, 5771 (1985).

[99] Bée, M. and Amoureux, J. P. *Molecular Physics* **48**, 63 (1983).

[100] Allen, F. H., Kennard, O., Watson, D. G., Brammer, L., Orpen, A. G., and Taylor, R. *Journal of the Chemical Society, Perkin Transactions* **2**, S1 (1987).

[101] Aliev, A. E., Harris, K. D. M., Apperley, D. C., and Harris, R. K. *Journal of Solid State Chemistry* **110**, 314 (1994).

[102] Meirovitch, E., Krant, T., and Vega, S. *Journal of Physical Chemistry* **87**, 1390 (1983).

[103] McKinnon, M. S. and Wasylishen, R. E. *Chemical Physics Letters* **130**, 565 (1986).

[104] Rieutord, F. Technical Report 90RI17T, Institut Laue Langevin, (1990).

[105] Volino, F. and Dianoux, J. A. *Molecular Physics* **41**, 271 (1980).

[106] Hall, P. L. and Ross, D. K. *Molecular Physics* **42**, 673 (1981).

[107] Nishikiori, S., Ratcliffe, C. I., and Ripmeester, J. A. *Journal of Physical Chemistry* **94**, 8098 (1990).

[108] Brot, C. and Lassier-Govers, B. *Berichte der Bunsen Gesellschaft* **80**, 31 (1976).

[109] Dianoux, A. J., Volino, F., and Hervet, H. *Molecular Physics* **30**, 1181 (1975).

[110] Rigny, P. *Physica* **59**, 707 (1972).